# Lawrence Berkeley National Laboratory

## Recent Work

### Title


The Development of Potassium Tantalate Niobate Thin Films for Satellite-based Pyroelectric Detectors


### Permalink

https://escholarship.org/uc/item/3332n00c



### Author

Cherry, Hilary Beatrix Baumann



### Publication Date

1997-05-22



eScholarship.org Powered by the California Digital Library University of California

LBNL-40412
UC-000

# ERNEST ORLANDO LAWRENCE BERKELEY NATIONAL LABORATORY

# The Development of Potassium Tantalate Niobate Thin Films for Satellite-based Pyroelectric Detectors

Hilary B.B. Cherry
**Engineering Division**

May 1997
Ph.D. Thesis

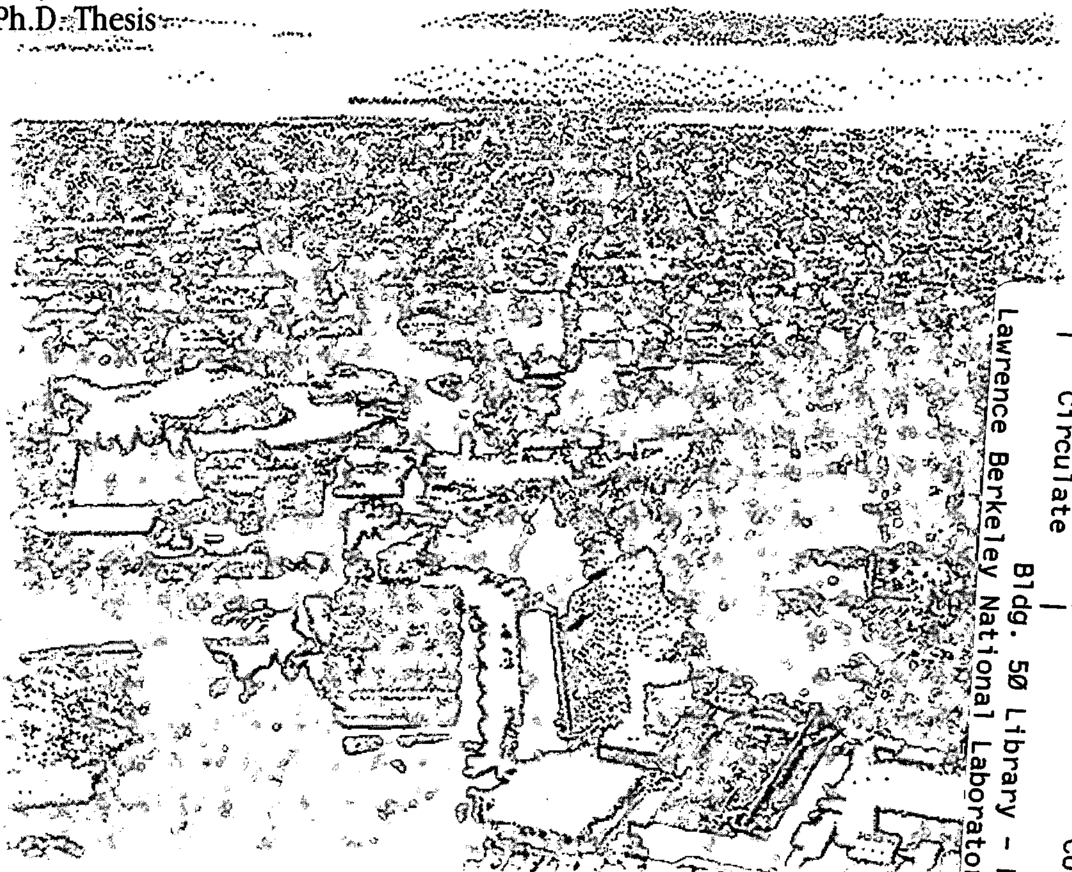

REFERENCE COPY
Does Not
Circulate
Bldg. 50 Library - Ref.
Lawrence Berkeley National Laboratory
LBNL-40412
Copy 1

## DISCLAIMER

This document was prepared as an account of work sponsored by the United States Government. While this document is believed to contain correct information, neither the United States Government nor any agency thereof, nor the Regents of the University of California, nor any of their employees, makes any warranty, express or implied, or assumes any legal responsibility for the accuracy, completeness, or usefulness of any information, apparatus, product, or process disclosed, or represents that its use would not infringe privately owned rights. Reference herein to any specific commercial product, process, or service by its trade name, trademark, manufacturer, or otherwise, does not necessarily constitute or imply its endorsement, recommendation, or favoring by the United States Government or any agency thereof, or the Regents of the University of California. The views and opinions of authors expressed herein do not necessarily state or reflect those of the United States Government or any agency thereof or the Regents of the University of California.

LBNL-40412
UC-000

# The Development of Potassium Tantalate Niobate Thin Films for Satellite-based Pyroelectric Detectors

Hilary Beatrix Baumann Cherry

Materials Science and Mineral Engineering
University of California, Berkeley

and

Engineering Division
Ernest Orlando Lawrence Berkeley National Laboratory
University of California
Berkeley, California 94720

Ph.D. Thesis

May 1997

This work was supported by NASA Grant No. A14221D (SLS) under Interagency Agreement with the Director, Office of Energy Research, Office of Health and Environmental Research, U.S. Department of Energy under Contract No. DE-AC03-76SF00098.

# The Development of Potassium Tantalate Niobate Thin Films for Satellite-based Pyroelectric Detectors

by

Hilary Beatrix Baumann Cherry

B.S. (University of California) 1989
M.S. (University of California) 1993

A dissertation submitted in partial satisfaction of the

requirements for the degree of

Doctor of Philosophy

in

Engineering-Materials Science and Mineral Engineering

in the

GRADUATE DIVISION

of the

UNIVERSITY OF CALIFORNIA at BERKELEY

Committee in charge:

Professor Eugene E. Haller, Chair
Professor Timothy Sands
Professor Richard M. White

1997

# The Development of Potassium Tantalate Niobate Thin Films for Satellite-based Pyroelectric Detectors

Copyright © 1997

by

Hilary Beatrix Baumann Cherry

The U.S. Department of Energy has the right to use this document
for any purpose whatsoever including the right to reproduce
all or any part thereof

Abstract

The Development of Potassium Tantalate Niobate Thin Films for Space-based Pyroelectric Detectors

by

Hilary Beatrix Baumann Cherry

Doctor of Philosophy in Engineering

University of California, Berkeley

Professor Eugene E. Haller, Chair

Potassium tantalate niobate (KTN) pyroelectric detectors are expected to provide detectivities of 3.7 x $10^{11}$ cmHz$^{1/2}$W$^{-1}$ for satellite-based infrared detection at 90 K. The background limited detectivity for a room-temperature thermal detector is 1.8 x $10^{10}$ cmHz$^{1/2}$W$^{-1}$. KTN is a unique ferroelectric for this application because of the ability to tailor the temperature of its pyroelectric response by adjusting its ratio of tantalum to niobium. The ability to fabricate high quality KTN thin films on Si-based substrates is crucial to the development of KTN pyroelectric detectors. $Si_xN_y$ membranes created on the Si substrate will provide the weak thermal link necessary to reach background limited detectivities. The device dimensions obtainable by thin film processing are expected to increase the ferroelectric response by 20 times over bulk fabricated KTN detectors. In addition, microfabrication techniques allow for easier array development.

This is the first reported attempt at growth of KTN films on Si-based substrates. Pure phase perovskite films were grown by pulsed laser deposition on $SrRuO_3$/Pt/Ti/$Si_xN_y$/Si and $SrRuO_3$/$Si_xN_y$/Si structures; room temperature dielectric permittivities for the KTN films were 290 and 2.5, respectively. The dielectric permittivity for bulk grown, single crystal KTN is ~ 380. In addition to depressed dielectric

permittivities, no ferroelectric hysteresis was found between 80 and 300 K for either structure. RBS, AES, TEM and multi-frequency dielectric measurements were used to investigate the origin of this apparent lack of ferroelectricity. The most likely explanation is the presence of point defects. Other issues addressed by this dissertation include: the role of oxygen and target density during pulsed laser deposition of KTN thin films; the use of YBCO, LSC and Pt as direct contact bottom electrodes to the KTN films, the adhesion of the bottom electrode layers to $Si_xN_y$/Si and the top electrode adhesion.

# Acknowledgements

I thank my advisor Professor Eugene E. Haller for his guidance and support during my graduate career. The staff and graduate students within our research group also contributed a great deal to my development as a scientist and engineer. I would like to single out Jeff Beeman for his advice and technical support on many issues, Annabel Nickles for the many discussions on ferroelectrics, and Kristin Duxstad and Kin Man Yu for performing and analyzing my RBS measurements. In addition, I thank Frances Ross, formerly of NCEM, who produced all the TEM micrographs presented in this dissertation and worked with me in their analyses; Ron Reade who introduced me to the pulsed laser deposition technique and grew my first set of samples, Professor Timothy Sands for his advice and valuable discussions on many aspects of my research and my husband Will Cherry, J.D., C.P.A.

I was fortunate to receive a Graduate Opportunity Fellowship offered through the University and a three year NASA Earth System Science Fellowship. In addition, this research was a part of a collaboration with NASA Ames and I thank G. Scott Hubbard and Robert E. McMurray, Jr. for their support of this project.

This work was supported by NASA Grant No. A14221D (SLS) under Interagency Agreement with the Director, Office of Energy Research, Office of Health and Environmental Research, U.S. Department of Energy under Contract No. DE-AC03-76SF00098.

TABLE OF CONTENTS

1. Introduction . . . . . . . . . . 1

1.1. Pyroelectric Detector Development . . . . . . . . . . 1

1.2. Ferroelectric Thin Films . . . . . . . . . . 5

2. Ferroelectric Materials . . . . . . . . . . 7

2.1. Dielectric Properties . . . . . . . . . . 7

2.2. Ferroelectricity . . . . . . . . . . 13

2.3. Structure . . . . . . . . . . 22

2.4. Electromechanical Behavior . . . . . . . . . . 26

3. Pyroelectric Detectors . . . . . . . . . . 29

3.1. Signal Formation . . . . . . . . . . 29

3.2. Noise . . . . . . . . . . 35

3.3. Materials Selection . . . . . . . . . . 38

3.4. Thin Film Approach . . . . . . . . . . 40

4. Review of Thin Film Growth . . . . . . . . . . 46

4.1. Pulsed Laser Deposition . . . . . . . . . . 46

4.2. Silicon Integration . . . . . . . . . . 49

4.3. Potassium Tantalate Niobate . . . . . . . . . . 50

5. Experiments and Results ........ 55

5.1 Target Fabrication ........ 55

5.2 Thin Film Growth ........ 60

5.2.1 Overview ........ 60

5.2.2 Study of Potassium Tantalate Niobate Growth on Platinum ........ 62

5.2.3 KTN Growth on Lanthanum Aluminate Substrates ........ 66

5.2.4 KTN Growth on Conducting Oxides ........ 76

5.2.4.1 Lanthanum Strontium Cobalt Oxide ........ 76

5.2.4.2 Yttrium Barium Copper Oxide ........ 91

5.2.4.3 Strontium Ruthenium Oxide ........ 97

5.3 Integration ........ 100

5.4 Discussion ........ 101

6. Conclusions ........ 106

7. Appendices ........ 109

A. Crystallographic Point Groups ........ 109

B. Thin Film Deposition Techniques ........ 110

C. Characterization Techniques ........ 111

D. Photolithography Steps ........ 116

8. References ........ 117

# 1. Introduction

## 1.1. Pyroelectric Detector Development

Outside the visible spectrum, at its red end, exists the infrared region with wavelengths longer than those of visible light. The infrared region of electromagnetic radiation spans photon wavelengths from 0.7 to 1000 μm. The origin of infrared photons are the gases, liquids and solids that make up our universe. These infrared sources can both absorb and emit infrared radiation. The dependence of radiation absorption and emission spectra on wavelength identifies and provides detailed information about the materials in our universe. Infrared detectors bring this valuable information within the purview of human observation through their use in a wide variety of optical characterization instruments, planetary exploration, space - and astrophysics, atmospheric radiation measurement and numerous commercial applications.

Currently, there is a need for high sensitivity broadband infrared detectors for satellite-based systems aimed at studying Earth and its atmosphere. Hydrological, biogeochemical, geophysical, climatological, ecological and solar fluence data can be gathered by infrared detectors and used by scientists around the world to develop a global model for the interactions between different physical climate systems and the human impact upon them. The primary hydrologic processes of interest are the interaction of land and ocean surfaces with the atmosphere through the transport of heat, mass and momentum. Scientists are also interested in exploring biogeochemical processes such as the formation, dissipation, transportation and distribution of trace gases and aerosols. Geophysical processes are of interest because they shape and modify the Earth's surface through plate tectonics, volcanism, and the melting of glaciers and sea ice. A better understanding of climatological processes, such as the formation and dissipation of clouds and their interactions with solar radiation, could lead to more accurate predictions of global weather patterns. There is also interest in

studying the interactions between global change and ecological processes and the response to such changes through adaptation.[1] The absorption spectra of molecules comprising atmospheric targets such as the ozone layer and clouds are viewed using the sun as an infrared radiation source. Targets on the Earth's surface are observed by measuring the characteristic radiation emission spectra of different vegetation and soils, for example. These absorption and emission measurements are quite complex and require sensitive detectors that can measure over a broad wavelength range.

Detectors for these applications must meet the low mass and power constraints of satellites, have long-term stability (5 - 10 years), extended spectral range (3 - 50 μm), flat wavelength response, and capability of integration into imaging arrays.[2] There are many different types of detectors operating in the infrared; they can be separated into two groups: thermal detectors and photon detectors. Thermal detectors, a class which includes bolometers and pyroelectric detectors, operate by monitoring a temperature sensitive material property which is altered by heat from absorbed radiation. Photon detectors measure the change in the number or mobility of free charge carriers brought about by changes in the flux of incident photons.[3] Thermal detectors are desired for this mission because they have no limitation in the wavelength of the photons they can detect leading to an extended spectral range and a flat wavelength response. In contrast, photon detectors have a cut-off wavelength, due to the bandgap of the material, above which they can no longer detect incoming radiation. In addition, the duration of these missions requires that the detectors operate at temperatures where passive cooling is possible. With passive cooling, temperatures as low as 85 K can be reached; however temperatures between 90 and 100 K are more easily obtained leading to ≥ 90 K operating temperatures. Sensitive photon detectors require cooling below this limit using liquid helium refrigerators or self-maintained mechanical cryopumps. The short operating life of liquid helium refrigerators (2 years) and self-maintained mechanical cryopumps (3-5 years) prohibits their use in long-term missions.

Currently, detectors such as $Hg_{1-x}Cd_xTe$ photodiodes and semiconductor bolometers are used for these satellite-based applications. $Hg_{1-x}Cd_xTe$ infrared detectors are fairly sensitive at temperatures between 77 and 100 K, exhibiting specific detectivities (D*) of 1 - 2 x $10^{11}$ cm $Hz^{1/2}$ $W^{-1}$ but only for a narrow spectral band between 6 and 13 µm. The spectral response above 14 µm decreases rapidly and is already < $10^9$ cm $Hz^{1/2}$ $W^{-1}$ at 15 µm.[4] Unlike the $Hg_{1-x}Cd_xTe$ photodiodes semiconductor bolometers are thermal detectors and therefore have an inherent extended spectral range and flat wavelength response. Unfortunately, they must be operated at very low temperatures, ~ 2 - 4 K, to obtain the same sensitivity as $Hg_{1-x}Cd_xTe$ photodiodes severely limiting there use in satellite-based applications. Another competing technology comes from high temperature superconducting bolometers, in particular YBCO ($T_c$ = 90 K), where large changes in resistance occur at the transition between the superconducting and normal states. YBCO is currently under investigation by other researchers; the best sensitivity reported to date for detectors operating ≥ 90 K is D* = 6 x $10^9$ cm $Hz^{1/2}$ $W^{-1}$ (4 Hz and 90 - 91 K).[5] This is almost two orders of magnitude less than the theoretical limit for a thermal detector.

Pyroelectric detectors are thermal detectors that are expected to meet the needs of satellite-based infrared detectors. Room-temperature pyroelectric detectors are currently limited by their thermal or Johnson noise. By decreasing the operating temperature of thermal detectors one can increase the performance of the detectors as measured by their specific detectivity, D*. Theoretical calculations show that in the thermal noise limited case decreasing the temperature to 90 K increases the D* to 3.7 x $10^{11}$ cm $Hz^{1/2}$ $W^{-1}$ from 1.8 x $10^{10}$ cm $Hz^{1/2}$ $W^{-1}$ at 300 K.[6] In the Johnson noise limited case increases in D* will also occur but to a lesser extent. To maximize the sensitivity of pyroelectric detectors it is desirable to operate them near the peak in their pyroelectric coefficient, which can occur anywhere between 30 K and 1000 K depending on the material selected.[7] The pyroelectric coefficient is the temperature

sensitive property of the material used to monitor radiation absorbed by the pyroelectric detector. This dissertation describes the development of potassium tantalate niobate (KTN) thin films for pyroelectric detector arrays operating at ~ 90 K. Section 1.2 describes the current status of growing ferroelectric materials integrated with silicon substrates. Chapter 2 provides a review of ferroelectric materials including their structure, properties and theory. Section 2.1 reviews basic dielectric properties, and Section 2.2 focuses on a description of ferroelectricity. The structure and basic types of ferroelectric materials are reviewed in Section 2.3. Section 2.4 reviews the electromechanical interactions of ferroelectric materials as derived from a phenomenological theory. In Chapter 3 a general discussion of pyroelectric detector operation is given in Section 3.1. Section 3.2 reviews the performance of pyroelectric detectors in terms of their noise. The selection of ferroelectric materials for infrared radiation measurement at 90 K is the topic of Section 3.3. The choice to fabricate thin-film pyroelectric detectors is discussed in Section 3.4.

Chapter 4 describes the approach taken to develop thin-film ferroelectrics. Section 4.1 reviews the pulsed laser deposition thin film technique. Progress in the growth of ferroelectric materials integrated with Si substrates is reviewed in Section 4.2. A review of the growth of potassium tantalate niobate thin films is given in Section 4.3. Chapter 5 details the experimental results. Section 5.1 describes the experimental procedure for fabricating potassium tantalate niobate targets and results. Section 5.2 lays out the growth parameters of KTN thin films deposited by pulsed laser deposition on various substrates. Experiments performed with respect to the integration of KTN with Si substrates are the topic of Section 5.3. Section 5.4 discusses the results, Chapter 6 concludes and provides a direction for future work.

## 1.2. Ferroelectric Thin Films

Ferroelectric materials are a subclass of pyroelectric materials, which are a subclass of piezoelectric materials, which in turn are a subclass of dielectric materials, see Figure 1. Ferroelectric materials are valued for their substantial dielectric, ferroelectric, piezoelectric, pyroelectric, and electro-optic properties. Early investigations of ferroelectric materials for electronic devices utilizing these unique properties were severely limited by the lack of a viable thin-film technology. Advances in thin film processing cultivated by silicon-based research and development have lead to renewed interest in ferroelectric materials for device applications. Current technology combined with the need for improved dielectric materials has fueled tremendous growth in thin-film ferroelectric processing over the past seven years.[8] Currently, ferroelectric thin films are being actively developed for integration into DRAMs (dynamic random-access memories), NVRAMs (nonvolatile ferroelectric random-access memories), MEMS (microelectromechanical systems), room-temperature infrared detector arrays, and image-storage systems.[9]

Although considerable progress has been achieved in the processing of ferroelectric thin films there are still many critical issues outstanding. One aspect common to many of the applications is the integration of ferroelectric thin films with silicon substrate and device technology. Ferroelectric thin film research aimed at integration is focusing on developing appropriate electrode technologies, discovering and producing suitable ferroelectric materials, developing scalable deposition processes† with good conformal coverage of nonplanar surfaces, and optimizing lithography and reactive ion etching processes.[10] Most of these are issues for materials development of KTN thin films for pyroelectric detector arrays. The development of KTN thin film materials has progressed over several stages. Initially the growth of KTN thin films on closely lattice-matched and chemically similar materials was

† Many Si crystal growers are now producing 8" and 12" diameter single crystals.

achieved. The progression of this dissertation focuses on the choice of electrode material and growth of KTN ferroelectric capacitors with desirable electrical properties on them.

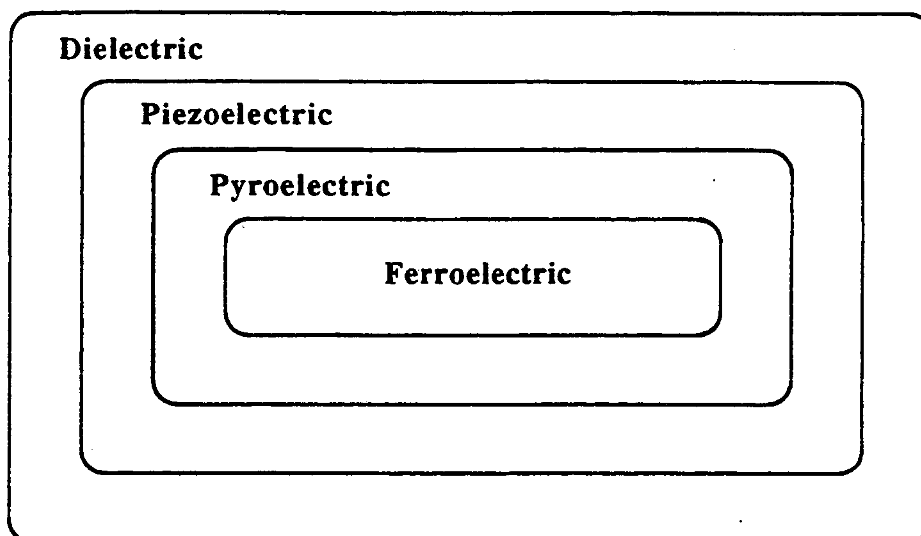


Figure 1. Dielectric materials and sub-classes.

## 2. Ferroelectric Materials

### 2.1. Dielectric Properties

Ferroelectric materials are a sub-class of pyroelectric materials which fall under the general class of dielectric materials. Dielectric materials are polarizable by the application of an electric field, E. Polarization is defined as the sum of electric dipole moments arising from the separation of ionic and electronic charge. The polarization of the crystal can be expressed in terms of the polarization charge, Q', produced at the electrodes divided by the electrode area (A),

$$P = \frac{Q'}{A}. \qquad [1]$$

The dielectric constant, $\varepsilon$, is a measure of this polarization, P, as a function of an applied electric field;

$$\mathbf{P} = (\varepsilon-1)\varepsilon_o\mathbf{E} \ , \qquad [2]$$

where $\varepsilon_o$ is the absolute permittivity of a vacuum. A material with non-linear polarization vs. electric field behavior has a variable dielectric constant or relative dielectric permittivity. Values of relative dielectric permittivity range from $1 - 10^5$, but values for most insulating materials are under 100. Measurement of the dielectric permittivity is usually made using a weak A.C. field (10 V/cm) [11] and measuring the charge stored,

$$Q = CV \ . \qquad [3]$$

This results in a measurement of the capacitance, C, which is directly related to the dielectric permittivity;

$$C = \frac{\varepsilon\varepsilon_o A}{d} \ . \qquad [4]$$

The area and thickness of the capacitative device are represented by A and d, respectively.

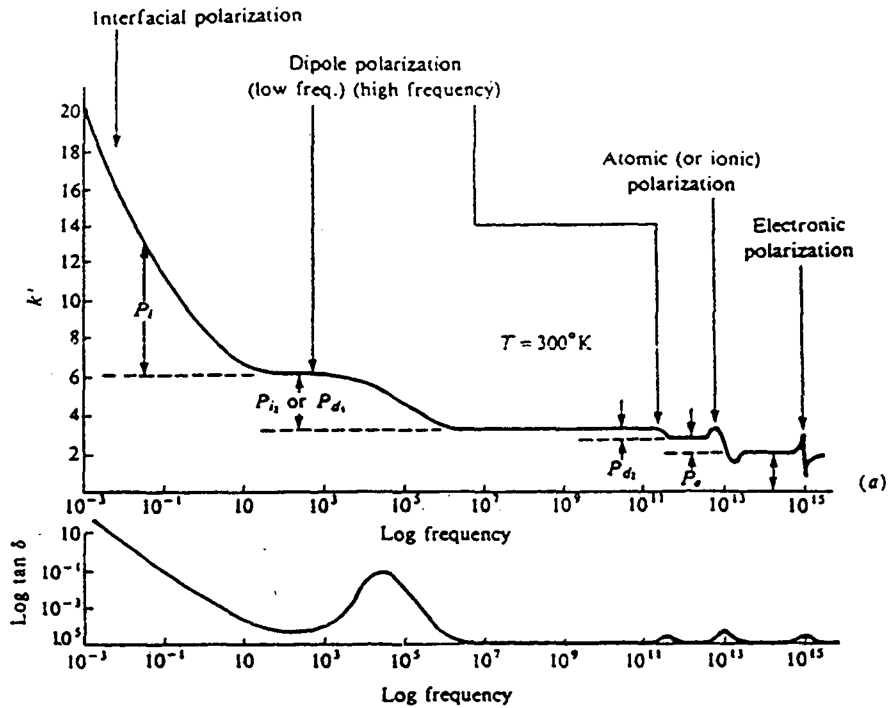


Figure 2. Frequency dependence of the polarization mechanisms in dielectrics. (a) Dielectric permittivity (k'). (b) Dielectric loss or dissipation (tan δ).[12]

The frequency dependence of the dielectric permittivity arises from the finite time it takes for the various polarization mechanisms to develop. Figure 2a shows the frequency dependence of the four polarization mechanisms: interfacial, dipole, atomic and electronic polarization. Interfacial and dipole polarization are strongly temperature dependent while atomic and electronic polarization are not. Interfacial or space-charge polarization can contribute to the dielectric permittivity up to about $10^3$ Hz. It arises from the diffusion of mobile charges over many atomic spacings. These charges pile up at interfaces within the dielectric, and produce localized polarization of the material. Dipole polarization arises from the rotation of permanent molecular dipoles, or reorientation of weakly bound dipoles to other equilibrium positions. The molecular dipoles and weakly bound equilibrium dipoles respond to electric fields varying at frequencies up to $10^{11}$ - $10^{12}$ Hz and $10^3$ - $10^6$ Hz, respectively.

Atomic or ionic polarization can follow frequencies up to $10^{12}$ to $10^{13}$ Hz and is due to the shift of ions relative to one another. Electronic or optical polarization arises from a shift of the valence electron cloud of ions with respect to the positively charged nucleus and reaches the highest frequencies, up to $10^{15}$ Hz.[13,14] Above these frequencies polarization effects vanish and the relative dielectric constant returns to unity.

The frequency dependence of the polarization also gives rise to a time lag or phase difference (90° - δ) between the externally applied alternating field and the current. The long - range migration of charges and/or the energy dissipation due to the rotation or oscillation of dipoles gives rise to this effect, which is expressed by the dielectric loss,

$$D = \tan\delta = \frac{\varepsilon'}{\varepsilon''}, \qquad [5]$$

where $\varepsilon = \varepsilon' + i\,\varepsilon''$ is the complex dielectric constant. Large values of dielectric loss occur when the polarization mechanisms cannot keep up with the applied field fluctuations, Figure 2b. A "lossy" dielectric extracts energy from the electric field and produces heat.[15] The loss can also be expressed in terms of equivalent resistances. For a series RC circuit,

$$D = \omega RC\ , \qquad [6]$$

where $\omega$ is the A.C. frequency, R is the resistance, and C is the capacitance. The loss in a parallel RC circuit is expressed as

$$D = \frac{1}{\omega RC}\ . \qquad [7]$$

Large values of loss, $D > 0.1$, indicate a high-loss material, in the extreme case a pure resistor, and $D < 0.01$ represents a low-loss material approaching a pure capacitor. The resistance of a material can be expressed independent of geometry as the resistivity,

$$\rho = \frac{RA}{d}. \qquad [8]$$

The value of resistivity is used to characterize the material: the resistivity of metals ranges from $10^{-2}$ - $10^{-6}$ $\Omega$-cm, semiconductors 1 - $10^{10}$ $\Omega$-cm, and insulators $10^{14}$ - $10^{22}$ $\Omega$-cm.

The presence of point defects can enhance ion migration (ionic conduction) in ionic materials resulting in high dielectric loss or metallic properties. Ionic conductivity occurs by the hopping of ions between available sites; whether interstitial or vacancy. The probability that a jump occurs depends on the energy barrier that the ion must overcome, availability of sites, and the energy supplied or the temperature. In the absence of a field, the jumps occur in random directions and the process is termed self-diffusion. An applied electric field lowers the energy barrier to the ion in one direction and increases it in the opposite direction, and leads to a net charge flow. The height of the energy barrier is also influenced by the valency and size of the ions; smaller radius and lower valence ions give rise to lower energy barriers.[16,17] In the absence of impurities, vacancy sites due to non-stoichiometry and Schottky defects are the primary enablers of conductivity in most ionic materials. Non-stoichiometry arises from the stability of multiple oxidation states. In order to maintain charge neutrality, the presence of different oxidation states leads to anion or cation vacancies. Schottky defects are corresponding anion and cation vacancies. Ionic conductivity follows an exponential dependence on the inverse of absolute temperature, Figure 3. The different slopes in the schematic indicate the two different activation energies. The larger slope at higher temperatures shows the ionic conductivity dependence on temperature for vacancy formation and the ion migration to neighboring sites. At lower temperatures, the slope decreases because the conductivity depends only on ion migration. Grain boundaries may also enhance migration of ions by providing an interface that is rich in point defects. The permittivity will depend on the concentration of defects. Migrating ionic charge can affect the polarization of the crystal because the charge is no longer bound to stable states and therefore cannot contribute to the dipole polarization. Another disturbance to the polarization is caused by vacancies; their

presence alters the potential that the ions feel. It is reasonable to expect that this effect is pronounced for Schottky defects because there is also a net decrease in the absolute charge.

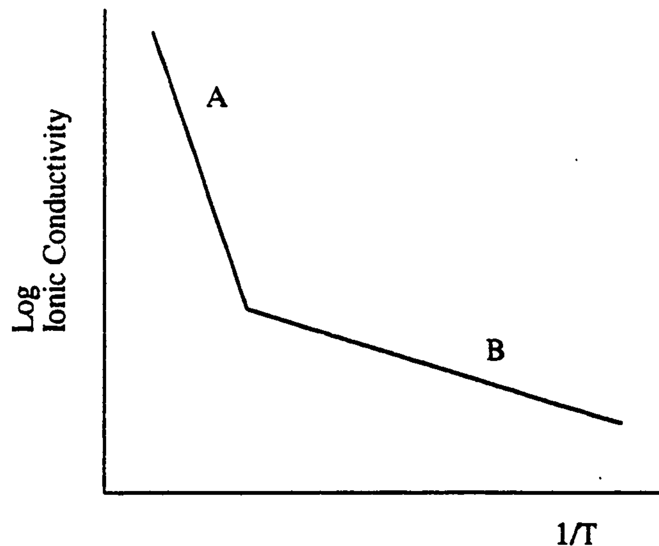


Figure 3. Ionic conductivity vs. temperature. Slope A corresponds to the activation energy necessary to form a vacancy and move a neighboring ion to this site, and slope B is the activation energy only for the migration of the ion.

Heterogeneities within an ionic material may give rise to further changes in electrical properties. A sharp composition gradient present at one of the electrode-material interfaces due to interfacial polarization, heat treatment, or atmospheric attack can lead to a two-layer capacitor. By modelling the capacitors in series, an expression for the averaged measured dielectric permittivity, $\varepsilon_m$, can be found;

$$\varepsilon_m^{-1} = (1-V_1)\,\varepsilon_2^{-1} + V_1\varepsilon_1^{-1}\,, \qquad [9]$$

where the subscripts 1 and 2 refer to the capacitor layers and $V_1$ to the volume fraction of layer 1. A dielectric containing rods of material with permittivity (subscript 1) different from their surroundings (subscript 2) and extending from one electrode to another, is modelled as parallel capacitors:

$$\varepsilon_m = (1-V_1)\,\varepsilon_2 + V_1\varepsilon_1 \qquad [10]$$

A random dispersion of spheres (subscript 1) leads to the following expression:

$$\varepsilon_m = \varepsilon_2\left(1+\frac{3V_1(\varepsilon_1 - \varepsilon_2)}{\varepsilon_1 + 2\varepsilon_2 - V_1(\varepsilon_1 - \varepsilon_2)}\right) \qquad [11]$$

The last two equations indicate that changes in the dielectric permittivity due to the presence of other phases follow roughly Vegard's law of mixtures. These models assume that the different regions in the material are ideal dielectrics. If they are not ideal, then Equation 10 is still appropriate for the parallel model. For non-ideal dielectrics the sphere and two-layer capacitor models follow the behavior of the dielectric permittivity and loss for interfacial polarization as shown in Figure 2. A peak of the loss as a function of frequency may be observed depending on the quantity and conduction of each phase. Since the conduction depends exponentially on temperature, the observed loss peak will shift to higher frequencies with increasing temperature.[18,19]

A significant electric field can also lead to changes in dielectric properties via dielectric breakdown. Dielectric breakdown produces an electrical short across the material under the application of an electric field. This happens when the temperature or thermal energy of the lattice or its electrons is such that the conductivity increases rapidly, damaging the material. The three basic types of breakdown are intrinsic, thermal and discharge. Intrinsic breakdown occurs when the applied field accelerates the electrons to the extent that they ionize the lattice ions. Thermal breakdown occurs when the operating or test conditions heat the lattice to temperatures that allow the lattice ions to be ionized. Discharge breakdown occurs in porous ceramics where there is occluded gas that ionizes. Material properties that affect the dielectric

strength include: material texture, particle alignment, stress distribution, porosity, surface condition, grain boundary effects, point defects, dislocations, and dielectric permittivity.[20,21]

## 2.2. Ferroelectricity

Ferroelectric materials are a sub-class of pyroelectric materials (see Appendix A). Pyroelectrics are non-linear dielectric materials that exhibit spontaneous polarization, $P_s$, in the absence of an applied field. The total polarization of a pyroelectric can be written as

$$\mathbf{P} = (\varepsilon-1)\varepsilon_o\mathbf{E} + \mathbf{P_s} \cdot \qquad [12]$$

The pyroelectric effect is the change in the spontaneous polarization with temperature;

$$\mathbf{p} = \frac{d\mathbf{P_S}}{dT} \, , \qquad [13]$$

where **p** is the pyroelectric coefficient. The spontaneous polarization forms from molecular and/or ionic dipoles and may not always be observed because the displacement and reorientation of ions and charged molecular units takes a finite time.[22] Therefore, if the change in temperature occurs slowly, charge compensation of the dipoles occurs and the pyroelectric effect may not be observed.[23] In conductors, compensation occurs almost instantaneously because electronic charges within the crystal are free to rearrange neutralizing the electric dipole. In insulators, free charges in the surrounding medium can flow to the surfaces and neutralize the electric dipole.[24] In addition, if there is more than one direction of the spontaneous polarization, as in ferroelectric and polycrystalline pyroelectric materials,[25] the opposing dipoles can cancel each other out to produce a zero net-spontaneous polarization.

Ferroelectric materials differ from pyroelectric materials in that the spontaneous polarization can be reversed by the application of an electric field resulting in hysteresis in the

polarization vs. electric field behavior (ferroelectricity). Ferroelectric materials are also characterized by a transition or Curie temperature, $T_c$. At the transition temperature, the material transforms from a high-temperature non-polar paraelectric phase to a low-temperature ferroelectric phase. Below $T_c$, in the ferroelectric phase, the material exhibits spontaneous polarization. This spontaneous polarization increases as the temperature decreases. A rapid change in spontaneous polarization occurs at the transition temperature resulting in a large pyroelectric coefficient. Large piezoelectric, dielectric, and specific heat coefficients are also observed in the vicinity of the transition temperature.

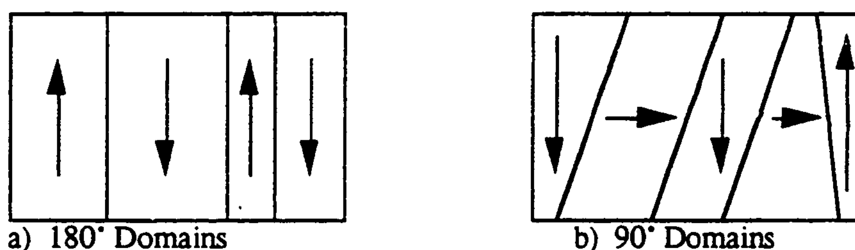


Figure 4. Schematic of domains in ferroelectric crystals.

In the ferroelectric phase, the spontaneous polarization of ferroelectrics has more than one orientation resulting in domains. The directions of these polarization vectors, and thus domains, can be changed by application of a sufficient electric field.[26] The spontaneous polarization of ferroelectrics is due to dipole and/or ionic polarization.[27] The displacements of small, high-valence cations lead to the large dipole moments responsible for the spontaneous polarization.† The closely spaced ions result in a strong dipole-dipole interaction.[28] To minimize their energy, neighbor dipoles polarize in the same direction. This leads to domains of uniform polarization analogous to the domains formed by magnetic dipoles in ferromagnetic

† The anions and other cations within the material also displace; however, the majority of the displacement can usually be associated with one of the cation species.

materials. The domain walls of ferroelectric materials are, however, much narrower (1-2 atomic spacings) compared to the Bloch wall of ferromagnetic materials (750 Å).[29] The Bloch wall width in ferromagnetic materials is determined by competition between the exchange energy to increase the wall width (alignment of spins) and the anisotropy to decrease the wall width.[30] The anisotropy is the orientation of the spins in lower energy orientations determined by the crystal lattice. In ferroelectric crystals the large anisotropic effect leads to domain orientations corresponding to unique polarization axis of the ferroelectric.[31] Figure 4 a) shows a possible domain structure of a ferroelectric material, such as potassium dihydrogen phosphate, with two spontaneous polarization orientations. In KDP spontaneous polarization occurs in both directions along the c-axis in the orthorhombic phase, and results in domains oriented against each other by 180°. Ferroelectric materials that exhibit spontaneous polarization in either direction along three perpendicular crystallographic axes exhibit 90° and 180° misoriented domains as shown in Figure 4 b).[32]

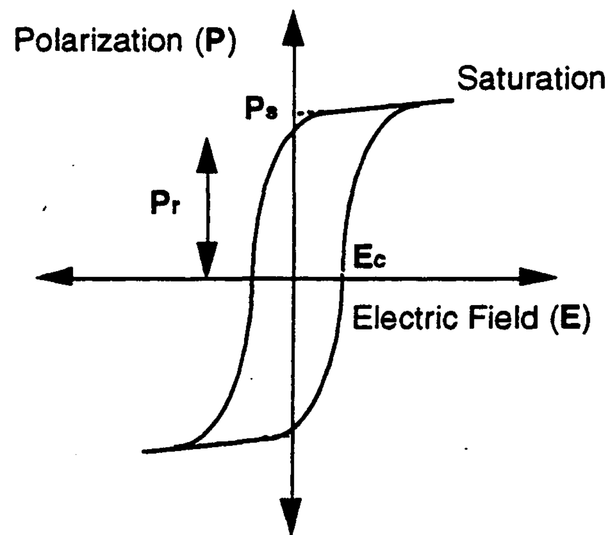


Figure 5. Polarization vs. electric field of a ferroelectric phase.

It is possible to reorient the domains with the application of an external electric field. The change in the polarization along a ferroelectric axis with electric field results in a hysteresis loop, as demonstrated by Figure 5. The hysteresis arises from the double potential well, shown in Figure 6, that the charged cation experiences along the ferroelectric axis. As an electric field is applied along the ferroelectric axis, the cations move from one potential well (polarization) to the other. The polarization increases rapidly until all cations occupy the same potential well (saturation) and a linear regime takes over as in a linear dielectric.† If the external electric field is reversed, the atoms return along the linear saturation region and then begin to switch from the current well to the other well, reversing the polarization. The hysteresis occurs because of the energy barrier between the two wells. In other words; there is an activation energy that must be overcome to reverse the total polarization of the crystal, that energy is also expressed as the coercive electric field ($E_c$). The area within the hysteresis loop is a measure of the energy required to reverse the polarization twice. The spontaneous polarization ($P_s$) and the remanent polarization ($P_r$) will be different if some of the dipoles reverse their polarization before the applied field reverses. This occurs because there can be a range of field strengths for reversing the dipoles due to interface, surface and defect states.[33]

† In a linear dielectric the charged species sit in a symmetrical single potential well.

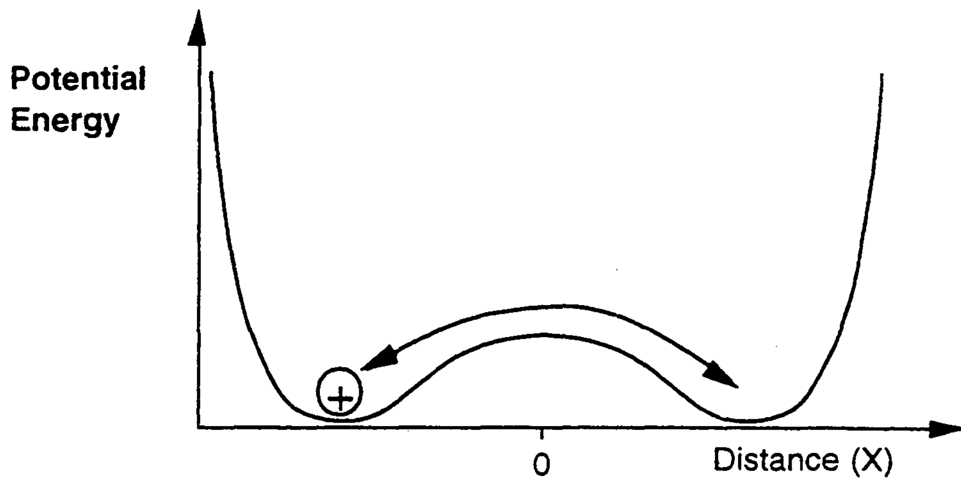


Figure 6. A double potential well experienced by charged species along a ferroelectric axis (X).

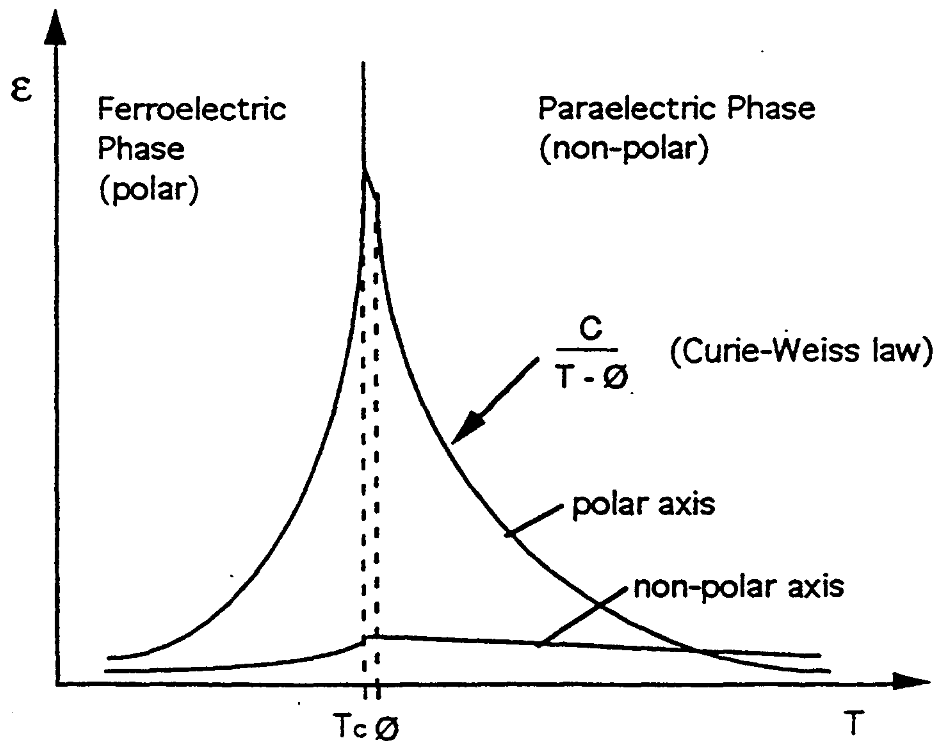


Figure 7. Dielectric permittivity vs. temperature of a polar and non-polar axis of a ferroelectric material.[34]

At the Curie temperature, $T_c$, a reversible phase transition occurs in a ferroelectric material. Typically, the material transforms from a high-temperature, high-symmetry, non-polar or paraelectric phase to a low-temperature, lower-symmetry ferroelectric phase. Below $T_c$, in the ferroelectric phase, the material exhibits spontaneous polarization. This spontaneous polarization decreases as the Curie temperature is approached from below. The temperature at which the phase transformation occurs, $T_c$, is the temperature at which the spontaneous polarization falls to zero. In addition, these phase transformations are marked by a peaks in the dielectric constant along the polar axis at $T_c$. Figure 7 shows a plot of the dielectric permittivity vs. temperature across the transition temperature for a polar and non-polar axis of a ferroelectric crystal. This plot is different for ferroelectric materials that exhibit cubic symmetry in their paraelectric phase because there is no non-polar permittivity in the paraelectric phase; any one of the three axes have the possibility of becoming the polar axis of the ferroelectric material. Other anomalies occur in the piezoelectric, pyroelectric, and specific heat coefficients at $T_c$. Above the Curie temperature, in the non-polar (or paraelectric) phase, the dielectric constant obeys the equivalent of the Curie-Weiss behavior observed in ferromagnetic materials,

$$\varepsilon = \frac{C}{T - \varnothing} \qquad [14]$$

where C is the Curie constant. The Curie constant and the Curie-Weiss temperature, Ø, are unique to each ferroelectric transition; Ø and $T_c$ may differ by as much as 10° C.[35]

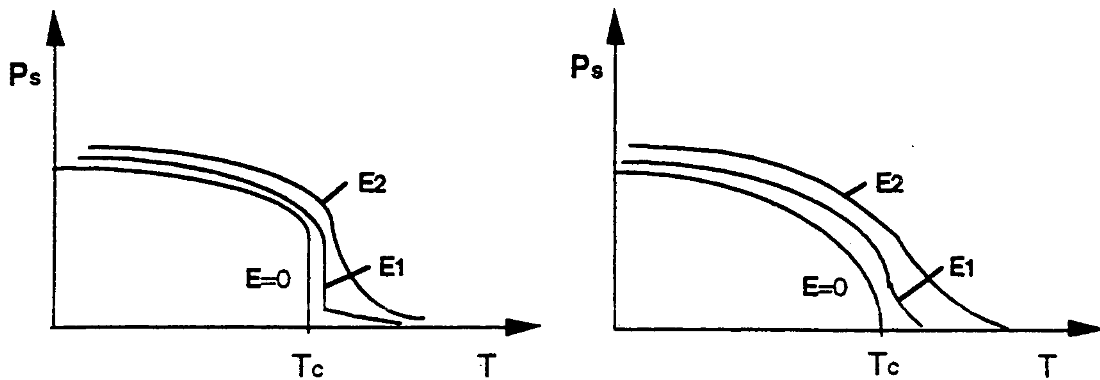


a) 1st-order phase transformation b) 2nd-order phase transformation

Figure 8. Spontaneous polarization vs. temperature for three values of bias, $E_2 > E_1 > 0$.

The spontaneous polarization of the ferroelectric phase decreases and falls to zero at the Curie temperature, as shown in Figures 8 a) and b). The type of phase transformation influences the behavior of the spontaneous polarization near the Curie temperature. In a first-order transformation, the spontaneous polarization changes discontinuously at the Curie temperature, while in a second-order transformation the spontaneous polarization changes more gradually as the Curie temperature is approached, as illustrated in Figures 8 a) and b), respectively. For these figures, the crystals are non-polar above the Curie temperature, resulting in a negative $dP_s/dT$. Only one ferroelectric is known to have a positive $dP_s/dT$; Rochelle salt (sodium potassium tartrate) has a ferroelectric phase bounded by two non-polar phases.

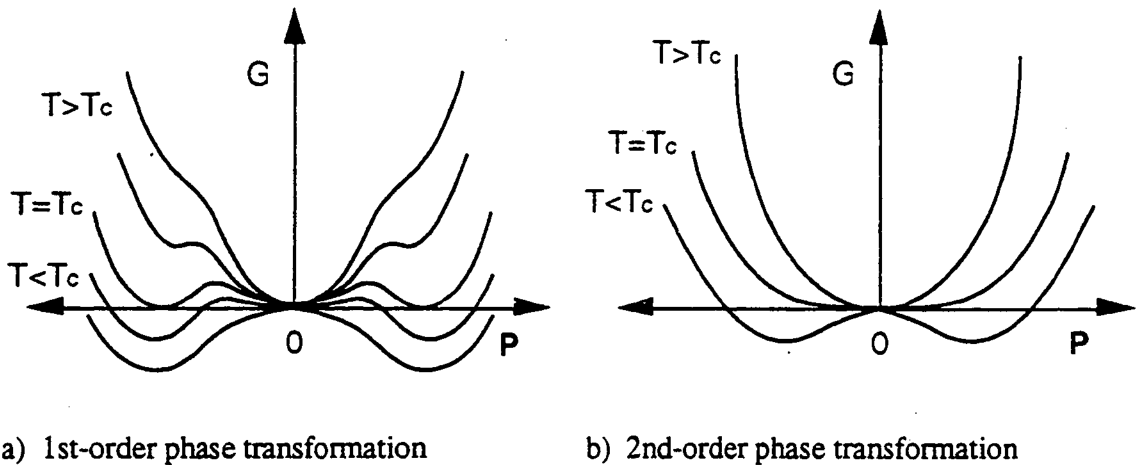


a) 1st-order phase transformation b) 2nd-order phase transformation

Figure 9. Free energy (G) vs. polarization (P)

In a first-order transition, the onset of spontaneous polarization occurs more rapidly than in the second-order transition and exhibits temperature hysteresis. The differences in first- and second-order transitions can be seen directly from the free energy vs. polarization curves for first- and second-order ferroelectric-paraelectric phase transitions as shown schematically in Figures 9 a) and b). The form of these curves was developed by Devonshire[36] who showed that the free energy, G, of a ferroelectric under zero stress can be expressed by a Taylor expansion,

$$G = \frac{1}{2}\chi P^2 + \frac{1}{4}\xi P^4 + \frac{1}{6}\zeta P^6 + \ldots, \qquad [15]$$

where the coefficients $\chi$, $\xi$ and $\zeta$ are functions of the temperature. The behavior of the dielectric permittivity and spontaneous polarization as a function of temperature and electric field can be extracted from these free energy curves. Devonshire further showed that with the application of a D.C. bias (electric field) the transition becomes more gradual, as shown in Figures 8 a) and b), and the polarization vs. temperature curve is no longer discontinuous for a first-order transition. In real crystals, the sharpness of the transition and temperature

hysteresis can also be blurred by the presence of impurities, internal stresses, and crystal defects.

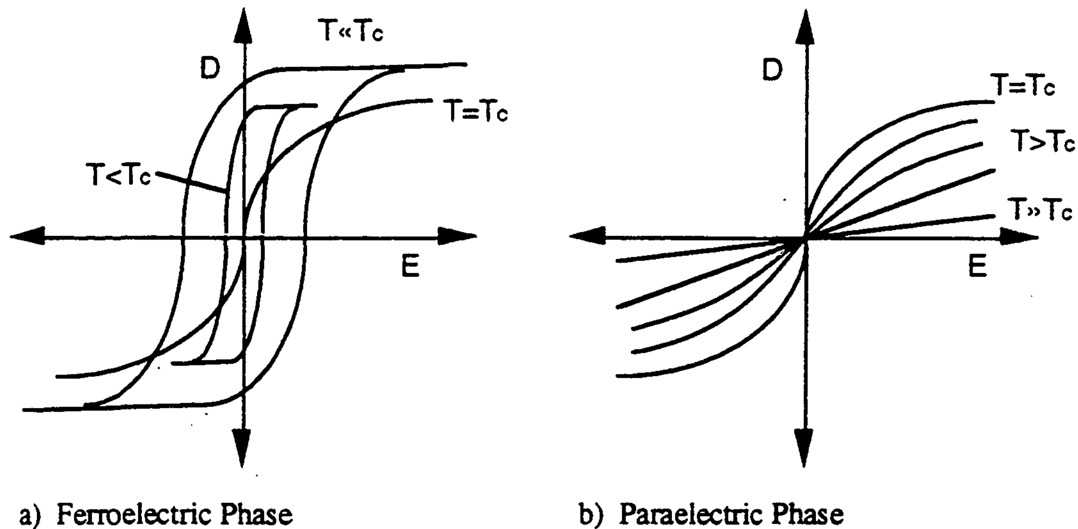


a) Ferroelectric Phase b) Paraelectric Phase

Figure 10. Electric displacement (D) vs. electric field (E) of a ferroelectric.

The temperature and electric field affect the values of the pyroelectric coefficient and dielectric permittivity which, as will be discussed in Chapter 3, are central to the response of the pyroelectric detector. Plotting polarization vs. temperature and electric field in three dimensions and taking two-dimensional cuts results in the polarization curves demonstrated in Figures 10 a) and b). The ferroelectric phase exhibits a hysteresis loop that changes with temperature near the Curie temperature. In the paraelectric phase ($T > T_c$) the ferroelectric material behaves as a nonlinear dielectric. Far above the Curie temperature the ferroelectric behaves as a linear dielectric.

## 2.3. Structure

Eleven of the thirty-two crystal classes are centrosymmetric and therefore cannot possess polar properties. The absence of a center of symmetry in twenty of the remaining crystal classes allows them to exhibit piezoelectricity (See Appendix A for classification of different crystal systems and symmetry groups.).† Ten crystal classes out of these twenty exhibit spontaneous polarization or pyroelectricity.[37] The ferroelectric materials within these ten crystal classes can be divided into two groups. In the first group the prototype structure is orthorhombic ($D_2$) or tetragonal ($D_{2d}$) when non-polar. The ferroelectrics in this group have only one polar axis, leading to two directions of polarization. The second group is made up of ferroelectrics with the perovskite structure. The prototype phase for the perovskite structure has complete cubic symmetry ($O_h$) leading to several equivalent polarization directions.[38] Ferroelectric materials making up the first group of materials are not centrosymmetric and thus are piezoelectric in their prototype phase unlike the perovskite ferroelectrics.

The perovskite structure has the chemical formula $ABO_3$ (Figure 11). The A site is located at the cube corners and is inhabited by either a di- or monovalent metal; the B site resides in the center of the cube and is either a tetra- or pentavalent metal, and the cube faces are filled by oxygen. The perovskite structured ferroelectrics typically have several ferroelectric phases, leading to ferroelectric–ferroelectric transitions. The highest temperature transition occurs between the paraelectric cubic and tetragonal ferroelectric phases. This transformation occurs via a tetragonal distortion in the direction of one of the three <100> cube axes, Figure 12 a. The B ion displaces in either direction along the tetragonal axis, leading to six polarization directions. The next transition occurs from the ferroelectric tetragonal to the ferroelectric orthorhombic ($C_{2v}$) phase. The distortion for this transformation occurs along the

† The one exception, although without a center of symmetry, has other symmetry elements that combine to exclude piezoelectric activity.

pseudocubic face diagonal, [110], and results in twelve polarization directions, Figure 12 b. Similarly the transformation from the orthorhombic to rhombohedral ($C_{3v}$) phase occurs via a body diagonal distortion, [111], resulting in eight polarization directions, Figure 12 c.[39] The large number of polarization directions for each of these ferroelectric perovskite phases results in complex domain patterns.

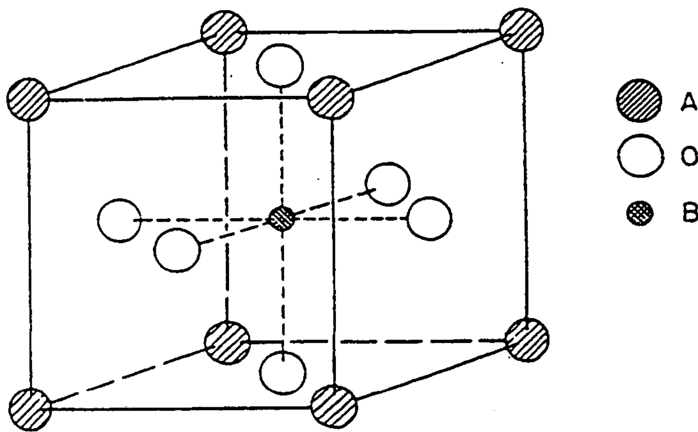


Figure 11. Cubic perovskite-type structure $ABO_3$.[40]

Materials with the perovskite structure often have an polymorphic pyrochlore phase that is cubic. The polymorphic nature means that transformation between the two phases requires no long range diffusion, only a rearrangement of atoms. The composition of the normal pyrochlore structure is $A_2B_2O_6O'$ with four crystallographically nonequivalent types of atoms.† The pyrochlore phase is typically ionic and complicated in structure; Figure 13 shows

† The O' indicates oxygen sites within the lattice that are different in symmetry than the non-superscripted oxygen.

the pyrochlore structure as derived from a fluorite lattice. The cubic lattice parameter of pyrochlore structures is typically on the order of 10 - 11 Å. The exact position of the O atoms also varies with the pyrochlore, the arrows indicate the orientation of the adjustment. A defect pyrochlore phase also exists that contains anion and/or cation vacancies: $A_2B_2O_6O'_{1-x}[]_x$ $(0 < x < 1)$ and $AB_2O_6$. The large numbers of vacancies present in these defected structures can lead to metallic properties due to large ionic conductivities; however, pyrochlores can also be semiconducting or insulating.[41]

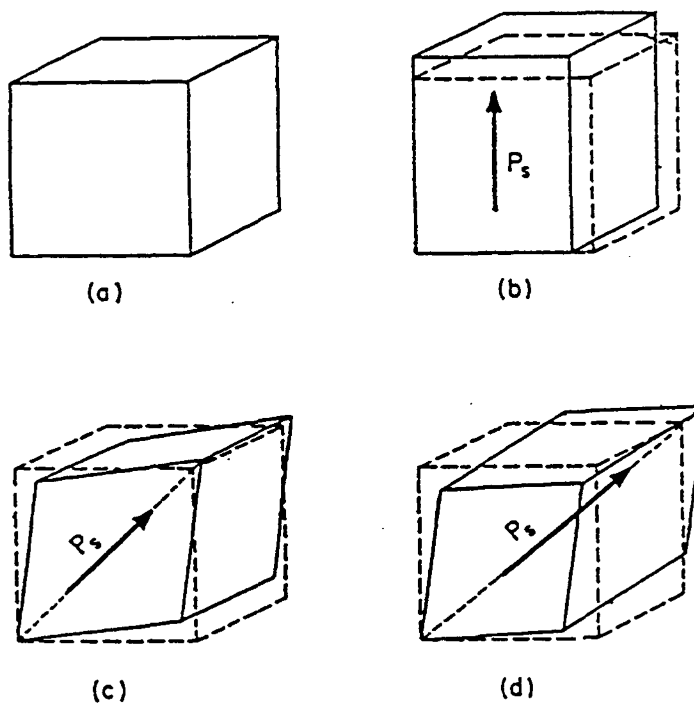


Figure 12. Crystallographic changes of the perovskite structure.[42]

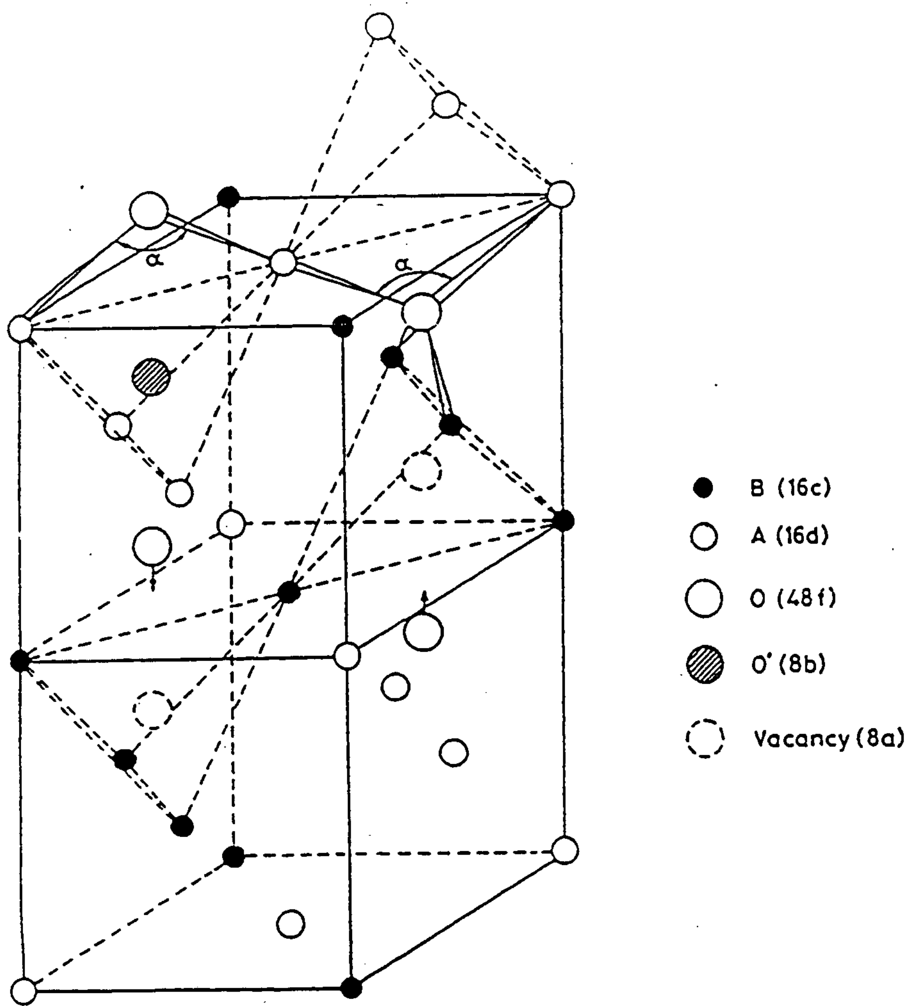


Figure 13. Pyrochlore structure as derived from the fluorite lattice. The cation positions for one quarter of the unit cell are shown.[43]

## 2.4. Electromechanical Behavior

Piezoelectricity and electrostriction describe the electromechanical behavior of materials. Application of an electric field to a piezoelectric material results in strains directly proportional to the field. Piezoelectricity also has a converse effect, applying stress results in a potential difference forming across the material. The piezoelectric effect occurs only in non-centrosymmetric material phases. Electrostriction occurs in all materials but has no converse effect. In electrostrictive materials the strain is proportional to the square of the applied field; the resultant strains are generally smaller than those of piezoelectric origin. The electromechanical behavior of piezoelectric materials can be described in terms of measurable properties by the free energy function of the electrical enthalpy, H:

$$\dot{H} = T_{ij}\dot{S}_{ij} - P_i\dot{E}_i \,, \qquad [16]$$

where: T - stress, S - strain, P - polarization, and E - electric field. The physical constants relating these measurable quantities are defined by the following equations:

$$T_{ij} = -c^{E}_{ijkl}S_{kl} + e_{kij}E_k \qquad [17]$$

$$P_i = e_{ikl}S_{kl} + \eta^{S}_{ij}E_k \qquad [18]$$

$$S_{ij} = -s^{E}_{ijkl}T_{kl} + d_{kij}E_k \qquad [19]$$

$$P_i = -d_{ikl}T_{kl} + \eta^{T}_{ik}E_k \qquad [20]$$

$$S_{ij} = -s^{P}_{ijkl}T_{kl} + b_{kij}P_k \qquad [21]$$

$$E_i = b_{ikl}T_{kl} + \chi^{T}_{ik}P_k \qquad [22]$$

$$T_{ij} = -c^{P}_{ijkl}S_{kl} + a_{kij}P_m \qquad [23]$$

$$E_i = -a_{ikl}S_{kl} + \chi^{S}_{ik}P_k \,. \qquad [24]$$

The physical constants are: c - elastic stiffness (N/$m^2$), e - piezoelectric constant (C/$m^2$), $\eta$ ($\varepsilon\varepsilon_o$) - permittivity component (F/m), s - elastic compliance constant ($m^2$/N), d - piezoelectric constant (C/N or m/V), b - converse piezoelectric constant ($m^2$/C), $\chi$ - inverse permittivity component (m/F), and a - converse piezoelectric constant (N/C). Equations [18] and [20] show that the dielectric component (permittivity) of piezoelectric materials is not simply a function of the polarization but is also influenced by the presence of stress or strain through the piezoelectric coefficients. In a non-piezoelectric phase the piezoelectric coefficients are zero and terms that are second order in polarization must be taken into account in the stress and strain equations.

Relationships between the various constants can be obtained by substituting Equations [17] - [24] for each other. The resulting relationships are particularly interesting for ferroelectric materials because anomalous behavior in one constant can be used to predict anomalous behavior in other constants. In addition, the relationships explain large differences in constants measured under different conditions. For example the dielectric permittivity can be measured at constant stress (free) or constant strain (clamped). In a ferroelectric material the measured values will be different. Under constant strain or at high frequencies (> $10^{12}$ - $10^{13}$ Hz), dielectric relaxation of the ionic polarization will occur resulting in a lower dielectric permittivity than that measured for a free crystal at low frequency. In non-piezoelectric materials, the clamped and free values of dielectric permittivity will be identical.[44,45]

In diffuse ferroelectrics the situation is more complicated. A diffuse or relaxor ferroelectric material has a broadened phase transition due to structural disorder, or composition fluctuations occurring in solid solutions. Composition variations lead to nanoregions of the material that posses a range of transition temperatures. Structural disorder can also broaden the phase transition if frozen-in (< 400°C) defects are clustered. The broadening of the phase transition translates to a broadened and lowered dielectric permittivity

peak, and ferroelectric and piezoelectric behavior above the 'averaged' ferroelectric transition temperature.[46]

## 3. Pyroelectric Detectors

### 3.1. Signal Formation

Pyroelectric detectors are thermal detectors that use the temperature-dependent spontaneous polarization, or pyroelectric effect, to detect incident radiation. Pyroelectric materials are dielectric materials that belong to the family of dielectric materials and possess a spontaneous electrical polarization that appears in the absence of an applied electrical field or stress. From Equation [12] it is apparent that the pyroelectric coefficient **p**, the derivative of polarization P with temperature T, has contributions from the dielectric permittivity and spontaneous polarization terms,

$$\mathbf{p} = \frac{d\mathbf{P}}{dT} = \left[\frac{d\varepsilon}{dT}\right]_{\mathbf{E}} \varepsilon_0 \mathbf{E} + \left[\frac{d\mathbf{P}_s}{dT}\right]_{\mathbf{E}} . \qquad [25]$$

In the absence of a D.C. bias or when the dielectric permittivity is temperature independent, the first term in Equation 25 is zero and the value of the pyroelectric coefficient depends only on the spontaneous polarization, $P_s$. There are two modes of operation for a pyroelectric detector: pyroelectric and dielectric (bolometer). The "true" pyroelectric mode can only be operated in the pyroelectric or ferroelectric state of the material while the dielectric mode becomes active through the application of a biasing field and, therefore, it can also be operated in the paraelectric phase of the material. In the "true" pyroelectric mode, large changes in the spontaneous polarization with temperature near ferroelectric phase transitions lead to large pyroelectric coefficients. However, there are two advantages to working in the dielectric bolometer mode. The first is that larger pyroelectric coefficients can be achieved for operation with an electric field. This can be explained by the occurrence of a remanent polarization or rounded hysteresis loop that is due to defects and domains in the ferroelectric. The second advantage is that lower losses are typically realized by the application of an electric field which

impedes domain boundary motion.[47] Therefore, the optimum detector response is a function of the applied electric field and temperature.[48]

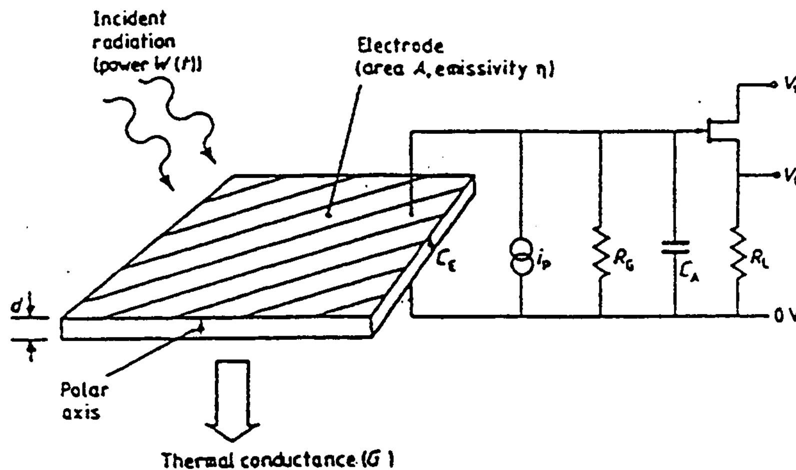


Figure 14. Schematic diagram of a pyroelectric detector.[49]

Pyroelectric detectors are currently used in room temperature devices such as fire alarms, motion sensors, thermal imagers, and gas analyzers. A pyroelectric detector, Figure 14, is a capacitor whose spontaneous polarization vector is oriented normal to the plane of the electrodes. Incident radiation absorbed by the pyroelectric material is converted into heat, resulting in a temperature variation (dT) and thus, the magnitude of the spontaneous polarization. Changes in polarization alter the surface charge of the electrodes, resulting in a pyroelectric current in the external circuit,

$$i_p = Ap\frac{dT}{dt} \quad . \qquad [26]$$

The pyroelectric current depends on the temperature change with time; therefore, pyroelectric devices are considered to be 'AC coupled' to any temperature changing effect.[50]

Determining the electrical response of a pyroelectric detector requires analysis of both the thermal and electrical circuits. Measurement of the electrical response is usually made using the detector arrangement shown in Figure 14. The simplest arrangement is to suspend the detector element in a vacuum by its wire leads. The wire leads carry charge to and from the electrodes and are also used to control the thermal conductance (G) between the element and its heat sink. The charge displaced from the electrodes is very small and thus requires an amplifier; the total spontaneous polarization of a ferroelectric capacitor is on the order of hundreds of nanocoulombs for a 1mm$^2$ device.

A pyroelectric detector is typically exposed to a sinusoidally modulated beam of radiation carrying power,

$$P = P_o\,(1 + e^{i\omega t}) \qquad [27]$$

at an angular frequency, $\omega$. Thermal sources usually produce continuous radiation. It is necessary to modulate the incoming radiation to obtain a thermal gradient, which produces the pyroelectric current expressed in Equation 26. Typically, modulation of the radiation is achieved by mechanical chopping with a rotating slotted disc.[51]

Absorption of the incident radiation results in a temperature rise ($\theta$) of the sensor. The thermal response of the sensor to this temperature change depends on the heat capacity (H) of the detector, the quantum efficiency or fraction of absorbed photons ($\eta$) and the thermal conductance (G) coupling the detector to its surroundings. The combined effect of these factors is described by the equation for a thermal circuit,[52]

$$\eta P = H\frac{d\theta}{dt} + G\theta \qquad [28]$$

Solving Equation 28 for the sinusoidal power fluctuations given in Equation 27 results in a temperature fluctuation amplitude $\theta_\omega$ of the detector,

$$\theta_\omega = \eta P \left(G^2 + \omega^2 H^2\right)^{-1/2} \quad [29]$$

The phase difference between the incident radiation and the temperature oscillations is given by

$$\phi = \tan^{-1}(\omega H/G) \quad [30]$$

and the thermal time constant is

$$\tau_T = \frac{H}{G} = \frac{cAd}{G} \quad [31]$$

The specific heat of the detector material and the area and thickness of the detector are c, A and d, respectively.

The thermal conductance between the detector element and its surroundings is the sum of its radiative conductance ($G_R$) and the thermal conductance of the wire links ($G_w$).

$$G = G_R + G_w \quad [32]$$

The radiative conductance is given by the Stefan-Boltzmann Law of thermal radiation,

$$G_R = 4\eta\sigma T^3 A_R, \quad [33]$$

where $\sigma$ is the Stefan-Boltzmann constant and $A_R$ is the radiating area with emissivity, $\eta$. The thermal conductance through a wire is

$$G_w = \frac{\kappa A_w}{l} \quad [34]$$

where $\kappa$ is the thermal conductivity, $A_w$ is the cross-sectional area and l is the length of the wire.[53]

The current responsivity[54] is defined as the current per watt of incident power,

$$R_i = \frac{i_p}{P_o} \quad [35]$$

Inserting Equations 26, 27 and 29 into Equation 35 and rearranging results in

$$R_i = \frac{\eta p A \omega}{G\left(1+\omega^2\tau_T^2\right)^{1/2}} \qquad [36]$$

To determine the voltage response of the device the electrical circuit of Figure 14 must be considered. The voltage response of the detector measured at the gate of the amplifier is,

$$R_V = \frac{V}{P_o} = \frac{i_p |Z|}{P_o} \qquad [37]$$

depends on the electrical impedance of the circuit,

$$|Z| = \frac{R}{\left(1+\omega^2\tau_E^2\right)^{1/2}} \qquad [38]$$

where $\tau_E = RC$ is the electrical time constant for the circuit shown in Figure 14. The total circuit capacitance and resistance are, respectively, $C = C_E + C_A$ and $R = (1/R_E + 1/R_G + 1/R_L)^{-1}$, see Figure 14. Combining Equations 35, 36, 37 and 38 results in the following voltage response:

$$R_V = \frac{\eta p A \omega R}{G\left(1+\omega^2\tau_T^2\right)^{1/2}\left(1+\omega^2\tau_E^2\right)^{1/2}} \qquad [39]$$

To achieve the greatest voltage response, the impedance of the detector-load circuit and the current response must be maximized. The impedance is maximized with large R, and small $\omega$ and C. The current response, Equation 36, is maximized with large $\eta$ and **p**, and small c and d.

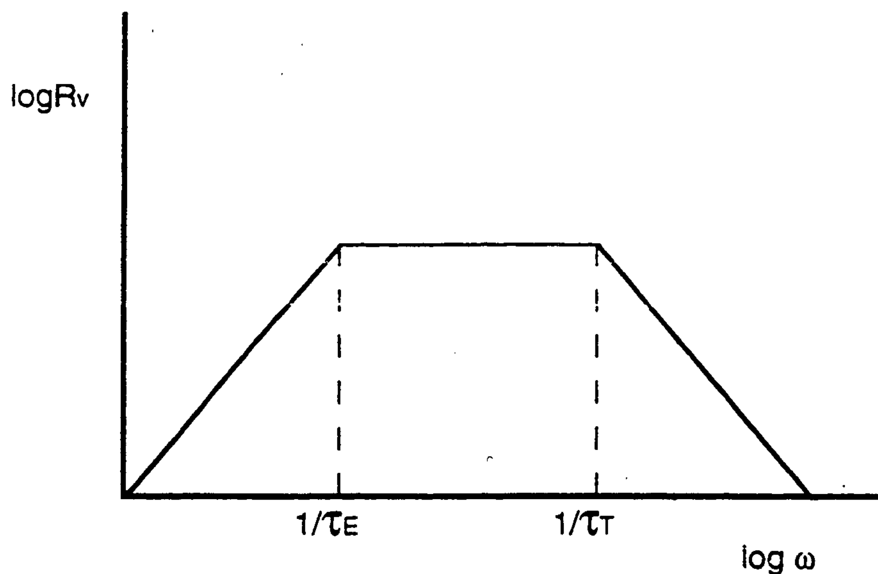


Figure 15. Schematic log-log plot of the voltage responsivity vs. chopping frequency of the incoming radiation.

Table 1. Voltage Responsivity vs. Time Constants and Chopping Frequency.

| | Low Frequency | Med. Frequency | High Frequency | |
|---|---|---|---|---|
| $\tau_T > \tau_E$ | $\frac{\eta p A \omega R}{G}$ [40] | $\frac{\eta p R}{cd}$ [41] | $(C_E > C_A)$ | $(C_A > C_E)$ |
| $\tau_T < \tau_E$ | | $\frac{\eta p}{GC}$ [42] | $\frac{\eta p}{c \omega \varepsilon \varepsilon_o A}$ [43] | $\frac{\eta p}{c d \omega C_A}$ [44] |

The chopping frequency can have a significant effect on the magnitude of the voltage response of the detector. Figure 15 shows the dependence of the voltage response on the chopping frequency ($f = \omega/2\pi$) for $\tau_E > \tau_T$. For the case shown the left-hand and right-hand slopes refer to the electrical and thermal roll-offs, respectively, for the case shown. This

curve depends on the properties of the different materials and the choice of $\tau_E$ as illustrated in Table 1.

### 3.2. Noise

In determining the detector performance it is insufficient to consider only its responsivity. The minimum detectable signal is limited by various noise sources in the detector element and in the load and measuring circuit.[55] The sensitivity of a detector element is often expressed as the noise equivalent power (NEP), which is the signal power incident on the bolometer that produces a signal-to-noise ratio of unity per 1 Hz electronic band width,

$$NEP = \frac{\Delta V_N}{R_V} \quad [45]$$

The detectivity is defined as the inverse of the NEP,

$$D = \frac{1}{NEP} \quad [46]$$

and the specific detectivity is $D^* = A^{1/2} D$. The use of $D^*$ in the discussion of the performance of pyroelectric detectors can be misleading because some of the noise sources depend on the area (A) of the detector. $D^*$ is useful for comparing devices of different areas.[56]

The primary electronic noise sources for the circuit in Figure 14 are the temperature or radiation noise, Johnson noise of the equivalent circuit, and the amplifier current and voltage noise. The sum of the squares of these noise terms is the total noise power squared,

$$\Delta V_N^2 = \Delta V_T^2 + \Delta V_J^2 + \Delta V_i^2 + \Delta V_A^2 \quad [47]$$

Each term in Equation 47 depends on frequency and refers to unit bandwidth.

Thermal noise is the change in output voltage that arises from random changes in the temperature of the pyroelectric detector. These thermal fluctuations are produced by the random exchange of heat and photons between the detector and its surroundings. For a detector linked to its surroundings by wire leads and situated in an evacuated chamber, the thermal noise arises from the thermal radiation, $G_r$, impinging on the detector and the thermal conductance, $G_w$, of the wire leads. The thermal noise voltage is

$$\Delta V_T = \frac{R_V}{\eta}\left(4kT^2G\right)^{1/2} \qquad [48]$$

where $G = G_r + G_w$. To minimize the thermal noise it is necessary to minimize the thermal conductance and the operation temperature. The smallest value of the thermal noise for a given temperature is obtained when the radiative conductance dominates the thermal conductance.[57] The ultimate detector sensitivity is limited by background radiation fluctuations. The thermal noise of a radiation limited detector depends on the temperature as $T^{5/2}$.

Johnson noise arises from the random motion of charge carriers in the crystal and in the electrical circuit. In practice, the pyroelectric crystal is not a perfect capacitor; the dielectric loss of the crystal is one factor contributing to the detector Johnson noise.[58] The Johnson noise voltage per unit bandwidth[59] is given by

$$\Delta V_J = \left(\frac{4kT}{R}\right)^{1/2}\left(\frac{1}{R^2} + \omega^2C^2\right)^{-1/2} \qquad [49]$$

The total resistance, R, is the parallel value of the gate resistance, $R_G$, and loss equivalent resistance, $R_E = (\omega C_E \tan\delta)^{-1}$. Likewise, C is the total capacitance of the detector, $C_E$, and circuit, $C_A$, in parallel.[60] At low frequencies, $\omega \ll (R_G C_E \tan\delta)^{-1}$, Equation 49 simplifies to

$$\Delta V_J = \left(\frac{4kTR_G}{1 + \frac{1}{\tan^2\delta}}\right)^{1/2} \qquad C_E \gg C_A. \qquad [50]$$

In the preceding equation the Johnson noise is minimized by low temperature operation, and small $R_G$ and dielectric loss, $\tan\delta$. The high frequency approximation, $\omega \gg (R_G C_E \tan\delta)^{-1}$, simplifies the Johnson noise voltage to

$$\Delta V_J = \left(4kT\frac{\tan\delta}{\omega C_E}\right)^{1/2} \qquad C_E \gg C_A \qquad [51]$$

Minimizing the Johnson noise in high-frequency operation is accomplished by operating at low temperature and high frequency with a large detector capacitance.

Other noise sources may reside in the electrical equipment, such as in the first stage of the signal amplifier, and microphonic effects.[61] The signal amplifier noise depends on the gate leakage current of the FET and the Johnson noise of the channel resistance. The preamplifier voltage noise is typically only a factor at high frequencies and below ~ 0.5 Hz where the 1/f noise begins to dominate. It is represented as a current generator in series or voltage source in parallel with the input circuit.[62] Microphonic noise is caused by vibrations of the electrical components. Vibration in the wire leads may result in charge fluctuations ($\partial Q = V\partial C + C\partial V$) and/or capacitance changes. In addition, since pyroelectric materials are also piezoelectric, vibrations can create stresses causing fluctuations in the spontaneous polarization. These changes in the electrical behavior can add to the noise.[63]

At the low frequencies intended for the pyroelectric detector operation, the thermal or Johnson noise will dominate. Assuming that the detector element's capacitance is greater than that of the signal amplifier and operation is in the high frequency roll-off regime, an expression for the detectivity can be derived using Equations 43, 45, 46 and 51:

$$D = \frac{\eta p}{c}\left(\frac{1}{\omega kTdA\varepsilon\varepsilon_o\tan\delta}\right)^{1/2} \qquad [52]$$

An expression for a materials figure of merit, $F_D$, can be derived from the Johnson noise limited detectivity:

$$F_D = \frac{p}{c}\left(\frac{1}{\varepsilon\varepsilon_o \tan\delta}\right)^{1/2} \qquad [53]$$

If the detector response is thermal noise limited an expression for the detectivity can be obtained from Equations 33, 45, 46 and 48, assuming the thermal radiance dominates the thermal conductance:

$$D = \left(\frac{\eta}{16Ak\sigma T^5}\right)^{1/2} \qquad [54]$$

The thermal noise limited detectivity is independent of materials parameters. Taking the emissivity as unity, the room temperature (300 K) thermal noise limited specific detectivity is $1.8 \times 10^{10}$ cm $Hz^{1/2}$ $W^{-1}$, compared with $3.7 \times 10^{11}$ cm $Hz^{1/2}$ $W^{-1}$ at 90 K. Operating the detector at the passive cooling limit (90 K) increases the performance of the detector by over an order of magnitude. Lowering the detector operating temperature affects the specific detectivity to a lesser extent in the Johnson noise limited case; $T^{-.5}$ vs. $T^{-1.5}$.

### 3.3. Materials Selection

Ferroelectric materials are desired over purely pyroelectric materials for pyroelectric detectors because of the large pyroelectric coefficients that occur at ferroelectric phase transitions. KDP (potassium dihydrogen phosphate) has a ferroelectric-paraelectric phase transition at 120 K. Unfortunately, it is a very difficult material to work with because it is hygroscopic. Solid solutions between several perovskite ferroelectrics also have transitions near 90 K: $Pb_{.06}Sr_{.94}TiO_3$, $Ba_{.1}Sr_{.9}TiO_3$, and $KTa_{.91}Nb_{.09}O_3$.[64] Pyroelectric detectors fabricated from $KTa_{.67}Nb_{.33}O_3$ single crystal materials operating at 235 - 270 K lead to $D^* = 1$ - $2 \times 10^8$ cm $Hz^{1/2}$ $W^{-1}$.[65] Detectors fabricated from $PbTiO_3$ ($T_c = 763$ K) resulted in $D^* = 9 \times$

$10^8$ cm $Hz^{1/2}$ $W^{-1}$ for operation near room temperature.[66] Values for the Johnson noise limited figure of merit, $F_D$ (Equation 53), can also be compared for room temperature based pyroelectric detectors. Values of $F_D$ for room temperature operation of $KTa_{.67}Nb_{.33}O_3$ ranged from .46 - 5 and for $Ba_{.67}Sr_{.33}TiO_3$ ($T_c \sim 293$ K), .034 - .84 $(cm^3/J)^{1/2}$.[67] Not enough data exist for determination and comparison of $F_D$ for the low transition temperature compositions; based on the above information, KTN is a good choice.

The phase transitions in potassium tantalate niobate, $KTa_{1-x}Nb_xO_3$, can be tailored to occur anywhere between ~ 4 K and 708 K, resulting in large dielectric, pyroelectric, piezoelectric, and electro-optic effects near the transition temperature. The paraelectric-to-ferroelectric transition temperature varies linearly with Nb fraction, x, for $x \geq 0.047$ and is well described by the empirical equation,

$$T_c = 676\,x + 32 \quad (K). \qquad [55]$$

A transition temperature $T_c = 93$ K requires $KTa_{.91}Nb_{.09}O_3$.

KTN is an ionic insulator that exists in the perovskite structure and is composed of stable $K^{1+}$, $Ta^{5+}$, $Nb^{5+}$ and $O^{2-}$ ions. Niobium is also stable as $Nb^{3+}$ which could lead to one oxygen vacancy per $Nb^{3+}$ substitution. Schottky defects may also contribute to vacancies in the form of two K vacancies and one oxygen vacancy, or multiple cation and oxygen vacancies. It is most likely that ionic conduction of KTN occurs by the migration of the lower valence potassium and oxygen ions. Ionic conduction, therefore, would be enhanced by the presence of K and O vacancies.

Although no previous reports in the literature have given credence to the presence of a KTN pyrochlore phase, it is probable that one exists. In order to maintain charge neutrality, the KTN pyrochlore would exist as a defect pyrochlore $A_2B_2O_6$ where the B site is shared by the Ta and Nb ions as in the perovskite structure. Oxygen vacancies naturally exist in the defect pyrochlore structure and could help lead to enhanced conduction over the perovskite

KTN phase. Non-stoichiometry and Schottky defects can also occur leading higher vacancy concentrations.

In addition to the changes that may be introduced by the presence of vacancies, the paraelectric and ferroelectric properties in solid solutions between insulating perovskites such as KTN can be greatly altered by small structural changes caused by defect-induced distortions.[68] That is, ordered micro-regions exist in the material that can become polar up to several hundred degrees above the ferroelectric phase transition temperature, leading to diffuse phase transitions and strong frequency dispersion in the dielectric permittivity.[69] As discussed in Section 2.1, the presence of a dispersed phase can lower the dielectric permittivity. In addition, the diffuse phase transition leads to ferroelectricity and piezoelectricity at temperatures above the 'averaged' phase transition.

### 3.4. Thin Film Approach

The desire to develop thin film vs. bulk crystalline pyroelectric detectors has two reasons. Based on the results of work performed developing bulk crystalline detectors, we know that we can increase the response, and thus detectivity, by developing thin film pyroelectric detectors. Also, a thin film approach will allow the use of microfabrication techniques that will enable easier fabrication of arrays and integration with readout electronics.

Initially, KTN devices were fabricated from bulk grown crystals with $T_c$ ~ 85 K. The KTN material was obtained from Dr. Daniel Rytz of the Optoelectronics Division, Sandoz Corporation, Saint Louis, France. Devices processed from this material were characterized for their optical response, dielectric and ferroelectric properties. The relative dielectric permittivity of these devices ranged from $10^3$ - $10^5$ in the temperature region of the maximum detector response; values of dielectric loss ranged from 0.1 - 1.[70] Using these values we can

estimate the frequency range for the electrical time constant. In addition, we can estimate values for the thermal time constant and determine from Table 1 the frequency range of operation.

Pyroelectric devices 1 $mm^2$ x 60 μm were fabricated from the bulk KTN. The capacitances of these devices over the temperature range of pyroelectric operation ranged from 148 pF - 14.8 nF and the preamplifier capacitance is on the order of 10 pF. Figure 14 shows that the capacitance of the pyroelectric device and preamplifier are in parallel; therefore, the voltage response of the pyroelectric detector is dominated by the capacitance of the pyroelectric device. In order to keep the flat top frequency response as wide as possible, the gate resistance was kept larger than that of the pyroelectric device, making the response device resistance dominant. Based on the dielectric loss and the chopping frequency ($\tau_E = RC = 1/\omega \tan\delta$) of 20 Hz, the electrical time constant is estimated to be between $8 \times 10^{-2}$ and $8 \times 10^{-3}$ seconds. These values correspond to electrical roll-off frequencies between 2 and 20 Hz.

The thermal time constant of these devices can be calculated from Equations 31, 32 and 33. By choice of wire dimensions and material, the detector thermal link was constructed to operate in the radiation limited regime. For an estimated specific heat of 2 J/$cm^3$K and a quantum efficiency of 0.2, and operating temperature of 90 K, the thermal time constant is $4.3 \times 10^3$ seconds. This corresponds to a thermal roll-off frequency of $4 \times 10^{-5}$ Hz. The voltage response of our pyroelectric devices can be described by Equation 43 of Table 1 since $\tau_T > \tau_E$ and $C_E > C_A$.

As discussed in Section 3.2, the detector performance is typically limited by either thermal or Johnson noise. In the thermal noise limited case the detectivity dictates that the performance can be increased for smaller device areas (see Equation 54). For a bulk crystalline sample a reduction in area is perhaps possible down to $1 \times 10^{-8}$ $m^2$, as opposed to a thin film

material where microfabrication can be used to define $1.96 \times 10^{-9}$ $m^2$ devices. This represents approximately a factor of 2 increase in detectivity.

The performance of a Johnson noise limited detector will increase for both reductions in area and thickness of the device (see Equation 52). A shift in the electrical or thermal time constant for operation in the flat top frequency response regime will also increase the performance. Since the electrical time constant, $\tau_E = \varepsilon\varepsilon_o\rho$, is independent of the geometry of the device, changing the dielectric loss, $D = (\omega\varepsilon\varepsilon_o\rho)^{-1}$, is the only way to shift the electrical time constant. Decreases in the electrical time constant shift the voltage response curve to higher frequencies. Unfortunately, this requires an increase in dielectric loss and thus lowers the performance. The thermal time constant can be lowered in order to shift its roll-off frequency to higher values by decreasing the thickness of the detector (see Equation 31). In order to move the frequency of the thermal roll-off to 20 Hz it is necessary to produce a sample on the order of 1 Å thick, which is unfeasible. However reducing the area or thickness of the device increases the detectivity. Bulk crystalline samples 60 μm thick were achieved with bulk KTN compared to 0.25 μm thick thin films. This results in over an order of magnitude increase in detectivity. Combined with the reductions in area this will possibly lead to 20 x increase in detectivity.

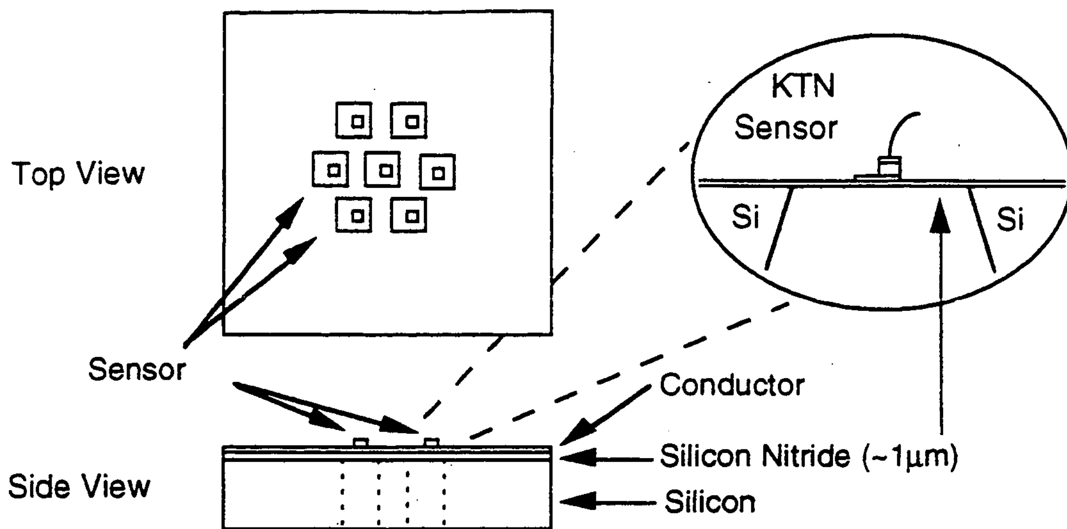


Figure 16. Schematic of thin film pyroelectric detector array.

The increases in detectivity and the future need for detector arrays makes the thin film approach to detector fabrication advantageous. Figure 16 shows a schematic of how we have proceeded with the thin film development. A silicon wafer is used as a substrate because of its mechanical properties and compatibility with microfabrication processes. On the silicon wafer we deposited a silicon nitride membrane 0.25 - 1 μm thick. A conducting layer is then deposited on the silicon nitride layer followed by the KTN thin film deposition and another conducting layer. Once the material growth on these substrates is developed the detectors will be patterned on the front side of the wafer. Portions of the backside of the wafer will then be etched leaving silicon nitride membranes on which the pyroelectric devices lie. The area and thickness of the membranes can be adjusted to optimize the thermal conductance between the detectors and the silicon heat sink while still providing mechanical stability for the devices.

Table 2. Global issues in substrate selection.[71]

| Issue: / Effect | Chem. compatibility | Thermal expansion | Surface quality | Substrate cleanliness | Substrate homogeneity | Substrate stability | Buffer layer |
|---|---|---|---|---|---|---|---|
| Process temperature | √ | √ | | | | √ | √ |
| Interface reaction | √ | | | √ | | | √ |
| Film impurity | √ | | | √ | | | √ |
| Substrate impurity | √ | | | | | | √ |
| Film adhesion | √ | √ | | | √ | | √ |
| Film buckling/ cracking | | √ | | | | | √ |
| Film microstructure | | | √ | √ | √ | √ | √ |
| Film composition | √ | | | | | | √ |
| Film morphology | | | √ | √ | √ | √ | √ |
| Film uniformity | | | √ | √ | √ | √ | √ |
| Electrical properties | √ | √ | √ | √ | √ | √ | √ |

Almost all aspects of film growth are strongly influenced by the substrate. Table 2 summarizes the effect of substrate characteristics on the film and substrate after thin film growth. Buffer layers are films positioned between the substrate and the film in order to alleviate shortcomings of the substrate. The metal electrode in the KTN/metal/SiN/Si layer acts as a buffer layer. In addition to providing adhesion between the metal and KTN, the layer must address the remaining issues. Typically, in ferroelectric materials this can be achieved by using a metallic oxide of the perovskite structure grown *in situ* with the film. One issue that presents a challenge is thermal expansion. Typically, the thermal expansion of a heterostructure system is governed by that of the substrate, in this case, Si. This results in a

limitation in the thickness of the film before cracks begin to form. Up to this critical thickness the film conforms to the thermal expansion properties of the substrate and may alter the film's properties.

## 4. Review of Thin Film Growth

### 4.1. Pulsed Laser Deposition

Pulsed laser deposition (PLD) is a technique for rapid investigation of complex structured materials; an example is the successful growth of the high temperature superconductor $YBa_2Cu_3O_{7-\delta}$ (YBCO). PLD is a simple technique to use but it involves very complex interactions that are not fully understood.

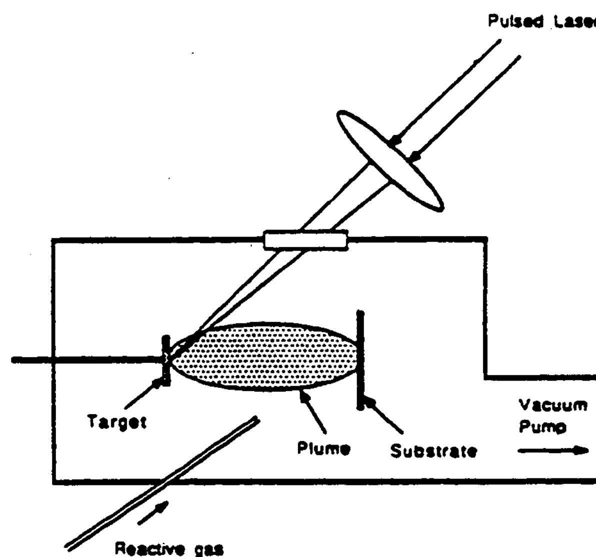


Figure 17. Schematic diagram of a PLD apparatus.[72]

A schematic of the PLD apparatus is shown in Figure 17. A pulsed laser beam is focused through a vacuum chamber window onto the target of the material to be deposited. The 20 - 30 ns laser pulse is focused to an energy density of ~ 1 - 10 J/cm$^2$ which vaporizes a few hundred angstroms of the target. The vaporized plume is oriented perpendicular to the

target surface in the form of neutral or ionized atoms and molecules. The kinetic energy of the atoms and molecules is in the 1 - 10 electron volt range. The plume material is deposited on a substrate positioned directly across from the target. Deposition rates are ~ 1 Å/pulse. The kinetic energy of the deposited material and the elevated substrate temperature aid crystalline growth. Deposition of material can take place in background gas pressures of several hundred mTorr.[73]

The mechanisms behind the laser target interaction are not fully understood but a simple picture is as follows. Photons from the incident laser beam are absorbed by the target causing surface heating. The optical penetration depth and thermal diffusivity of the target along with the energy transfer rate (laser pulse width) determine the increase in surface temperature. At the power densities used for PLD, the electric fields generated by the laser result in dielectric breakdown and surface melting of the target. Above a material-specific threshold energy, removal of the material from the molten layer does not take place by thermal evaporation but is linearly dependent on the laser fluence. It is believed that the congruent evaporation of multicomponent targets and the rapid rate of material removal characteristic of PLD are critically dependent on the coupling of the optical energy of the laser to the target. This coupling is optimized with short wavelengths (UV) and short pulse widths (~ 30 ns). The energy absorbed by the material occurs in such a short time that the target, instead of conducting the generated heat away, expels the hot material from the surface in a shock-wave like manner making the rate of material removal independent of the elemental species of the target. Material removal from the target causes the emission of many species including ions, electrons, neutral atoms and molecules. A recoil pressure formed during the emission process is exerted on the liquid layer expelling molten material. Thus, the material removed is a combination of liquid and vapor.[74]

The pulsed laser deposition parameters that affect the deposition are laser energy density at the target, laser wavelength, laser pulse duration, target material, target surface

condition, background gas and pressure, substrate-to-target distance, substrate temperature, and substrate. The laser energy density at the target is affected by the laser emission wavelength, laser operation energy, and laser beam focusing. If the laser energy is to low the absorption of the laser energy produces near-equilibrium thermal evaporation. This is not desirable for materials that do not evaporate congruently. The threshold energy for congruent evaporation of YBCO is ~0.11 $J/cm^2$. The useful laser wavelengths for PLD lie between 200 and 400 nm because of the strong absorption by most materials in this spectral region.[75]

Target quality is an important issue in the growth of PLD thin films. Chemical non - stoichiometry and particulates ("boulders") form defects which can affect the electrical properties of the film. The film stoichiometry is primarily determined by the target stoichiometry. In addition, the formation of particulates or boulders is primarily influenced by the target's surface features, and to a lesser extent the target density and homogeneity. A rough surface produces reduced deposition rates and particulate exfoliation by evaporating the anchor early and ejecting a particulate. Exfoliation gives off randomly shaped solid particulates and is not only dependent on the target surface morphology but also laser energy density. Laser energy density beyond a threshold fluence leads to increased particulate size and density.[76] Needle-like cones that are formed after continuous ablation melt or break off as a result of the thermal shock produced by the intense laser irradiation. A denser and/or lower porosity material enables one to create a smoother target surface, thus, decreasing the particulate formation. Inhomogeneous materials will have variable melting temperatures which can also lead to surface variations and particulate ejection much the same way as porosity.[77]

Other origins of particulates are subsurface boiling and liquid layer expulsion. Subsurface boiling occurs when the time required to transfer the laser energy into the target is shorter than that needed to evaporate the surface layer or when the subsurface is superheated before the surface reached vapor phase. This is an effect associated with materials of high thermal conductivity and therefore is not likely to occur in dielectric materials. Liquid layer

expulsion occurs when the recoil pressure exerted by the shock wave of the laser plume is strong enough to splash micron-sized condensed globules from the liquid surface layer of the target.[78]

Target texturing, a common effect, is the roughening of the surface with ablation time. This leads to a drop in deposition rates, increased particulate formation, and a slanting of the plume toward the laser beam with time. To combat these effects, the targets can be sanded between growths, and rotated during growth so that the laser beam doesn't always hit the same position on the target.

Typically reactive gases such as oxygen are used to assist the deposition of oxides. It has been found that the presence of oxygen during growth of oxide materials not only helps maintain oxygen stoichiometry but can oxidize ejected atoms and molecules as they travel to the substrate. The oxidation process favors large substrate-to-target distances, high kinetic energies and high oxygen pressures.[79]

## 4.2. Silicon Integration

Integration of ferroelectric materials with silicon substrates is a widely studied topic. Many applications involving ferroelectric materials require high temperature growths on a conducting substrate in an oxygen ambient. This limits the metallic layer to either a conducting oxide material or inert metals such as Pt. Although few studies have been made on metal/SiN/Si heterostructures, many have been performed on metal/$SiO_2$/Si heterostructures. Studies on the adhesion of Pt to $SiO_2$/Si substrates indicate that Pt does not bond well to $SiO_2$. To remedy this problem studies have focused on an adding other metal layers such as Ti to promote adhesion. The Pt/Ti bilayers have been met with limited success. At higher temperatures the Pt/Ti bilayers degrade, resulting in an unstable surface which affects the

morphology, phase and orientation of the ferroelectric layer. It is believed that the Ti and O both diffuse through the Pt layer forming $TiO_2$ at the surface of the Pt and the Pt/Ti interface. In addition, grain coarsening of the Pt film leads to a rougher growth surface.

Sreenivas et al.[80] solved this in the case of $SiO_2$/Si substrates. By depositing a very thin layer of Ti followed by a crystallized layer of $TiO_2$ and then the Pt film, they created a stable system that withstood 700°C anneals for 12 hours in air (1 atmosphere). The thin layer of Ti was intended to promote adhesion to the $SiO_2$ by oxidation. The $TiO_2$ layer was intended to form an adhering layer between the Pt and the $TiO_2$ formed by the oxidation of the Ti. Cooney et al. used a similar approach to stabilize Pt films on SiN/Si substrates. However, a few differences did exist. First of all, their layers were thicker and their sputter deposited $TiO_2$ was amorphous. However, they were able to show stability at temperatures as high as 700°C.[81]

In approaching this problem, one may be tempted to deposit TiN to promote adhesion between Pt and SiN. However there are several issues that should be addressed. SiN is naturally terminated with a layer of $SiO_2$ therefore the $TiO_2$ is probably just as effective if not more so. Also, oxides are thermodynamically more stable than nitrides;[82] this makes it reasonable to expect that the TiN will oxidize.

### 4.3. Potassium Tantalate Niobate

Few papers have been published on the development of KTN thin films. All the published papers have looked at KTN materials with transitions near room temperature. Several different thin film techniques have been applied to the growth of KTN. Common problems to all techniques is potassium deficiency and broad phase transitions as measured by the dielectric permittivity versus temperature. Potassium deficiency has been shown to depress

the dielectric permittivity, but the extent to which it may effect the broadness of the phase transition has not been studied. The paraelectric and ferroelectric properties in insulating perovskites including KTN can be greatly altered by small structural changes introduced by stress due to externally applied stress[83] and film surface tension.[84] In piezoelectric materials this can lead to a loss of ferroelectricity.[85]

Electrical measurements of KTN thin films are sparse, probably due to the difficulty in maintaining potassium stoichiometry. Most measurements have focused on the dielectric properties of the films which show low and broad peaks in the dielectric permittivity peaks, compared with single crystal KTN. Metalorganic deposition of $KTa_{0.6}Nb_{0.4}O_3$ films on Pt - coated polycrystalline Yttria yields broad $\varepsilon(T)$ peaks with a maximum ~ 5000.[86] Post-growth K vapor anneal at 1070°C lead to a broad but high relative dielectric permittivity, 16000@10 kHz, at the Curie peak of metalorganic films.[87] The spontaneous polarization before annealing is 24 $\mu C/cm^2$. Nazeri reported values for sol-gel grown KTN films with subsequent RTA (rapid thermal annealing) that resulted in < 0.1 μm thick films. The spontaneous polarization and dielectric permittivity of these samples were on the order of 8 - 30 $\mu C/cm^2$ and 5000, respectively. [88] The upper range of $30 \mu C/cm^2$ compares favorably with values published for bulk single and polycrystalline KTN.[89,90,91]

RF-magnetron sputter deposition on sapphire substrates using a 15% K enriched $KTa_{0.5}Nb_{0.5}O_3$ target pressed to 90% of its theoretical density prepared by standard ceramic processing yielded $K_{0.94}Ta_{0.68}Nb_{0.4}O_3$, a 6% K deficiency. Films grown using this same target on a $Pt/SiO_2/Si$ substrate showed a maximum in $\varepsilon(T) = 2090$ measured at 1 kHz which is significantly lower than that for bulk single crystals ($\varepsilon \geq 20000$). The peak is also somewhat broader than those observed in bulk single crystal KTN. A K deficiency of only 1.2% atomic percent was achieved in a single phase perovskite film.[92]

KTN films grown by PLD are typically deficient in potassium. Several techniques have been applied to increase the potassium content of the films with varied amounts of success. PLD films were grown using a laser energy density of 0.7 $J/cm^2$ onto Si substrates in a vacuum at room temperature. The $KTa_{0.55}Nb_{0.45}O_3$ target used was prepared by sintering a pressed mixture of potassium carbonate ($K_2CO_3$), tantalum pentoxide ($Ta_2O_5$), and niobium pentoxide ($Nb_2O_5$) powders for 20 hours at 1000°C. RBS showed the Ta:Nb ratio was preserved, but only 45% of the potassium stoichiometry was preserved. Increasing the substrate temperature and adding oxygen during growth only improved the K content to 70 - 80% of the stoichiometric amount. In order to increase the concentration of K in the films the researchers used a segmented target approach. A semicircular melt-grown target of composition $KTa_{0.7}Nb_{0.3}O_3$ used in conjunction with a semicircular target of molten $KNO_3$ produced stoichiometric (110) KTN films on (110) STO substrates. They used a 1 $J/cm^2$ laser energy density, 50-100 mTorr oxygen partial pressures, 700-750 °C substrate temperatures, 6 cm target-substrate distance, and 0.2 nm/pulse deposition rate. TEM showed uniform films free of large defects at the interface with the STO with some dislocations. No reports were made regarding the presence of pyrochlore in the films (phase purity), whether the initial ceramic pressed target was stoichiometric as opposed to just the starting materials, or what temperature and pressure ranges were attempted in the non-segmented target approach. No electrical measurements were reported for this sample.[93]

A segmented target was also tried by Yilmaz et al.[94] with pulsed laser deposited films on $SrRuO_3$ electrodes yielding stoichiometric films. This approach, however, limits the laser energy density at the target because of different melting temperatures between the two target phases. Further research by this group showed that the density of the KTN part of the segmented target could be improved to 95% by using a sinterforging technique of $KTaO_3$ and

$KNbO_3$ powders.† Results of KTN films with a superior sol-gel derived segmented KTN target were reported for (110) KTN films grown on (110) STO substrates. Other substrate orientations could easily be grown by choosing different STO substrate cuts. Deposition was performed at 700-750°C, 7 kPa, 10 -20 Hz, with 1 J/cm$^2$ laser energy density on the target. The Ta/Nb ratio preserved with respect to the target and no potassium deficiency was observed. It was not specified whether the resulting films were 100% perovskite, only that they were well oriented. Growth of KTN films were also performed directly on several conducting films including: Pt, $ZnO_2$, $SnO_2$, $SrRuO_3$, $CdSnO_3$ and $In_2O_x$. $SrRuO_3$ proved to be a good conducting medium in which to seed the perovskite growth. Measurements of the dielectric permittivity yielded a broad maximum value of 10000 at .3 kHz as a function of temperature. This low value was attributed to composition inhomogeneities and strain resulting from the lattice mismatch.

Nazeri et al.[95] performed PLD of $KTa_{0.55}Nb_{0.45}O_3$ thin films on (100) MgO substrates using a pressed KTN target of fully reacted perovskite KTN powder which was synthesized by a sol-gel technique. Their research focused on studying the phase composition and microstructure as a function of oxygen pressure (50 and 300 mTorr) and temperature (300 - 700°C) using an excimer laser operating at 10 Hz and 1.5 J/cm$^2$ and a substrate to target distance of 4 cm. They characterized the films using XRD, SEM, TEM and RBS. For temperatures greater than 500°C they used RBS to look at the stoichiometry of the films. The Ta:Nb ratio for all films was higher than that of the target (1.22), but there were no clear trends as a function of temperature and pressure with ratios ranging from 1.35-1.73. Increased oxygen partial pressure during pulsed laser deposition yielded 84-92% K at 300 mTorr versus 81-82% K at 50 mTorr. None of their films were completely pyrochlore free and the following trends were observed. Films grown at ≤ 500°C were almost entirely amorphous with a few random grains of perovskite and pyrochlore. At 650°C and 300 mTorr the film is entirely

† Jupiter technologies, Ithaca, NJ.

crystalline and primarily perovskite. Further increases in temperature lead to higher proportions of pyrochlore. For 50 mTorr growths, similar trends were observed except that the highest ratio of perovskite to pyrochlore occurred at 700°C.[96] A similar approach has been applied with success to the incorporation of volatile Pb within $PbZrTiO_3$ films deposited by PLD. Pb loss has been found to depend on substrate temperature and oxygen pressure. Lower substrate temperatures and/or increased oxygen pressure leads to stoichiometric films.[97]

Pulsed laser deposition of $KNbO_3$ can be expected to exhibit similar/identical K deficiency problems as those posed by KTN. $KNbO_3$ films grown on MgO substrates using a single crystal $KNbO_3$ target by Zaldo et al.[98] were found to have a K deficiency linearly dependent on the substrate-target distance. At 2 cm the K/Nb ratio was ~ 0.8 while at 6 cm the K/Nb ratio was ~ 0.5. K- rich targets (K/Nb = 2.85) were used to achieve stoichiometric films at reasonable target-substrate distances. Thöny et al.[99] also used enriched targets to achieve stoichiometric $KNbO_3$ sputtered films, mixing $KNbO_3$ and $K_2CO_3$ powders resulted in a K/Nb ratio of 3.

# 5. Experiments and Results

## 5.1 Target Fabrication

KTN targets for the PLD films were made by standard ceramic processing at LBNL by John Jacobsen and James Wu of the ceramics group. A summary of the target batch process parameters and relevant target properties is shown in Table 3. Target batch #1 was produced by mixing $KO_2$, $Ta_2O_5$ and $Nb_2O_3$ oxide powders and reaction sintering at 900 °C for 16 hours in air in an $Al_2O_3$ crucible. The resulting ceramic was then reground and pressed into a 3/4" steel die at 10 kpsi. Next the target was isostatically pressed at 180 kpsi (cold isostatic press or CIP) and resintered in air at 1050 °C for 20 hours. The XRD pattern of this target, Figure 18, shows many diffraction peaks that correspond to any number of K, Ta and Nb oxides. The peaks are impossible to assign with any accuracy because of variability in phase content and stoichiometry. RBS results indicate that the target contains about half the intended K. The loss of potassium is assumed to occur during the high temperature sintering steps where its high vapor pressure and that of its oxides aides in its loss from the target. The potassium target is only ~ 67 % of it's theoretical density. XPS results of films grown using a target from batch #1 indicate that they range from 35 - 65 % K deficient.

Table 3. Results of important properties including the target phase, % K content of constituents compared with stoichiometric KTN, % density compared with single crystal KTN, and comments referring to the visual quality of the targets produced at LBNL are tabulated. (CIP - cold isostatic press, HIP - hot isostatic press)

| Target Batch | Process | Phase(s) | K content % | Density % | Comments |
|---|---|---|---|---|---|
| 1 | CIP | multi-phase | 47 | 70 | - |
| 2 | CIP | perovskite | 115 | 72 | - |
| 3 | CIP | - | - | - | crumbled |
| 4 | CIP | - | - | - | crumbled |
| 5 | HIP under Ar | multi-phase | | 76 | inhomogeneous |
| 6 | CIP | multi-phase | | 73 | inhomogeneous |
| 7 | CIP | perovskite | 99 | 71 | - |
| 8 | CIP | - | - | - | crumbled |

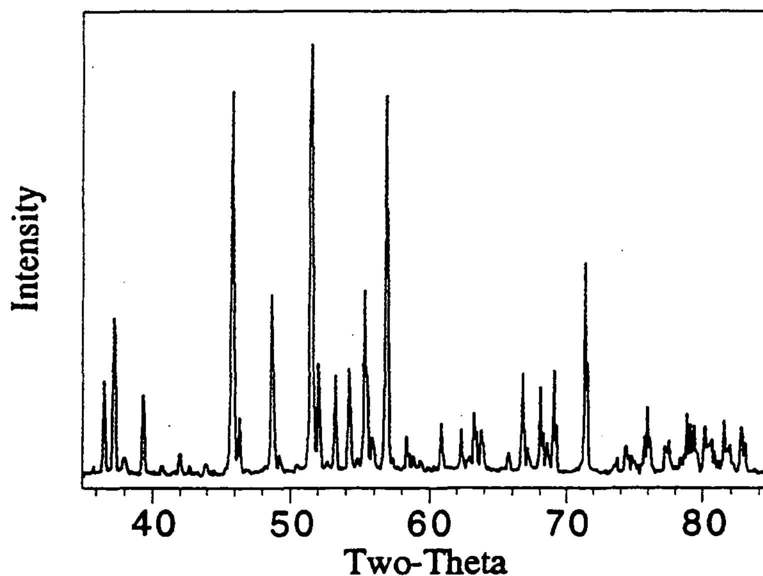


**Figure 18. XRD scan of a target from batch #1 indicates that it is polycrystalline and is composed of a mixture of oxide phases.**

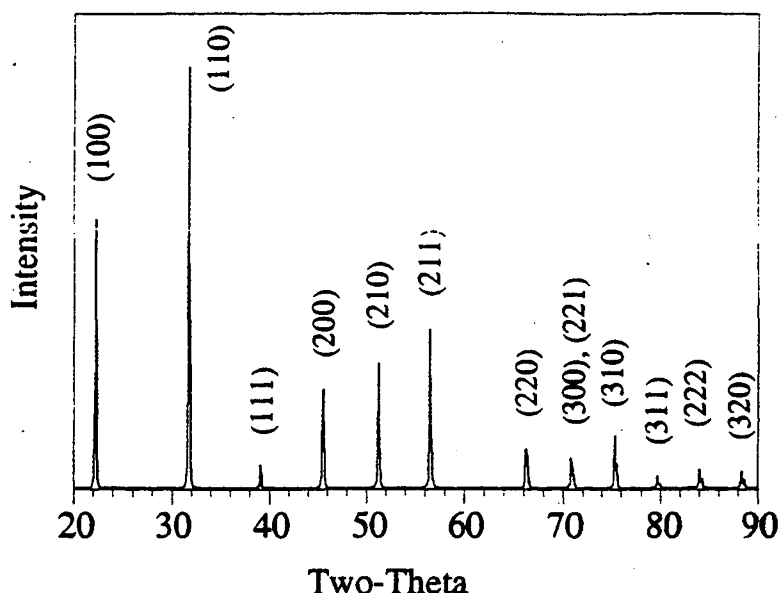

Figure 19. XRD scan of a target from batch #2 showing 100 % polycrystalline perovskite KTN.

To compensate for the loss of K during sintering starting materials with 2x, 3x and 4x, the K required for stoichiometric KTN were used to fabricate target batches #2, #3 and #4, respectively. Target batches #3 and #4 were not structurally sound. Examination of the targets revealed yellow pockets of material which we assume are unreacted $KO_2$, a sticky yellow powder. We attribute the poor structural quality of these targets to the inability of the target to accommodate the excess K that is not driven off by the sintering processes. Neither XRD, RBS, nor density measurements were made on these two targets due to their crumbled state. The doubled K content of batch #2 targets resulted in polycrystalline-single phase perovskite KTN, Figure 19. RBS and XPS indicate that they are slightly K enriched ~ 15%. In addition, the density was improved by a small margin to 72% of the theoretical value. Films grown from targets of batch #2 have K contents ranging from 80% to slightly K enriched. Particulates or boulders are seen by optical microscopy and SEM. Figure 20 is a SEM

micrograph showing boulders of two sizes 0.5 - 1 and 2 - 3 μm in diameter. The larger boulders have facets indicating they were liquid and crystallized at some point during their formation. Boulder formations of this type arise from liquid layer expulsion of the target which can be eliminated by using a molten target.

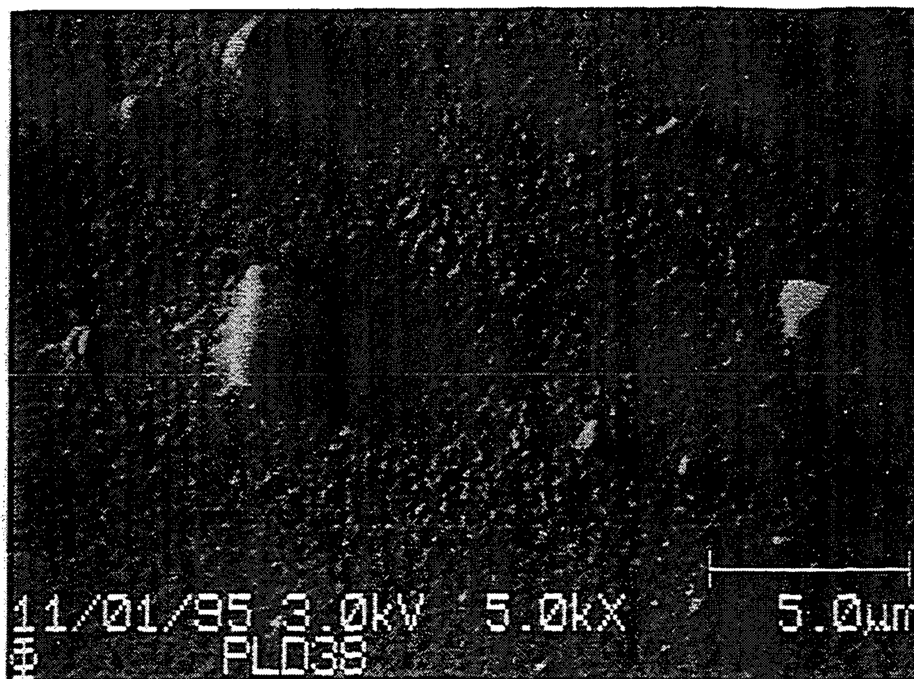


Figure 20. SEM micrograph of a KTN film grown on LSC/LAO at 675 °C. The larger faceted boulders are 2 - 3 μm in diameter and the smaller boulders are 0.5 - 1 μm in diameter. The surface texturing is on the order of 0.25 μm.

Improving the target density was attempted by application of the HIP (hot isostatic press) process. Target batch #5 was prepared identical to batch #2 except that the last sintering process was performed by a HIP at 24 kpsi and 1150 °C in argon. The resulting target was structurally sound but looked inhomogeneous (dark spots) and exhibited an XRD scan similar to that of batch #1, 18. As expected, improvement in the target density was seen reaching 76 % of theoretical density. The multiphase and inhomogeneous target is probably a result of a lack of oxygen during the HIP process. Unfortunately, at the HIP temperature and pressure used for KTN one is unable to use oxygen without reaction with the HIP equipment.

To try and increase the density of the targets while maintaining homogeneity we decided to return to the CIP (cold isostatic press) process. Target batch #6 used an additional ball milling and sintering step to try and decrease the particle size and increase the mixing of the sintered powder. After mixing the powders, as in batch #2, the composition was sintered at 920 °C for 24 hours in air in an $Al_2O_3$ crucible. The mixture was then ball-milled and resintered overnight at 1000°C. After ball-milling the mixture was pressed into a 3/4" steel die using ~ 12 lbs and CIP at 18 kpsi before being sintered for 20 hours at 1050 °C. Visual inspection of the targets showed light green spots throughout. The XRD scan from the resulting target showed a mixture of oxide phases similar to target batches #'s 1 and 5, Figure 18. The density of the target was 73 % of the theoretical density. It is thought that the mixture of phases and inhomogeneity could arise from possible K non-stoichiometry caused by the additional sintering step.

Unfortunately, increasing the K content in these samples was thwarted because of misplacement of the $KO_2$ source powder. Instead, $KCO_3$ was used and found to be much more reactive. It was necessary to cut back on the starting K stoichiometry to achieve solid targets. Target batches # 7 and 8 correspond to starting K of 1 x and 1.5 x stoichiometric concentrations, respectively. Targets from batch #8 crumbled. Visual inspection of target batch # 7 indicated a homogenous target. XRD measurements show that the target is 100 % perovskite KTN as in target batch # 2, Figure 19. RBS measurements of the target show that it is 99 % K, $K_{.99}Ta_{.91}Nb_{.09}O_3$. Unfortunately, the target density did not improve; it was measured at 71 % theoretical density. The changes in the starting K content for fabrication of the targets with source is probably due to differences in the melting temperature. $KO_2$ starts to decompose at 300-400 °C and melts at 707 °C. $KCO_3$, on the other hand, melts at 891 °C.[100] Typically materials with lower melting points have lower boiling points and, thus, vapor pressure. Therefore, it is reasonable to assume that $KO_2$ vaporizes considerably more than $KCO_3$ before reaction with the stable $Ta_2O_5$ and $Nb_2O_5$ powders can take place.

## 5.2 Thin Film Growth

### 5.2.1 Overview

Initially, pulsed laser deposition growth parameters were narrowed for KTN films through a series of growths on (100)-pseudocubic $LaAlO_3$ (LAO) substrates.[†] (See Appendix B for details regarding thin film deposition equipment.) Substrates cut from LAO crystals were used because LAO is a fairly inexpensive crystalline material with high temperature stability that should be a good template to seed KTN growth. LAO is a perovskite structured insulator, which means its chemistry and structure are similar to those of KTN. Its lattice mismatch with KTN is only 5.6 %. Table 4 compares the thermal expansion, lattice constant and lattice mismatch for films used in conjunction with KTN in this study. The phases and orientations of the KTN films were determined using x-ray diffraction in the $\Theta$-$2\Theta$ mode (see Appendix C for details regarding characterization techniques). X-ray rocking curves were determined for a number of the films to determine crystalline quality by measurement of the FWHM of the film peaks. Another measure of the film quality can be obtained by using a x-ray phi-scan which measures the in-plane orientation of the film and can be used to estimate the degree of epitaxy. Once this study was completed, growth on conducting substrates was undertaken in order to determine the optimum conditions for enhancement of the electrical properties of the KTN films, namely the pyroelectric coefficient and loss.

† The $LaAlO_3$ substrates were obtained from Litton Airtron, Charlotte, NC.

Table 4. Materials used in combination with KTN thin film deposition. Thermal expansion coefficient, lattice constants, and lattice mismatch with KTN are given for room temperature.

| Material | Thermal Expansion Coefficient ($10^{-6}$/K) | Lattice Constant (Å) | Lattice Mismatch (%) |
|---|---|---|---|
| $KTa_{.91}Nb_{.09}O_3$ | 8.3 | 3.99 | - |
| $SrRuO_3$ | | 3.93 | 1.4 |
| YBCO (a-b plane) | 12.9 | 3.86 | 3.4 |
| $La_{.5}Sr_{.5}CoO_3$ | | 3.80 | 4.7 |
| $SrTiO_3$ | 9.4 | 3.91 | 0.5 |
| $LaAlO_3$ | 10 | 3.78 | 5.6 |
| YSZ | | | |
| Pt | 8.9 | 3.93 | 1.5 |
| Ti | 8.4 | hexagonal | |
| silicon nitride | 3.1 | amorphous | |
| Si | 4.7 | 5.43 | - 26.5 |

Several different electrode schemes were used in the attempt to maximize the perovskite phase of the film and provide a stable electrode. Pt/SiN/Si † was tried because of Pt's *high* - temperature stability in highly oxidizing atmospheres such as that used during the growth of KTN films and the need for the SiN/Si substrate. The Pt was deposited by sputtering resulting in [111] oriented films. The amorphous SiN was deposited non-stoichiometrically to produce films in tension. Poor electrical properties of these films, combined with the inability to suppress the pyrochlore phase, led to the investigation of conducting oxide electrodes, and the addition of other metal layers to improve the Pt adhesion. The conducting oxide materials exist in the perovskite structure and can be easily deposited in a conducting state by pulsed laser deposition. Three different conducting oxides were investigated: $La_{.5}Sr_{.5}Co_3O_3$ (LSC), $Y_1Ba_2Cu_3O_{7-\delta}$ (YBCO) and $SrRuO_3$ (SRO).†† The targets used for these growths were single phase. RBS performed on the SRO target indicated a composition of $Sr_{1.2}Ru_{1.0}O_{3.8}$ with

† The non-stoichiometric silicon nitride (SiN) was grown on 1/2 mm thick Si wafers by Ernst Kreysa using the Tylan 18 CVD furnace in the Berkeley Microlab.

†† The LSC and SRO targets were purchased from Seattle Specialty Ceramics, Woodinville, WA. The YBCO target was borrowed from Amit Marathe.

about $Ba_{0.005}$. The KTN/conducting oxide films were grown both on LAO and Pt/SiN/Si substrates. KTN/YBCO was also grown on (100) STO and (100)YSZ. † In practice the Pt is not stable at the high growth temperatures needed for KTN. The growth on oxide materials such as LAO, STO, and YSZ was performed in order to separate effects that might be due to unstable Pt. KTN/SRO was also grown directly on SiN/Si. In addition to the resistance measurements described above for KTN/LAO growths, dielectric permittivity and ferroelectric hysteresis measurements were made on the KTN films. The resistance of the conducting layers was also investigated to ensure stability after subsequent KTN growth.

### 5.2.2 Study of Potassium Tantalate Niobate Growth on Platinum

Initially, a feasibility study of KTN thin film growth was performed using Pt/SiN/Si (1000 Å/0.5 μm/1 mm) substrates. Films were deposited at 300 mTorr $Po_2$ and 650, 700 and 750 °C. A potassium deficient target from batch #1 with composition $K_{.45}Ta_{.9}Nb_{.1}O_3$ was used, the remaining deposition conditions are similar to those shown in Table 6. The KTN deposition time was 30 minutes or ~ 9000 pulses at 5 Hz. The x-ray diffraction scans in Figure 21 show a strong temperature dependence for the KTN perovskite phase formation on Pt. The perovskite KTN grows best at 700°C and is absent at 600°C, but the pyrochlore phase is present at all three temperatures. Although the Pt is [111] oriented perovskite KTN prefers to grow in the [100] orientation despite it's close lattice match with Pt, 1.5 %. XPS measurements of the film's surface composition indicate that the films contain only 35 - 65 % of the requisite K, the K content of the target is 47 % of the stoichiometric [K].

† The YSZ and STO substrates were purchased from Deposition Technology, Pennsylvania.

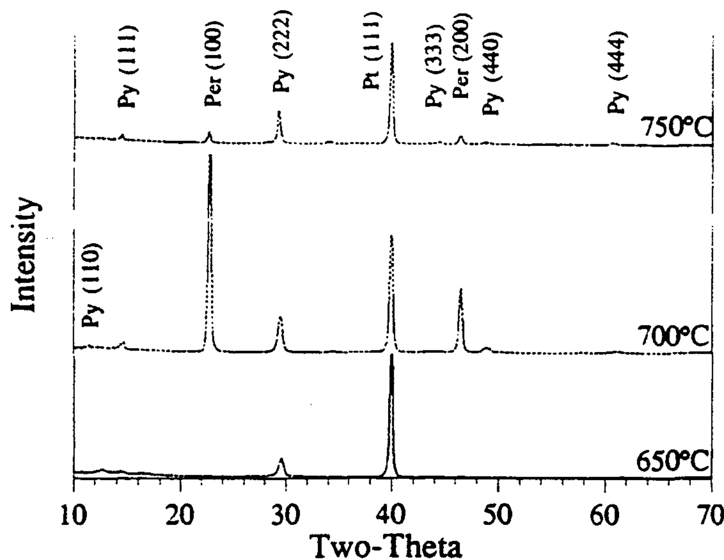


Figure 21. X-ray diffraction scans of KTN/ Pt/SiN/Si structures at 300 mTorr and 650 - 750°C. (py - pyrochlore, per - perovskite)

Bottom contact to the samples was achieved by etching back to the Pt layer using 5% HF. A profilometer measured the thickness of the KTN layers; 0.75, 1.63 and 1 μm for growths at 600, 700 and 750 °C, respectively. Top contacts were deposited by sputtering Pd:Au (200:1400 Å) through the circles of a shadow mask 0.145 - 0.229 $mm^2$ in area. Copper wires to these contacts were attached with silver epoxy. Measurements of the capacitance and resistance of the KTN devices as a function of temperature were made using a Capacitance Bridge (Appendix C) operating at 20 Hz and 25 mV pp A.C. (75 - 170 V/cm). The KTN film thickness and the area of the top contact was used to calculate the dielectric permittivity from Equation 4, Figure 22. The dielectric permittivity vs. temperature behavior is nearly the same for films grown at 600, 650 and 750 °C. It is 5 to 6 times less than what is expected (~ 390) for KTN of this composition at room temperature. In addition, instead of rising to a peak at the expected ferroelectric transition temperature, 90 K, the dielectric permittivity slowly decreases. The dielectric loss was calculated from Equation 7 and is plotted as a function of

temperature in Figure 23. The dielectric loss is fairly similar between samples and ranges from 0.02 - 0.04 at low temperatures and increases to values close to 0.1 at room temperature. The D.C. resistance of these devices is also quite high. A Keithly Model 617 electrometer measured room temperature resistivities $\rho \sim 10^{12}$ Ω-cm. Unfortunately, however, no ferroelectric hysteresis behavior was detectable in these films.

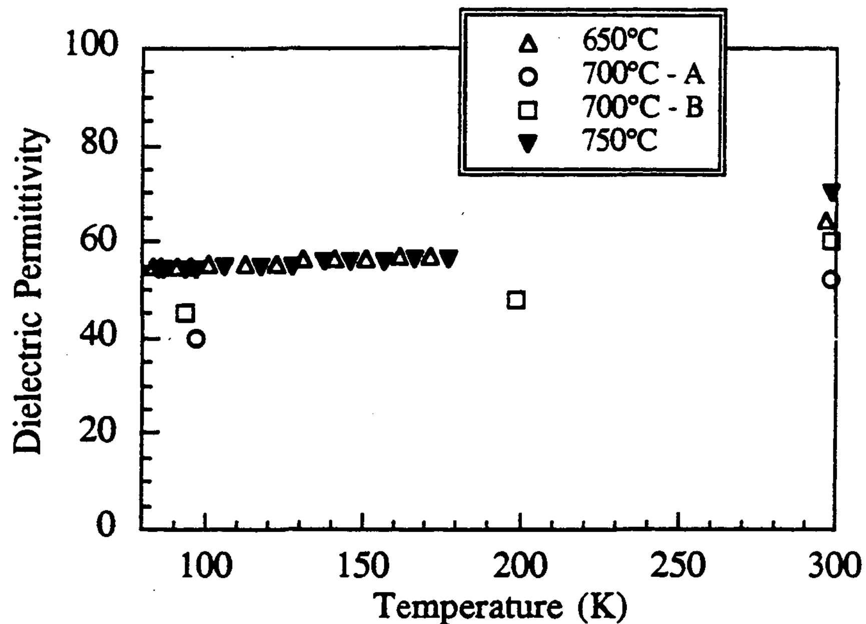


Figure 22. Dielectric permittivity vs. temperature for KTN films grown on Pt/SiN/Si substrates at 650, 700 and 750 °C. The areas of the devices were 0.145, 0.159, 0.229 and 0.145 mm$^2$ for growths at 650, 700 (A), 700 (B) and 750 °C.

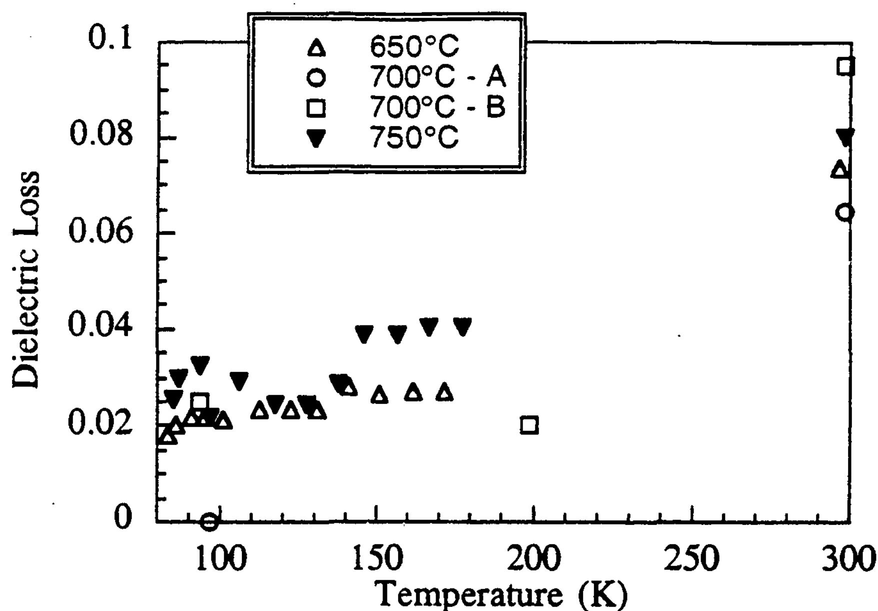


Figure 23. Dielectric loss vs. temperature for KTN films grown on Pt/SiN/Si substrates at 650, 700 and 750 °C. The area of the devices were 0.145, 0.159, 0.229 and 0.145 mm2 for growths at 650, 700 (A), 700 (B) and 750 °C.

Table 5. KTN deposition parameters for growth on Pt/SiN/Si using target batch #2, $K_{1.15}Ta_{.87}Nb_{.13}O_x$. (per - perovskite, py - pyrochlore)

| Film | Temp. (°C) | Pressure (mTorr $Po_2$) | Laser Energy (mJ) | Laser Shots | Phase |
|---|---|---|---|---|---|
| 1 | 650 | 400 | 600 | 4000 | py, sm. (110) per |
| 2 | 675 | 300 | 600 | 4000 | py |
| 3 | 700 | 100 | 700 | 5000 | py |
| 4 | 700 | 300 | 600 | 3000 | py, sm. (100) per |

Since the electrical properties of the films were very similar despite the quantity of perovskite KTN present, it was thought that the electrical properties of the film were not those of the perovskite KTN but perhaps those from a layer of pyrochlore acting as a series

capacitor. Given that hypothesis, attempts were made at growing pyrochlore-free KTN directly on Pt/SiN/Si using a higher K content target from batch #2 and similar deposition parameters as above. Table 5 summarizes the varied deposition parameters and shows that the growths performed were not successful in obtaining 100 % perovskite KTN.

### 5.2.3 KTN Growth on Lanthanum Aluminate Substrates

KTN films deposited on (100)-p LAO for a study of KTN pulsed laser deposition parameters were grown using a target from batch #2. These targets have a composition of $K_{1.15}Ta_{.91}Nb_{.09}O_3$ which corresponds to a transition temperature of 93 K. All deposition parameters, Table 6, were held constant except for temperature and partial oxygen pressure.† The temperature was varied between 600-750°C and the partial oxygen pressure was varied between 100 and 400 mTorr.

Table 6. KTN/LAO pulsed laser deposition growth parameters

| | |
|---|---|
| Laser Energy Density | 2-3 J/cm$^2$ |
| Laser Pulse Frequency | 5 Hz |
| Target batch #2 | $K_{1.15}Ta_{.91}Nb_{.09}O_3$ |
| Substrate-Target Distance | 6 cm |
| Cooling Conditions | 5°/min. ramp down at $P_{O2}$=500-600 Torr |

† The deposition time for films in this study varied from 15-30 minutes. This was determined not to affect the phase formation.

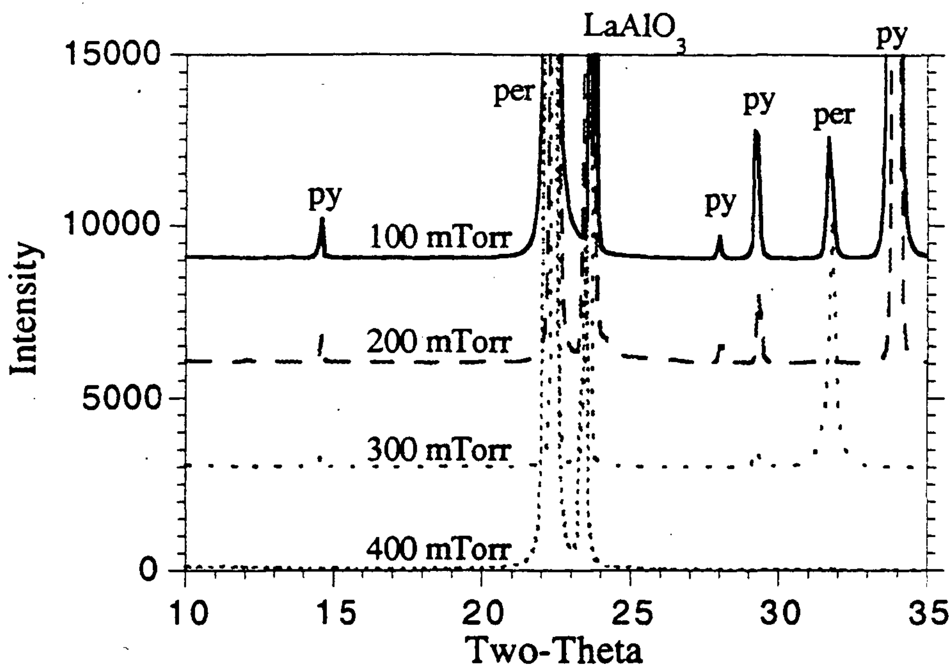


Figure 24. X-ray diffraction scans of KTN films grown on (100)-p LAO at 700°C and 100-400 mTorr.

Films grown at 100 and 200 mTorr partial oxygen pressure were primarily composed of what is believed to be the pyrochlore phase of KTN.[101] At partial oxygen pressures of 300 and 400 mTorr the films were composed of a significant amount of [100] oriented perovskite KTN, the pyrochlore phase is either not found or present in very small amounts. The XRD scan in Figure 24 shows the dramatic change in pyrochlore (400) intensity in 700°C grown films as a function of oxygen partial pressure with little corresponding change in the perovskite intensity. In addition, other pyrochlore reflections become increasingly smaller as the pressure is increased. For the lower pressure growths the pyrochlore phase is oriented with its {111}, {113} and {100}planes parallel to the substrate surface as shown by the (111) and (222) reflections at $2\Theta = 14.5$ and $29.3\,°$, the (113) reflection at $2\Theta = 28°$, and the (400) reflection

at $2\Theta = 34°$. Only small intensity {111} reflections are present for films grown at 300 mTorr $Po_2$. For 400 mTorr $Po_2$ all pyrochlore reflections are absent. Similar trends were found for growths at 600, 650 and 750 °C.

Table 7. (100) and (111) Rocking curve FWHM (degrees) of KTN films grown on LAO.

| Temperature (°C) | Oxygen Pressure $Po_2$ 300 mTorr (100) | Oxygen Pressure $Po_2$ 400 mTorr (100) | (111) |
|---|---|---|---|
| 600 | 0.64 | 1.59 | 1.11 |
| 650 | 0.73 (675°C) | 0.64 | 0.48 |
| 700 | 0.57 | 0.43 | 0.52 |
| 750 | 0.45 | 0.50 | 0.67 |

Further characterization was performed on films grown at 300 and 400 mTorr, films composed primarily of the perovskite phase. Rocking curves of the (100) perovskite KTN peak were recorded for all films grown at 300 and 400 mTorr; the results are summarized in Table 7. Figure 25 shows the FWHM of a film grown at 700 °C and 400 mTorr. The form of the rocking curve FWHM is similar for all films except for the film grown at 600 °C and 400 mTorr. These rocking curves are broader than what is observed by inspection of the $\Theta$-$2\Theta$ x-ray diffraction scans. This difference is attributed to the smallness of the sample which could broaden the FWHM during the rocking of omega. There is no clear trend that can be obtained from the rocking curve FWHM as a function of temperature, or film orientation with respect to the substrate. Omitting the anomalous sample, the film FWHM average is 0.57°, this 2.3 times greater than the (100) FWHM of single crystal KTN grown by the Czochralski method,

0.2406°, Figure 26.† The $(100)_{-p}$ FWHM of the LAO substrates was measured at 0.1488°, Figure 27. Figure 28 shows a perovskite KTN phi-scan of a film grown at 600°C and 400 mTorr. The phi-scan displays the fourfold symmetry of the {111} with respect to the (100) oriented film. The narrowness of the phi-scan peaks shows an exceptional degree of in-plane alignment and along with the [100] oriented films is a good indicator of epitaxial growth. Epitaxial growth was confirmed by the alignment of the KTN {111} with the $\{111\}_{-p}$ LAO phi - scan peaks.

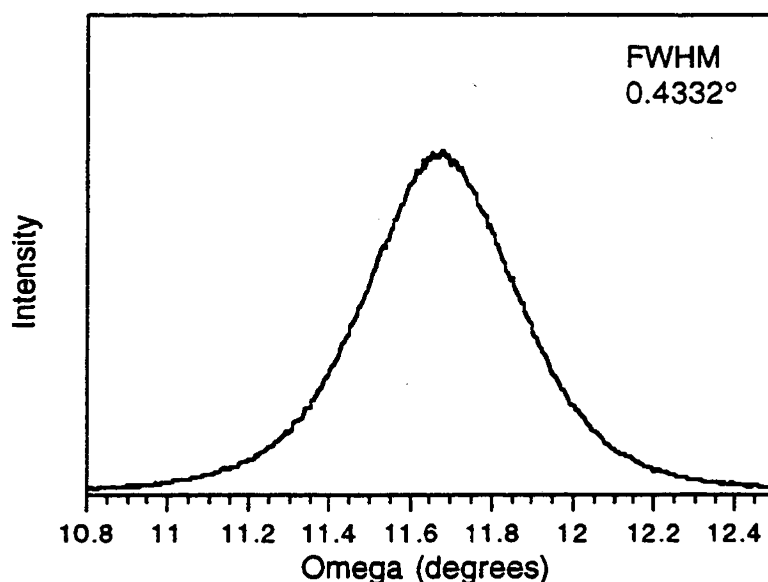


Figure 25. X-ray rocking curve of (100) KTN. The film was grown on (100)-p LAO at 600°C and 400 mTorr.

† These KTN crystals, PK-33, were grown by Dr. Daniel Rytz currently at the Ferschungsinstitut, Idar - Oberstein, Germany.

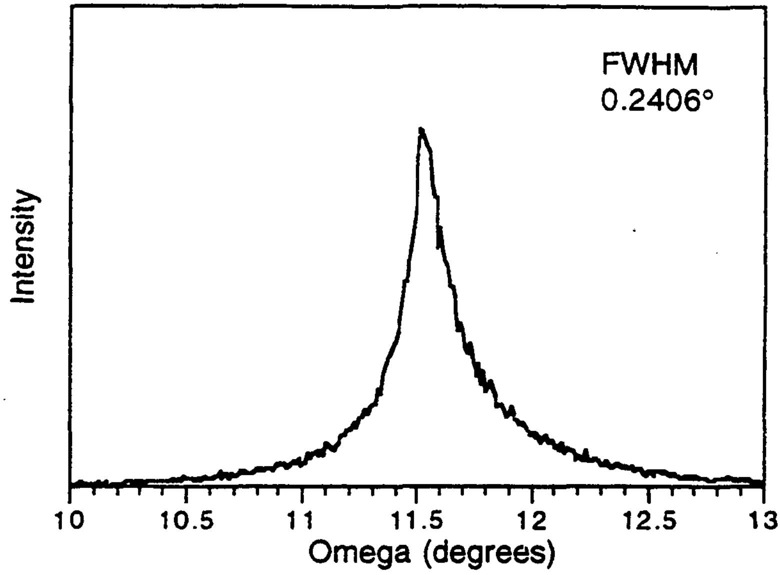


Figure 26. (100) x-ray rocking curve of single crystal KTN, PK-33, obtained from Dr. Daniel Rytz.

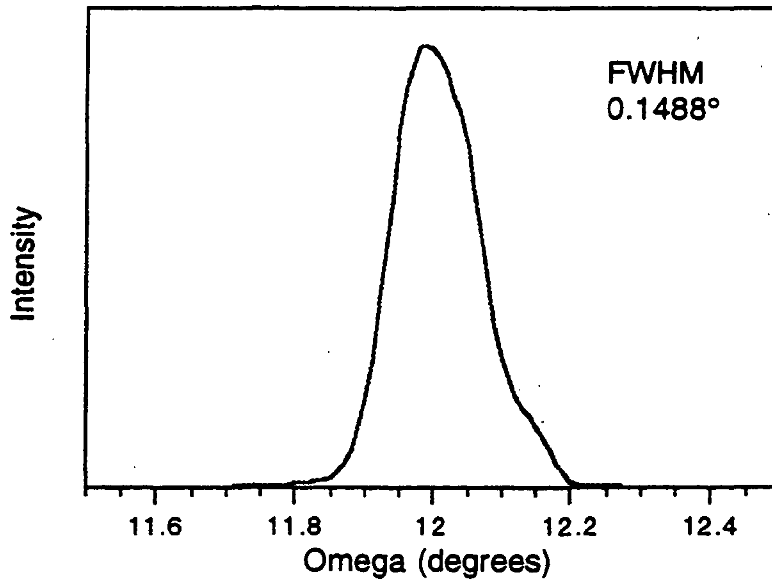


Figure 27. Rocking curve FWHM of (100)-p LAO.

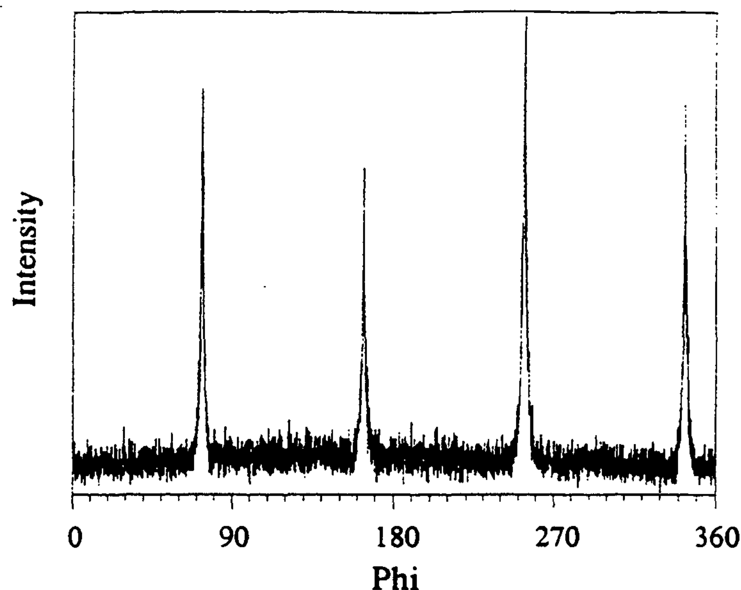


Figure 28. Phi-scan of a [100] perovskite KTN film grown on $(100)_{-p}$ LAO at 600°C and 400 mTorr showing four-fold symmetry of the {111}.

RBS measurements were made on the films grown at 300 and 400 mTorr to determine the film stoichiometry and thickness. Figure 29 is an example of the RBS raw data and fit for a film grown at 700 °C and 400 mTorr. The KTN films grown at 300 mTorr contain only 79 - 91 % K, in close agreement with previous researchers whose results for KTN on MgO by PLD yielded 84-92 % K at 300 mTorr.[102] By further increasing the partial oxygen pressure to 400 mTorr during growth films, containing 90 - 101 % of stoichiometric K were produced. No trend in the K content with growth temperature was observed within the temperature range of our experiments. The deposition rate varied from 0.5 to 2 Å per laser shot. Films grown at 300 mTorr tended to be thicker than those grown at 400 mTorr. Other

variations in film thickness are attributed to the placement of the plume center with respect to the substrate.

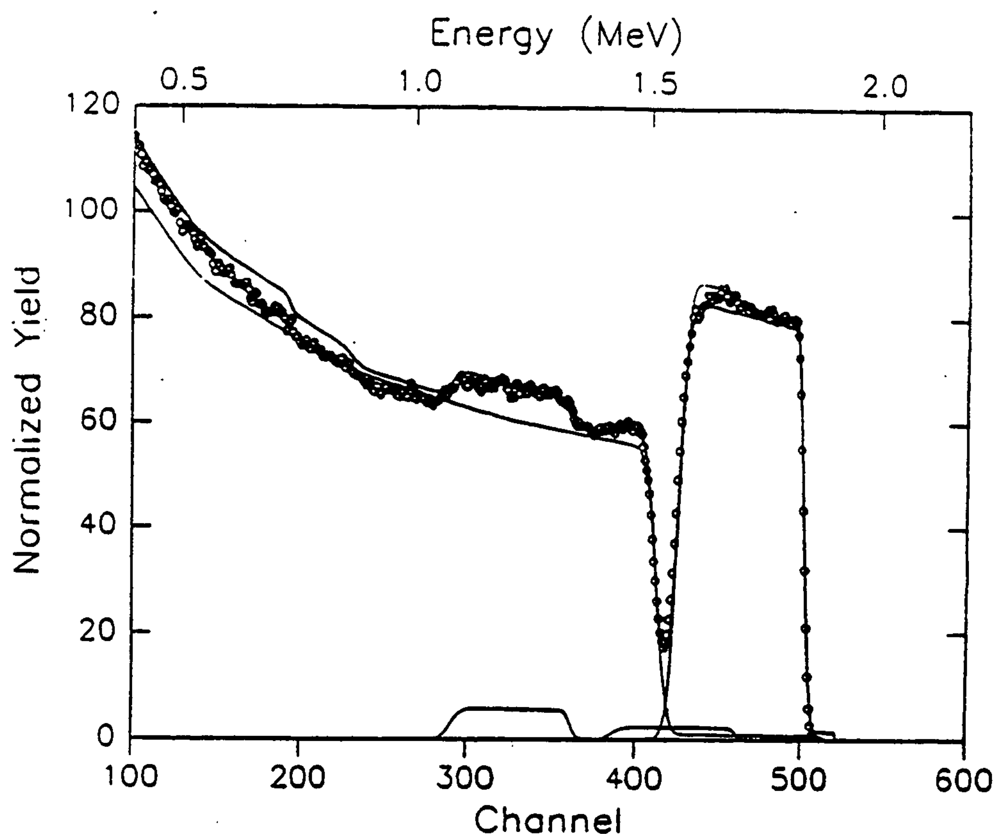


Figure 29. RBS raw data (circles) and fit (lines) for a KTN film grown on $(100)_{-p}$ LAO at 700 °C and 400 mTorr. The fit resulted in a thickness of 0.28 μm and composition $K_{.9}Ta_{.92}Nb_{.08}O_x$.

Cross-sectional TEM was used to look at a film composed almost entirely of pyrochlore, shown by the XRD scan in Figure 30. Figure 31 shows a cross-section of the KTN film that was grown at 650 °C and 100 mTorr $Po_2$. Columnar grains are seen extending the thickness of the film. These grains are ~ 50 - 100 nm thick. A crack is present at the KTN/LAO interface which is probably due to the stresses induced during the processing of the

TEM sample and it identifies the weakest part of the structure. A higher resolution micrograph of the KTN/LAO interface is shown in Figure 32. The interface between the KTN and the LAO substrate is quite smooth. The pyrochlore KTN nucleates in several orientations, using the LAO substrate to calibrate the magnification results in lattice spacings of approximately 3.11 or 6.22 Å. These values correspond closely to the spacing between the (222) and (111) pyrochlore planes observed in the XRD scan of this sample. These planes make angles of approximately 0° and 71° with the LAO surface and most likely add to the strong intensity of the {111} reflections seen in the XRD scan of this sample. The presence of the perovskite KTN phase is not found in agreement with the XRD data that shows only minute reflections for perovskite KTN.

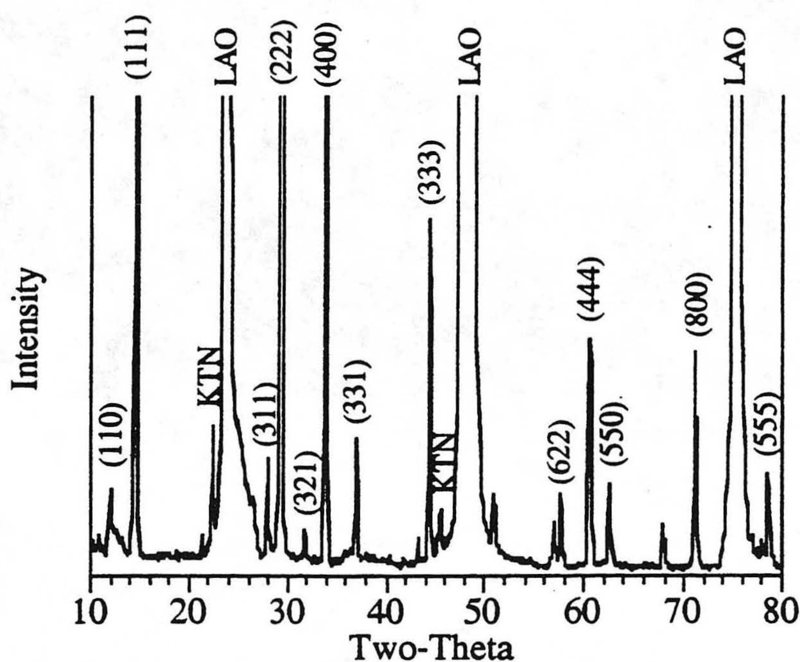


Figure 30. XRD scan of a KTN film grown on a $(100)_{-p}$ LAO substrate at 650 °C and 100 mTorr. The indexing refers to the KTN pyrochlore phase. Unlabeled peaks are pyrochlore planes which could not be identified exactly.

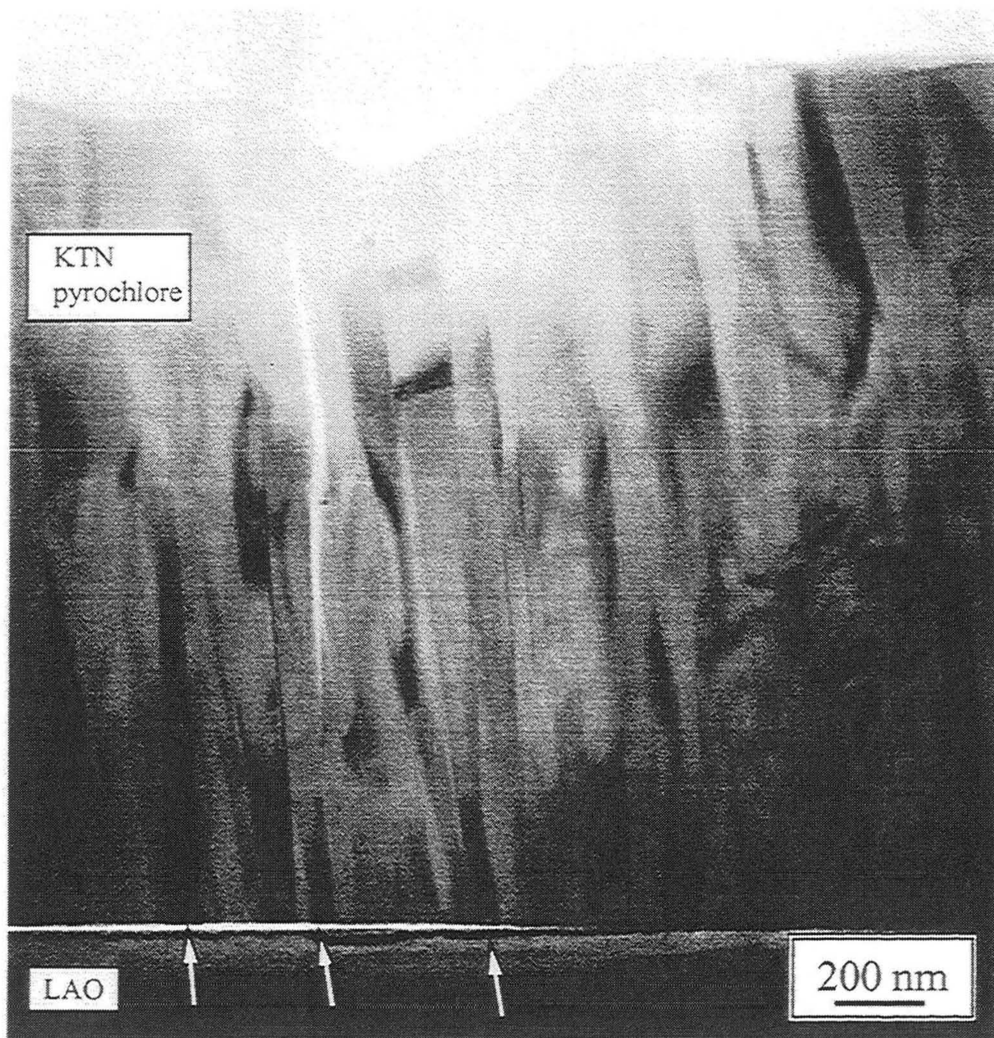


Figure 31. TEM micrograph of KTN/LAO heterostructure showing columnar grains of pyrochlore. The grains are 50 - 100 nm thick.

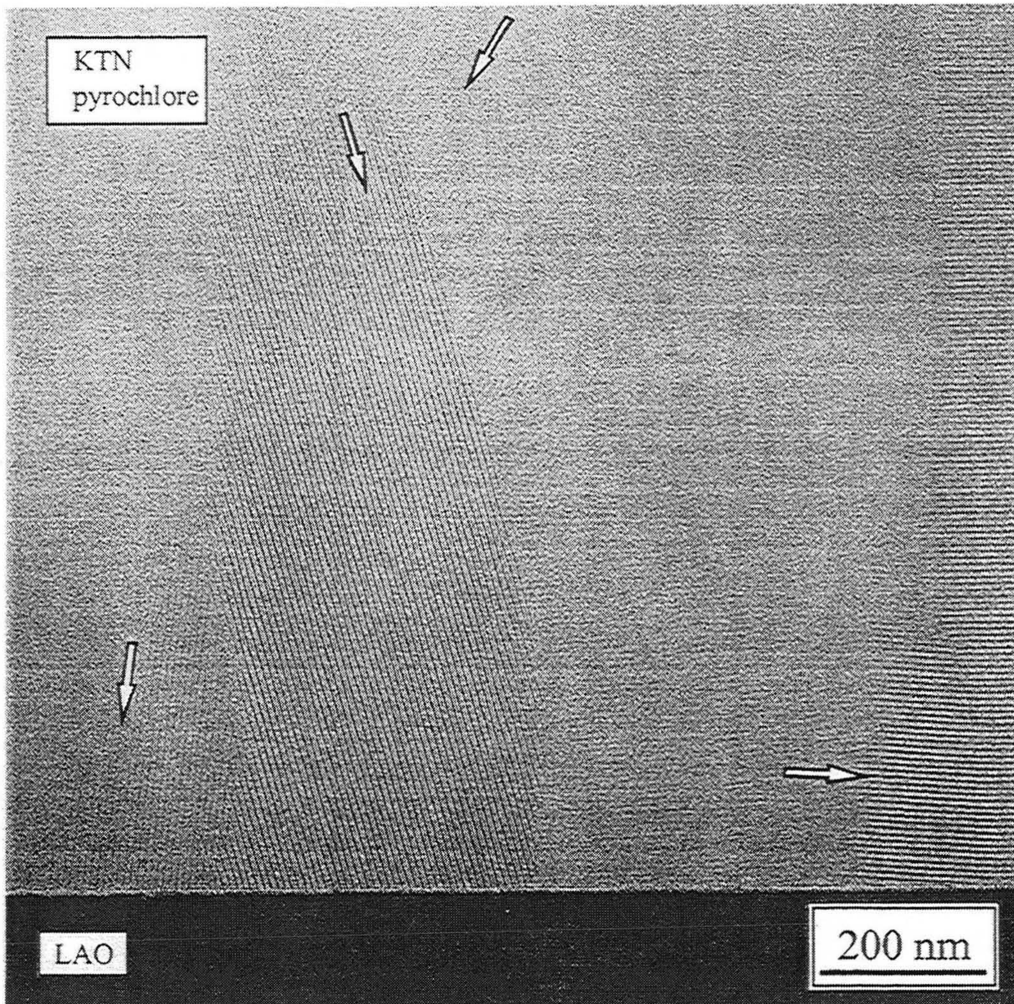


Figure 32. TEM micrograph of the interface of a KTN/LAO film. The lattice constant of the KTN is 3.11 or 6.22 Å indicating that it is (111) or (222) pyrochlore. The KTN grows randomly oriented on the LAO substrate.

### 5.2.4 KTN Growth on Conducting Oxides

#### 5.2.4.1 Lanthanum Strontium Cobalt Oxide

The difficulty in growing pyrochlore free KTN on Pt surfaces led to the investigation of conducting oxide materials for bottom electrodes to the KTN. LSC was originally identified as a candidate because of its success as a bottom electrode for other ferroelectric materials. First, $La_{.5}Sr_{.5}CoO_3$ (LSC) conducting oxide films were deposited by pulsed laser deposition on $LaAlO_3$ substrates to check the conductivity of the LSC films grown at 600, 650, 700 and 750 °C. The remaining deposition parameters were kept constant: target batch #2 was used ($K_{1.15}Ta_{.87}Nb_{.13}O_3$), substrate to target distance ~ 5 - 6 cm, $Po_2$ = 100 mTorr, laser shots ~ 3900, laser pulse frequency was 5 Hz, and laser energy was 600 mJ which corresponded to a laser energy density at the target of about 1.9 - 2.5 J/cm$^2$. X-ray diffraction scans, Figure 33, of the films indicate that the LSC grows in the (100) direction and that there is a small amount of pyrochlore present at all growth temperatures. RBS measurements showed smooth films ~ .25 µm thick (.65 Å/pulse). The stoichiometry of the films was $La_{.6}Sr_{.5}Co_{1.1}O_{2.8}$. Two - point resistance measurements (Appendix C) of the LSC films showed they are metallic. A film grown at 600°C exhibited resistances of 18.7 and 23.7 ohms at 84 and 300 K and at 650 °C the resistance at room temperature is 7.5 ohms corresponding to resistivities in the metallic range (< $10^{-2}$ Ω-cm). These values were similar to those observed with the other films; there was no apparent trend with temperature. The contacts were made by sputter depositing 1500 Å Pt or Pd:Au (300:1400Å) contacts through a shadow mask; silver epoxy was used to attach copper wires. The measurements were made with a Keithly electrometer at 100 µ amps.

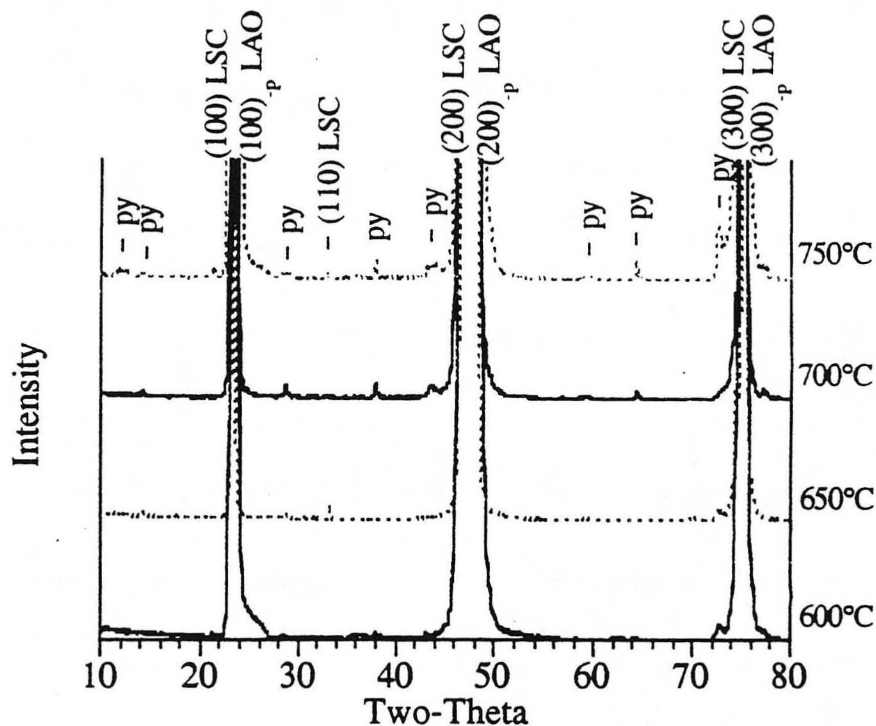


Figure 33. Theta-2theta x-ray diffraction scans of LSC/LAO heterostructure at 600, 650, 700 and 750 °C. (py - pyrochlore)

KTN/LSC films were deposited on $LaAlO_3$ substrates at 600, 625, 675 and 700 °C using 300/100 mTorr $Po_2$. The remaining deposition parameters were nearly identical to those used above, except that the number of laser shots varied from 2000 - 4500 for the LSC films and 3000 - 4500 for the KTN films. The laser energy was kept constant at 600 mJ or ~ 1.9 - 2.5 J/cm$^2$.

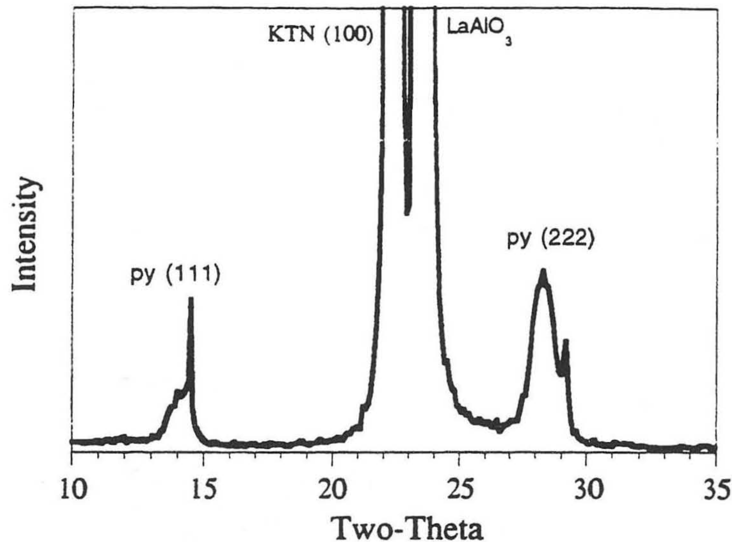


Figure 34. Θ-2Θ XRD scan of KTN/LSC/LAO heterostructure grown at 675°C showing (100) oriented perovskite KTN and twin {111} pyrochlore peaks (py). The KTN film was grown at 675°C and 300 mTorr.

XRD diffraction scans of samples grown at 675 and 700 °C show the presence of two pyrochlore phases as well as (100) perovskite (3.98 Å) as seen in Figure 34 for a 675 °C growth. The smaller lattice constant (111) and (222) pyrochlore orientations (6.10 and 3.06 Å, respectively), sharper "py" peaks on XRD scan, fall where we expect the KTN pyrochlore. The larger lattice constant (111) and (222) pyrochlore orientations (6.32 and 3.10 Å, respectively), broader left-hand peaks, we attribute to either a $LaAlO_3$ or LSC pyrochlore or some unknown pyrochlore mixture of the two since the presence of this phase is seen in LSC/LAO samples containing no KTN and the peak positions do not match any possible LAO or LSC reflections but are consistent with what one would expect for a pyrochlore phase.

Films grown at 600 and 625 °C show minuscule peaks which could be pyrochlore along with the (100) oriented perovskite phase, Figure 35.

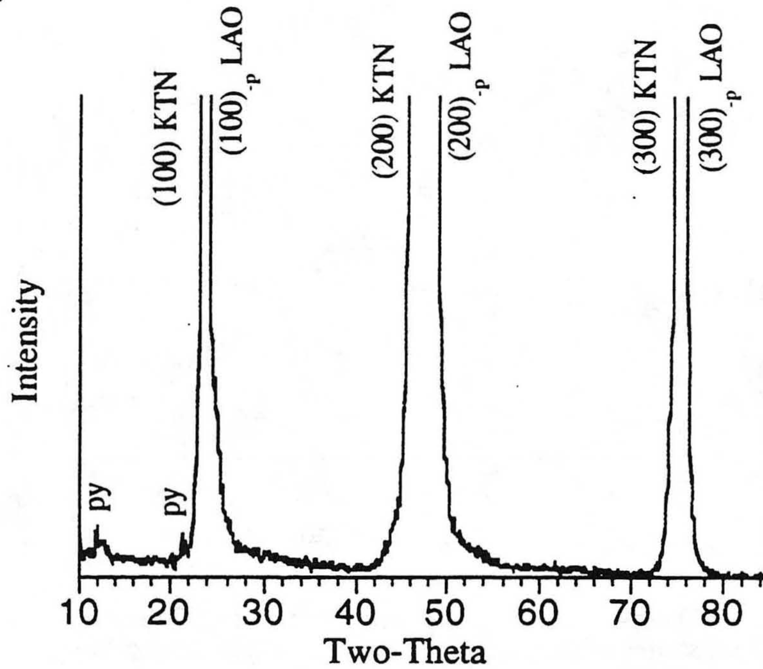


Figure 35. Θ-2Θ XRD scan of a KTN/LSC/LAO heterostructure grown at 600 °C and 300/100 mTorr. (py - possibly pyrochlore, KTN - perovskite)

Two-point resistance measurements of the LSC film resistance vs. temperature after subsequent KTN deposition at 600°C show that the LSC layer is semiconducting. Figure 36 plots the resistance of this film and an LSC film grown at the same temperature 600 °C without subsequent KTN deposition. The semiconducting behavior of the LSC was seen for higher temperature KTN/LSC growths as well. The contacts to this sample were made by etching back to the Pt sputtered corners of the sample using 50% HF and directly attaching copper wires with silver epoxy to the Pt.

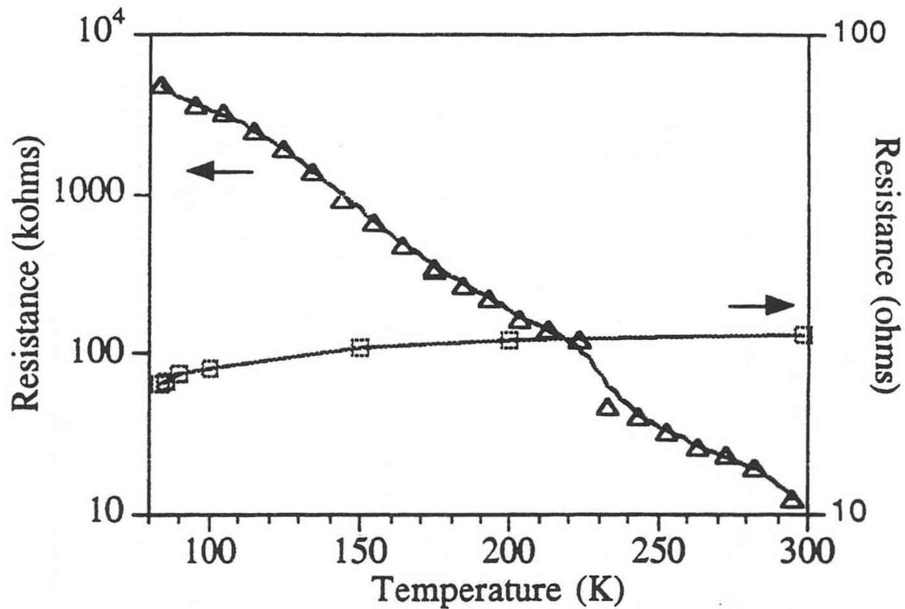


Figure 36. Two-point resistance measurements of LSC grown at 600 °C on LAO substrates with (triangles) and without (squares) subsequent KTN deposition at 600 °C.

Simulation of an RBS measurement of a KTN film grown at 675 °C, Figure 37, gave a film thickness ~ 0.2 μm and composition $K_{.83}Ta_{.88}Nb_{.12}O_x$. The LSC film thickness was estimated to be 61 nm. The D.C. resistance across the LSC bottom contact showed semiconducting behavior varying from 340 kΩ at 83 K to 5 kΩ at 298 K. Top contacts were made to this sample by using a shadow mask during sputtering of Pd:Au (300:1200 Å). Silver epoxy was used to bond Cu wires to the 0.23 $mm^2$ contacts resulting in capacitors. The D.C. resistance of the resulting capacitive devices is ~ 26 MΩ at room temperature and increases to 5.3 GΩ (~ 6.1 x $10^{11}$ Ω-cm) at 83 K (Figure 38). Measurements using the capacitance bridge resulted in room temperature dielectric permittivities of 76 at 100 Hz and 43 at 1000 Hz. These values are about 5 and 9 times less than what is measured for single crystal KTN,

respectively. In addition, the dielectric permittivity slowly decreased when the temperature was lowered as opposed to rising to a maximum at 90 K, the expected transition temperature.

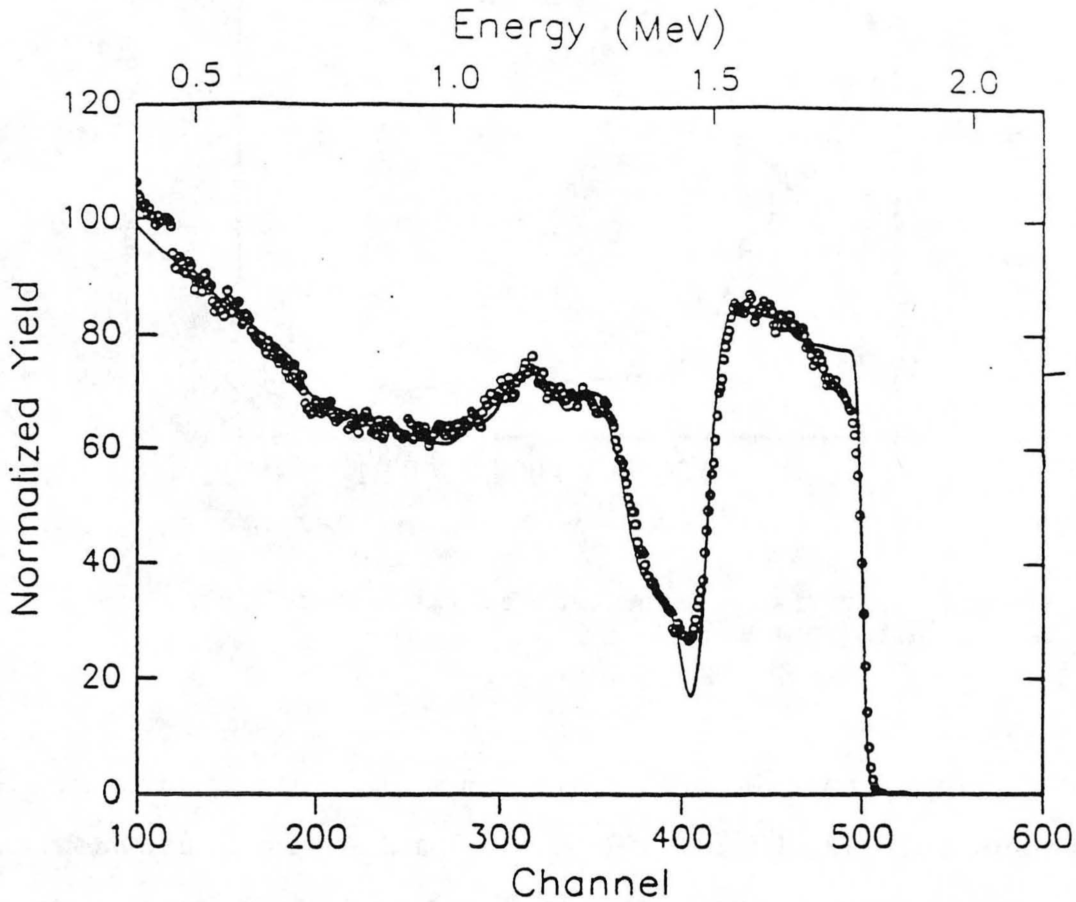


Figure 37. RBS data (circles) of a KTN/LSC/LAO heterostructure grown at 675 °C. The data simulation (line) indicates that the KTN film is ~ 0.18 μm thick and has composition $K_{.83}Ta_{.88}Nb_{.12}O_x$.

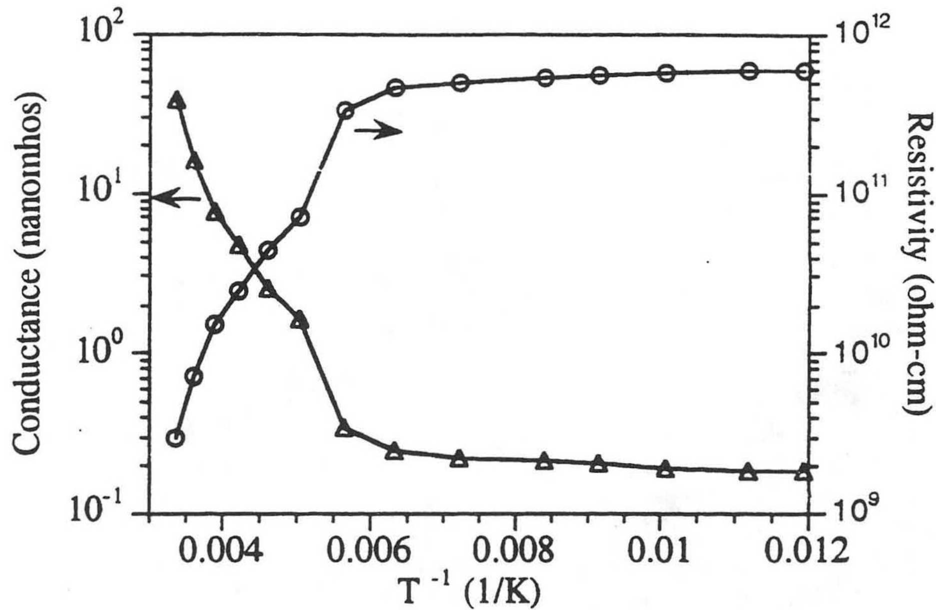


Figure 38. Conductance vs. temperature of a capacitive device from a KTN/LSC/LAO grown at 675 °C.

Photolithography was also used to form top contacts producing circular capacitors of various diameters: 50, 70, 100, 200, 350, 700, 1100, and 1400 μm. Some films showed statistical shorting; the larger area capacitors were all shorted and the resistance of the smaller capacitors fluctuated. Capacitance measurements were made on a film containing a minute amount pyrochlore grown at 600 °C using non-shorted, higher resistance capacitors. A HP LCR meter was operated at 120 Hz at room temperature, resulting in extremely low values of capacitance: 6 and 80 pF for 50 μm and 200 μm diameter capacitors, respectively. The values for capacitance scale with size. The thickness of the KTN film measured using RBS was 0.17 μm, leading to room temperature relative dielectric permittivities of 50 - 60. RBS also

indicated that the films were very smooth but ~ 70% K deficient. Polarization versus electric field measurements on these films did not show ferroelectric hysteresis.

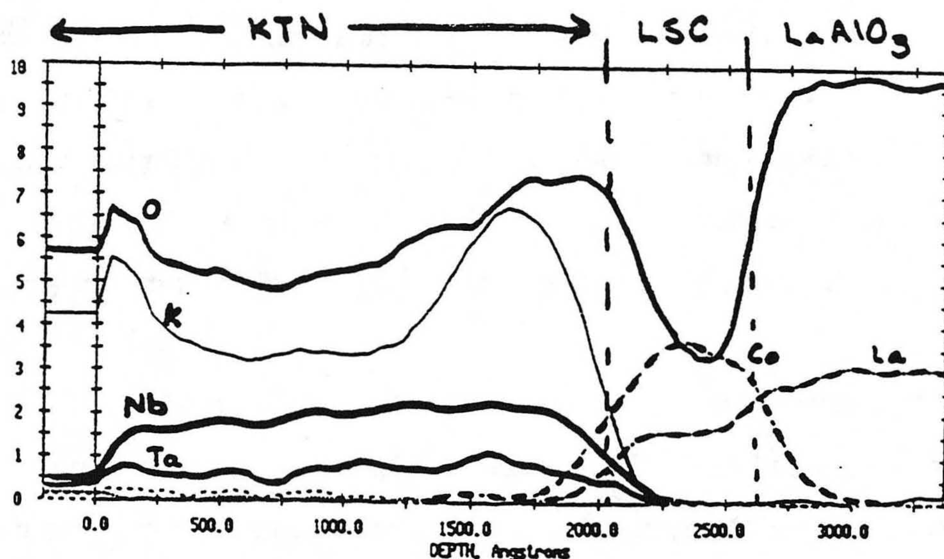


Figure 39. Auger depth profile of KTN/LSC/LAO heterostructure grown at 675 °C.

In order to discover the origin of these poor electrical properties, Auger and TEM were performed on the 675 °C grown film. The Auger depth profile of this film shows an inhomogeneous KTN layer with interdiffusion between the layers possibly as far as 200 Å. The KTN film is divided into two portions. The thickness of these portions is based upon the total thickness of the LSC layer, 61 nm, as determined by RBS; the interface layer is then 75 nm thick and the surface layer is 130 nm thick. At the surface of the film the K and O concentrations peak. After they drop they reach a steady level similar to the Ta and Nb concentrations. Almost two-thirds of the way into the structure the K and O content, and to a

much lesser extent the Ta and Nb content, peak. Then the LSC phase begins, which is marked by a small dip in O with corresponding increases in the La and Co contents. The start of the LAO substrate is marked by further increases in LAO and O.

Cross-sectional TEM performed on this film indicates that the LSC layer is 65 nm thick, in close agreement with the RBS results, Figure 40. The KTN is again shown to be composed of two layers; the surface layer is 250 nm thick and the interface layer, which appears to be denser is 140 nm thick. Combined, these values add up to twice the thickness determined by RBS, indicating that the films are not as dense as expected for stoichiometric KTN. Recalculation of the dielectric permittivity gives 145 and 82 at 100 and 1000 Hz, respectively. The lattice spacing is as expected, ~ 3.95 Å in both regions of the film (Figures 41 and 43).

The KTN grains are columnar, highly c-axis oriented and run the full thickness of the film with a diameter between 50 and 100 nm. There are voids between the grains starting at the interface between the two KTN layers. Moiré fringes are evident in many of the grains indicating a high degree of orientation with the LAO. Most of the grains show a square pattern of fringes aligned with the square pattern on the LAO (Figures 42 and 43). The grains are faceted on (001) and some have extremely square corners (Figure 41). There is evidence that small amounts of pyrochlore are present at the tops of a few of these columnar grains. The pyrochlore is not found at boundaries between the columnar grains, nor is it present as a continuous layer at either interface Given that both KTN layers are perovskite, the dramatic changes in the K and O with film depth indicate that the film contains a highly defected layer. The defects in this layer appear to be primarily due to K-O Schottky defects.

The LSC showed no fringes and has a rather patchy appearance, indicating that it grows in a number of orientations but probably retains some preferred orientations imposed by the LAO substrate, Figure 44. The LSC lattice parameter was measured at 3.8 Å. Another

pyrochlore phase was also discovered at the LSC/LAO interface confirming the presence of two distinct pyrochlore phases seen in the XRD data.

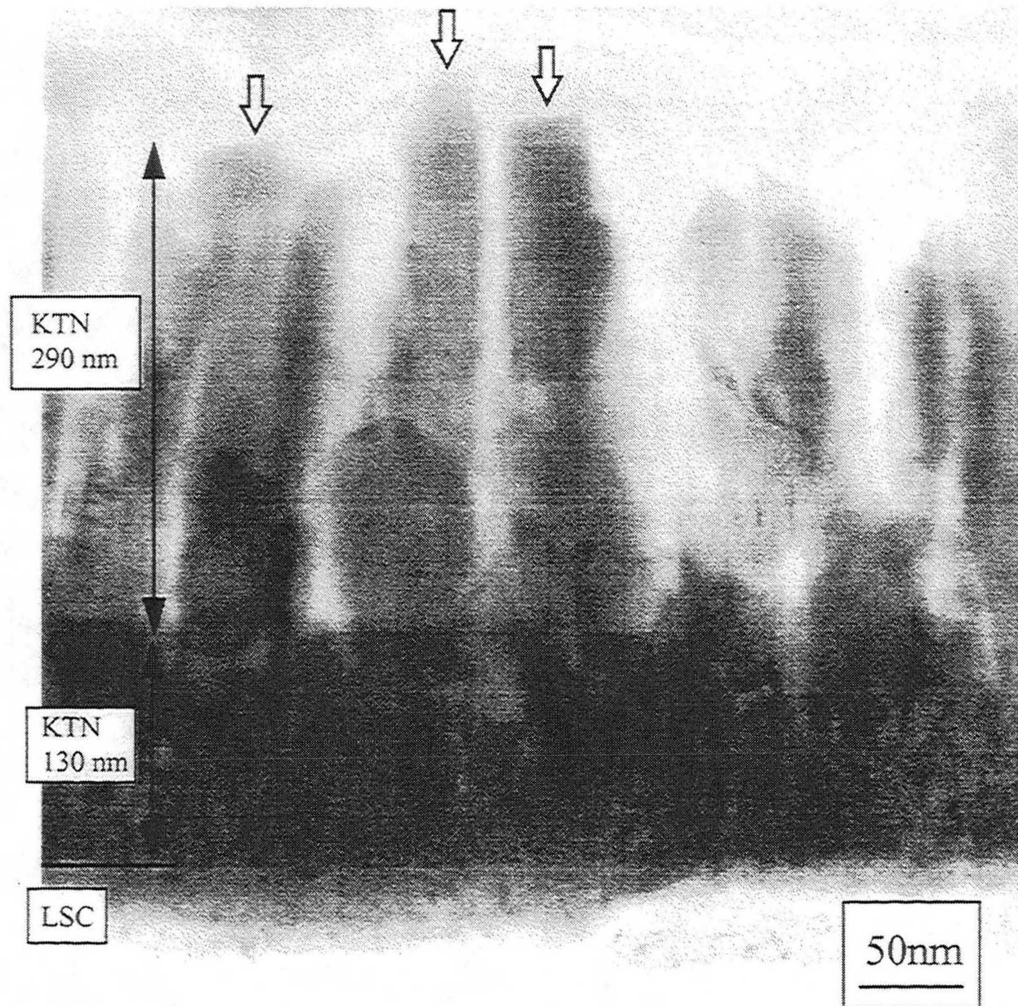


Figure 40. Cross-sectional TEM micrograph showing columnar grains of KTN from a KTN/LSC/LAO film grown at 675 °C. The KTN layer is divided into two parts; the surface region is ~ 290 nm and the interface part ~ 130 nm. The LSC is the weakest point and has cracked.

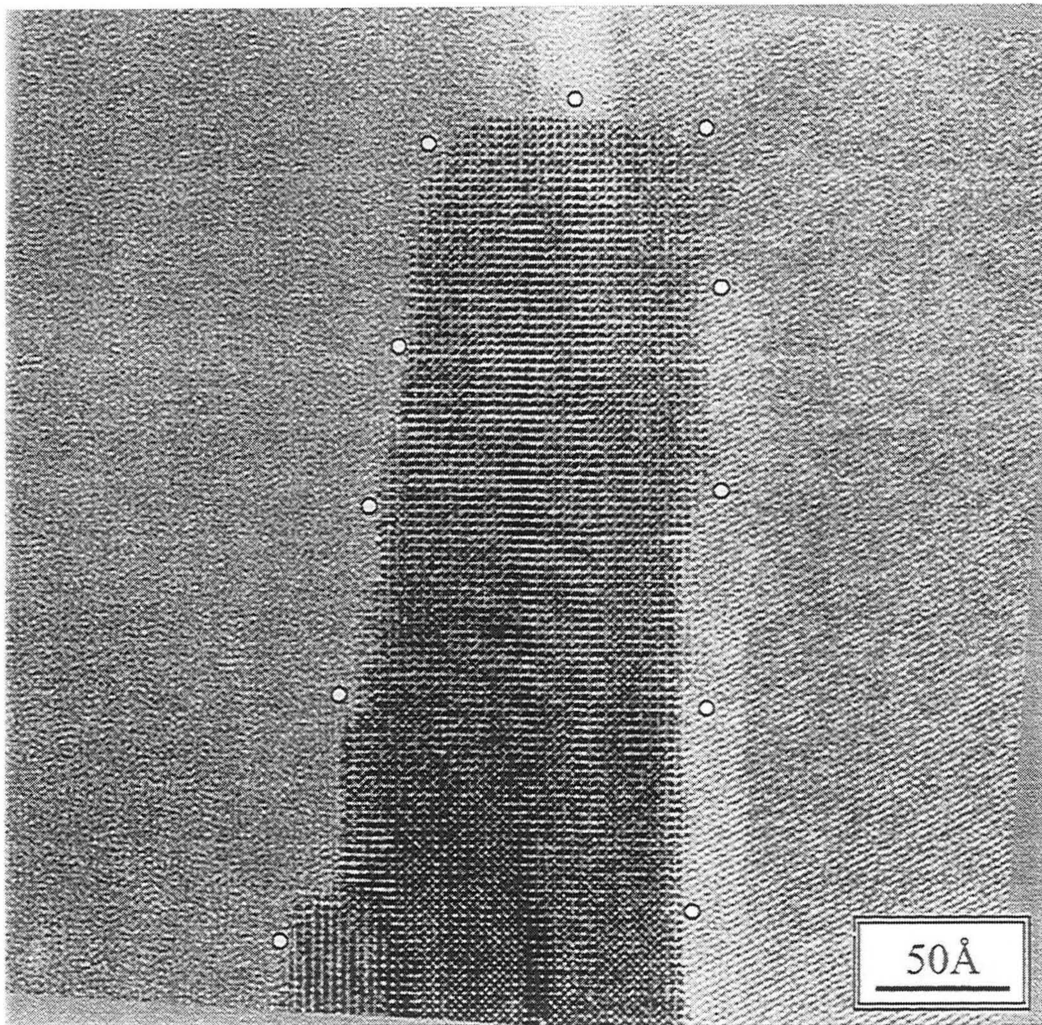


Figure 41. Cross-sectional TEM micrograph showing one of the columnar grains of KTN from a KTN/LSC/LAO film grown at 675 °C. The grain is highly faceted with voids on the sides. The lattice constant ~ 3.9 Å.

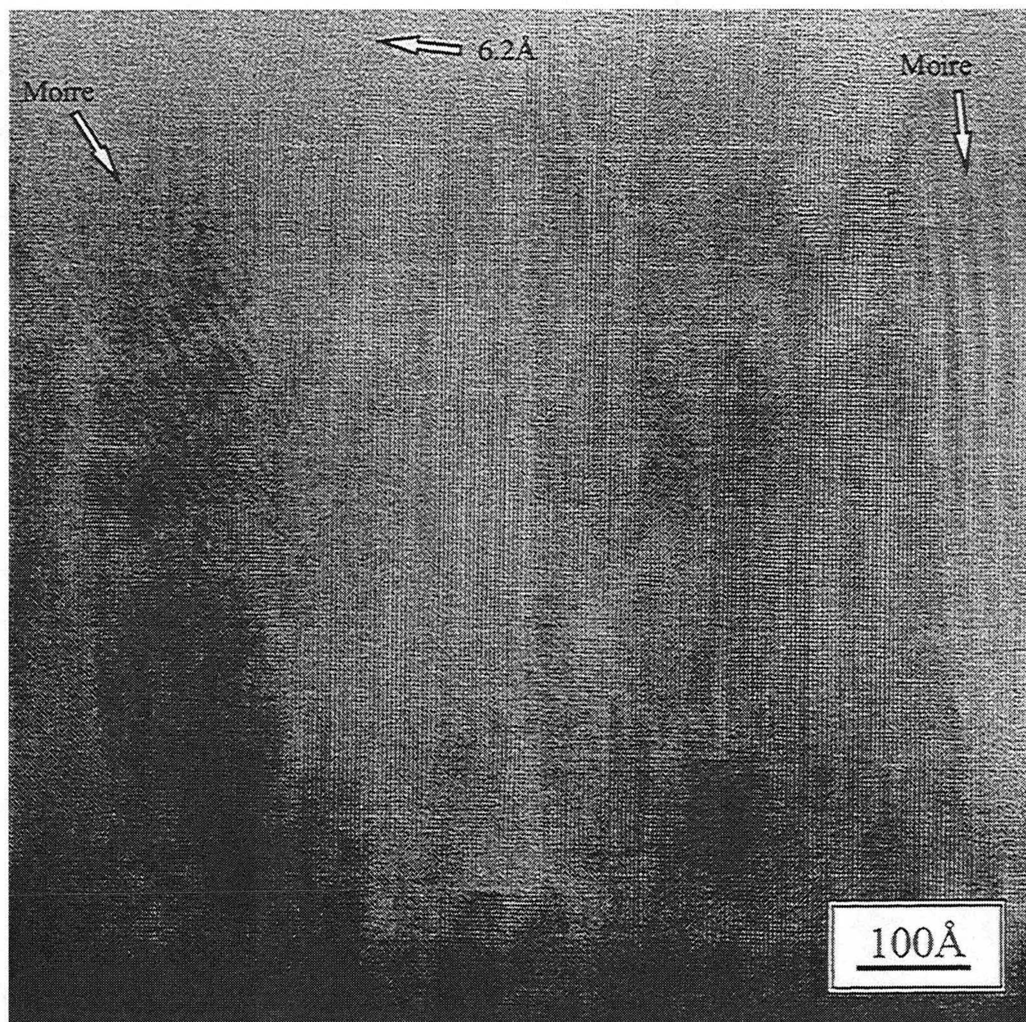


Figure 42. Cross-sectional TEM micrograph of KTN in a KTN/LSC/LAO film grown at 675 °C showing moiré fringes in different directions. The majority of the film has a lattice constant ~ 3.9 Å, but there are some small regions near the top of some of the grains that have lattice spacings ~ 6.2 Å.

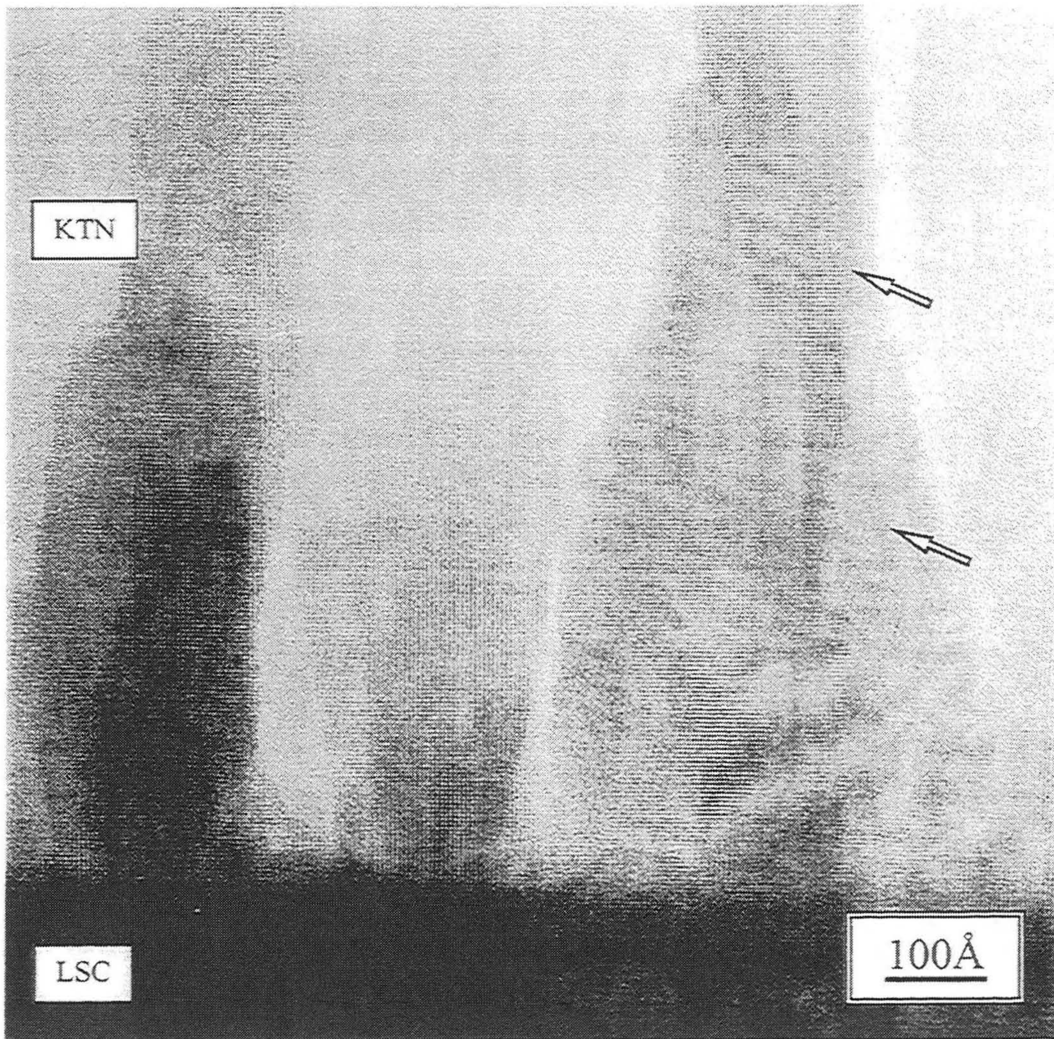


Figure 43. Cross-sectional TEM micrograph of KTN/LSC from a KTN/LSC/LAO film grown at 675 °C. Moire fringes are evident in the KTN film. The lattice constant of the LSC was measured ~ 3.8 Å.

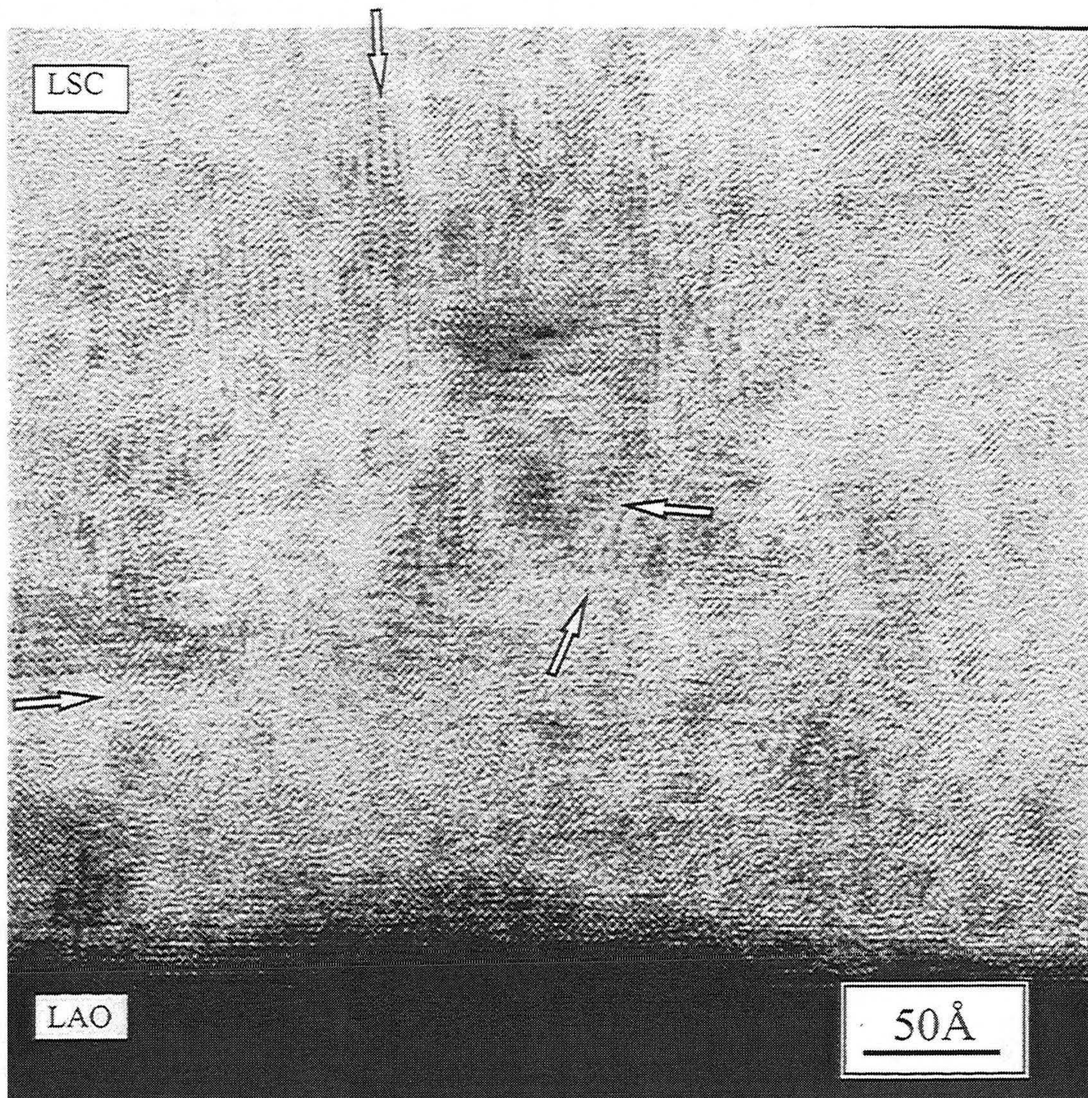


Figure 44. Cross-sectional TEM micrograph of LSC/LAO from a KTN/LSC/LAO film grown at 675 °C. The interface between the LSC and LAO has a lattice spacing ~ 6.04 Å. The LSC is composed of many orientations of grains, the largest block ~ 100 Å across.

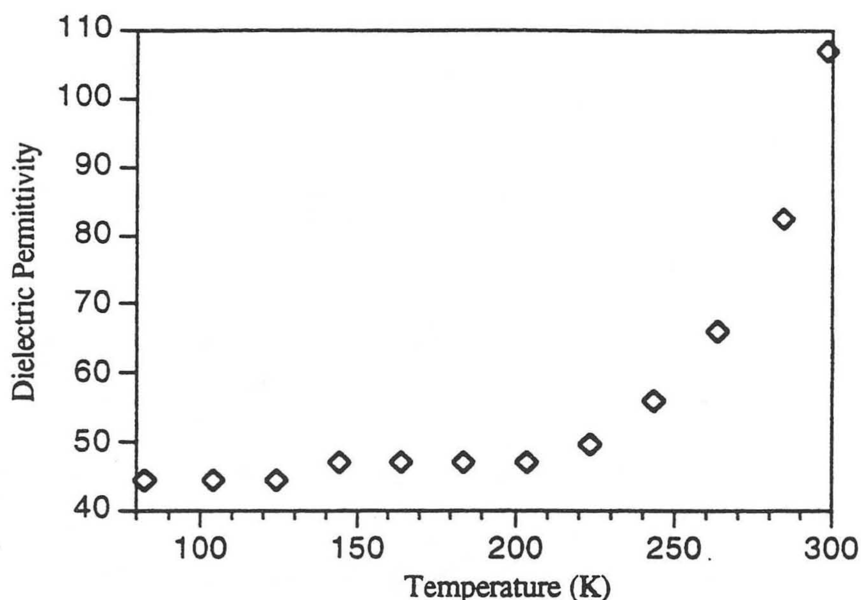


Figure 45. Dielectric permittivity vs. temperature for measured at 100 Hz and 301 μV A.C. signal of a KTN/LSC device grown on Pt/Ti/SiN/Si at 600 °C.

Films grown under identical conditions at 600, 625 and 675 °C on Pt/SiN/Si and Pt/Ti/SiN/Si substrates had electrical properties similar to those reported above. X-ray diffraction showed that the films typically contained small amounts of pyrochlore, although it was possible to produce films of only the perovskite phase at 600 °C. Increases in the laser energy also produced pyrochlore-containing films. Photolithography was performed on the films to produce circular top contacts of various diameters: 50, 70, 100, 200, 350, 700, 1100, and 1400 μm. The resistances of the films were measured using a HP LCR meter operating at 100 - 1000 Hz. Many of the films grown at these temperatures exhibited statistical shorting where the larger diameter capacitors were either shorted or had significantly reduced

resistance compared to the smaller area capacitors that often showed resistances that were off scale, > 20 MΩ.

The dielectric permittivity of the KTN films grown on Pt/Ti/SiN/Si is independent of growth temperature and the presence of pyrochlore. Capacitance measurements were made on a film grown at 625 °C using the high resistance capacitors. The HP LCR meter was operated at 120 Hz at room temperature and resulted in extremely low values of relative dielectric permittivity, 110 - 120. The dielectric loss was ~ 0.25. Figure 45 shows the relative dielectric permittivity behavior for a KTN film grown at 600 °C. The dielectric permittivity decreases with decreasing temperature and never reaches a maximum at the expected transition temperature. At room temperature the permittivity matches that of the pyrochlore free film grown at 625 °C.

#### 5.2.4.2 Yttrium Barium Copper Oxide

KTN/YBCO films were grown on $LaAlO_3$, YSZ and $SrTiO_3$ substrates *in situ* to investigate YBCO as an electrode and look at the substrate effects. The YBCO was deposited at 760°C and 200 mTorr, the temperature was then reduced to 450 °C and the sample was allowed to anneal in 600 Torr $Po_2$ for 10 minutes. The temperature was increased to 675°C where the KTN growth took place in 300 mTorr. The laser energy density at the target was 2.3 - 3 J/cm$^2$. The pulse frequency was 5 Hz. After growth the substrate was cooled to 450 °C at 40°/min. and held for 10 minutes before cooling to room temperature at the natural cooling rate.

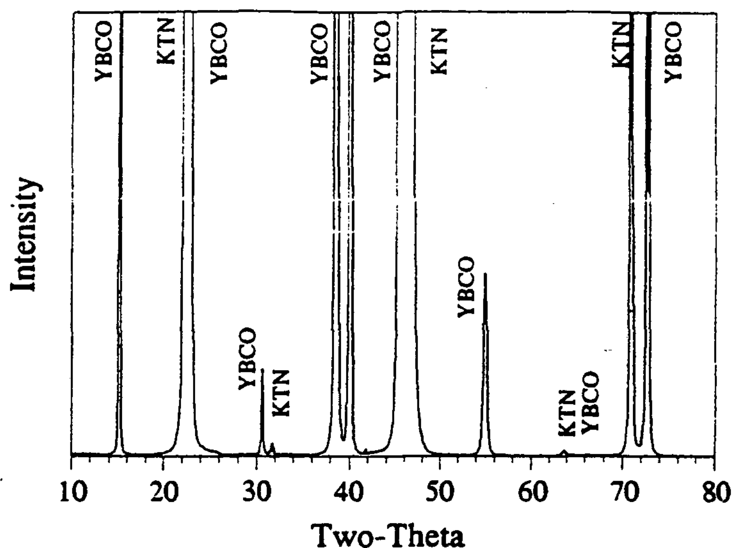


Figure 46. X-ray diffraction scan showing the (001) and highly (100) oriented YBCO and perovskite KTN films, respectively. The KTN film was grown on YBCO/STO at 675°C and 300 mTorr of oxygen.

XRD of the KTN film grown on the YBCO/$SrTiO_3$ structure at 300 mTorr and 675°C showed no evidence of pyrochlore or any unknown phases, Figure 46, while for YBCO/$LaAlO_3$ and YBCO/YSZ some KTN pyrochlore was found. Deposition on all substrates yielded oriented YBCO and KTN films, (001) and (100) respectively. RBS measurements of this sample indicate a KTN thickness ~ 0.20 μm and composition of ~ $K_{.78}Ta_{.88}Nb_{.12}O_x$, Figure 47.

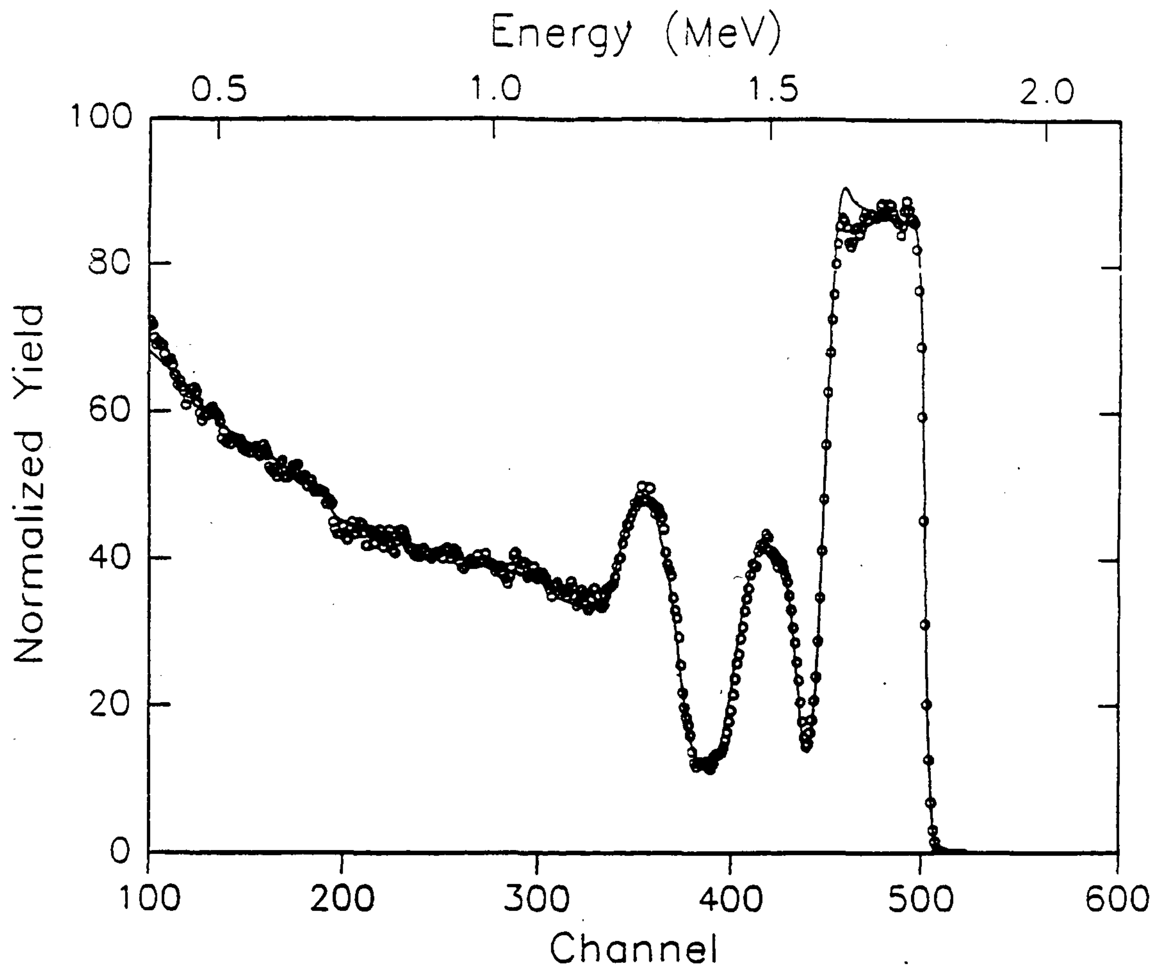


Figure 47. RBS measurement (circles) of a KTN/YBCO/STO heterostructure. The simulation (line) is for a KTN film thickness of 0.2 μm and composition of $K_{.78}Ta_{.88}Nb_{.12}O_3$.

Electrical measurements of the KTN film on the YBCO/$LaAlO_3$ and YBCO/YSZ structure yielded results similar to those of films grown on LSC with the exception that the YBCO remained metallic after subsequent KTN deposition (See Figure 48). Capacitance measurements vs. temperature at 100 Hz using 3 and 0.3 mV a.c. signal of the KTN/YBCO/STO devices yielded a broad and low peak in the dielectric permittivity at ~ 80 K,

as shown in Figure 49. The dielectric permittivity at room temperature is ~ 222 which is about 60 % of that of single-crystal KTN. The dielectric loss of the 1.54 $mm^2$ device yielded values between 0.01 and 0.03, similar to what is observed in single crystals at about 10 ° above the phase transition. The resistivity vs. temperature is shown in Figure 50; the increasing resistivity with temperature is seen in single-crystal materials. The D.C. resistance of the KTN capacitors varied from 0.3 to 60+ GΩ at 300 and 83 K, respectively. Ferroelectric hysteresis loops were also observed (Figure 51). The remanent polarization was 0.21 μC/$cm^2$ at 85 K.

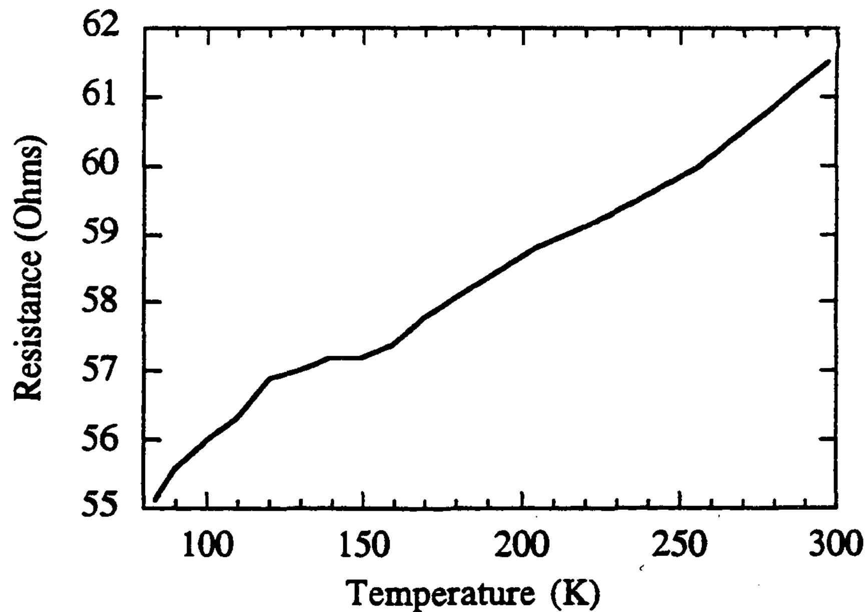


Figure 48. Resistance vs. temperature of YBCO bottom contact to a KTN/YBCO/LAO heterostructure grown at 675/760 °C. The YBCO is metallic.

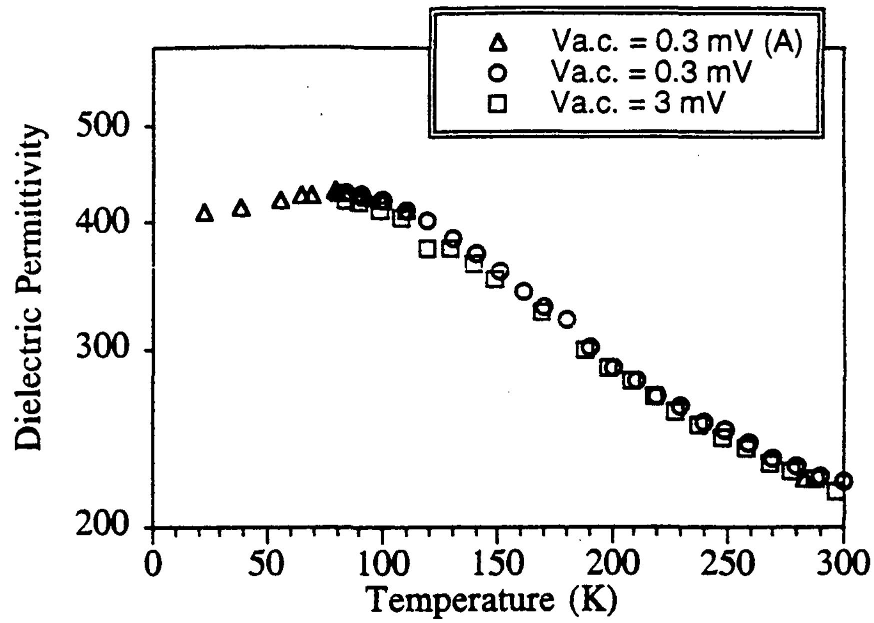


Figure 49. Dielectric permittivity vs. temperature of KTN grown on YBCO/STO at 675°C and 300 mTorr. The measurements were taken at 0.3 and 3 $mV_{ac}$. Data labelled A were obtained in a He exchange cryostat.

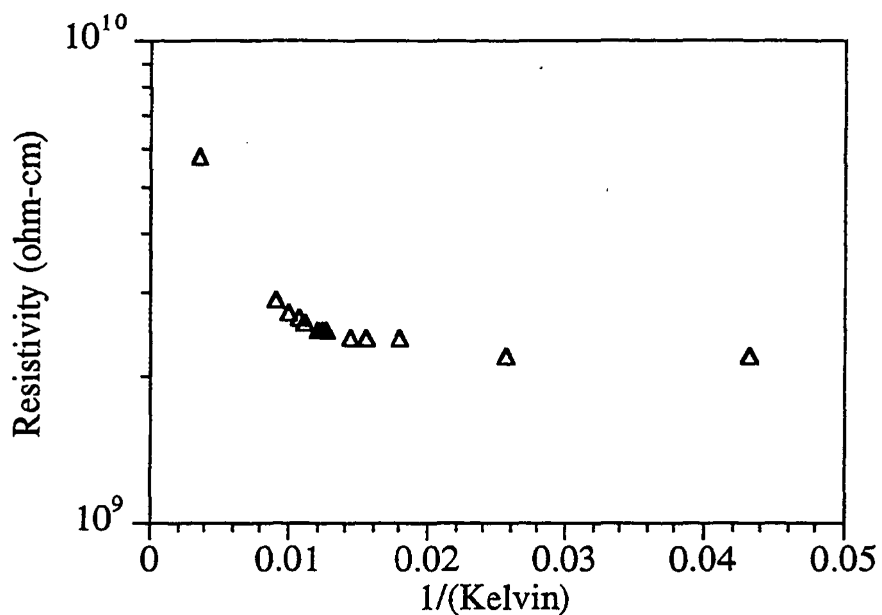


Figure 50. Resistivity vs. temperature for KTN/YBCO grown on STO substrates at 675/760 °C and 300/200 mTorr. Measurement was made at 100 Hz & 0.3 $mV_{ac}$.

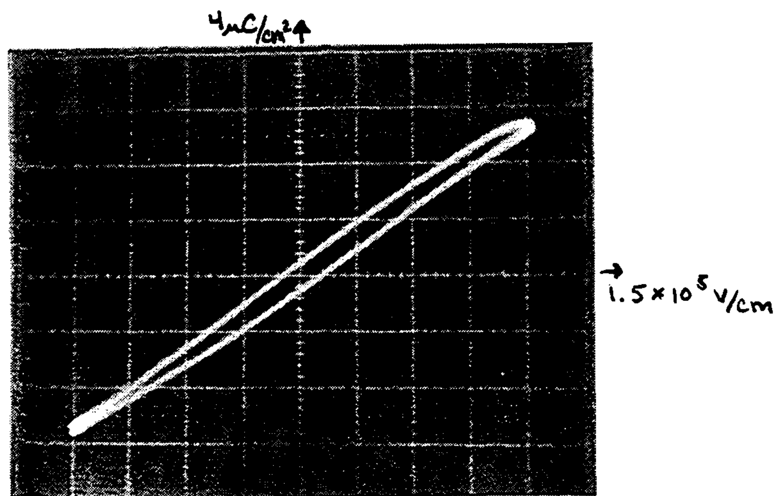


Figure 51. Hysteresis loop of a KTN film grown on YBCO/STO at 675 °C and 300 mTorr. The remanent polarization ~ 0.21 μC/cm2.

5.2.4.3 Strontium Ruthenium Oxide

First, a study of the growth of strontium ruthenium oxide (SRO) films was made on various substrates. The films were grown at 600, 675 and 775 °C at 200 mTorr and 600 mJ laser energy. The number of laser shots was 4500. Substrates were LAO, STO, Pt/SiN/Si (1000 Å/0.5 µm/0.5 mm) and Pt/Ti/SiN/Si (1130 Å/25 Å/0.5 µm/0.5 mm) and SiN/Si. Two point resistance measurements vs. temperature indicate the films are metallic, Figure 52 shows the resistance of one of the SRO films grown on (100) STO at 775 °C. Measurements of the resistance vs. temperature of the SRO films after subsequent KTN depositions at temperatures ≥700 °C showed that the films retained their metallic behavior. Such measurements were not performed on films grown at the other temperatures.

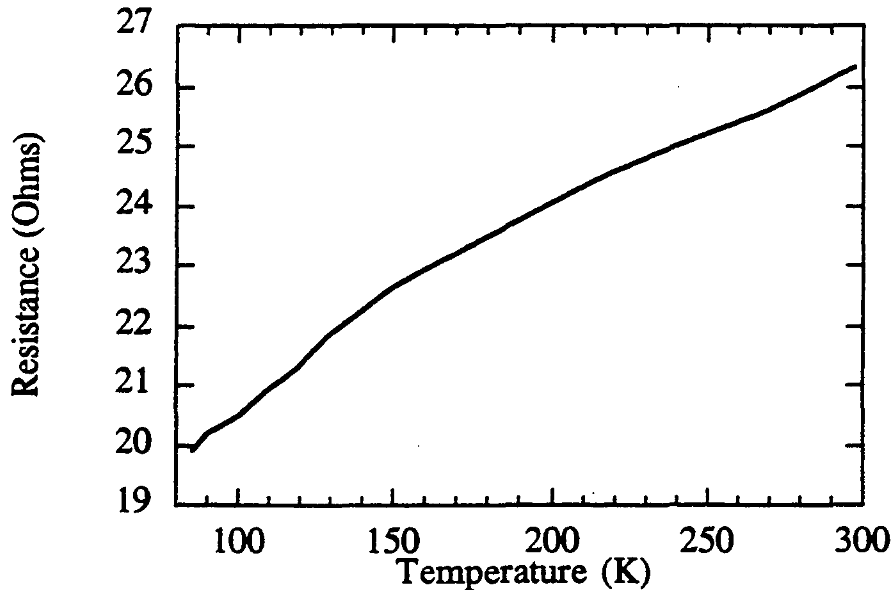


Figure 52. Two-point resistance vs. temperature of SRO without subsequent KTN deposition grown at 775°C on (100) STO.

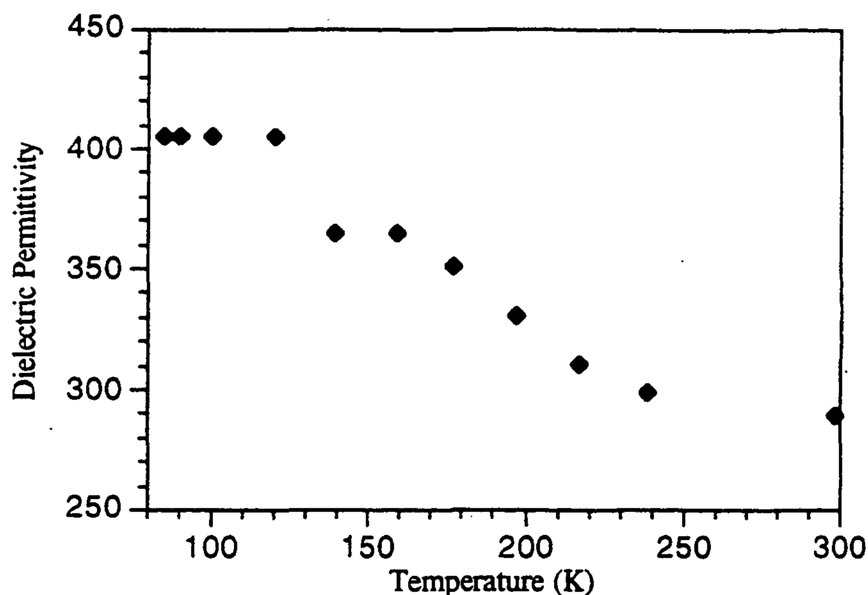


Figure 53. Dielectric permittivity vs. temperature for a KTN/SRO/LAO structure grown at 700 °C and 500 mTorr. The data was measured at 50 Hz and 0.3 $mV_{ac}$.

KTN/SRO growths were performed on SRO substrates at 700 °C and 300, 400 and 500 mTorr. At 300 mTorr $Po_2$ the dielectric permittivity of the KTN film is ~ 70 - 80 for frequencies between 20 and 120 Hz at 301 $\mu V_{ac}$ and room temperature. The films are 30 % potassium deficient. Measurement of the dielectric permittivity vs. temperature of a 100 µm diameter device shows that the values decrease only slightly with temperature. At 400 mTorr, 120 Hz and room temperature the dielectric permittivity ranges from 110 to 120. A variety of capacitors having different areas were measured and it was found that the dielectric permittivity is independent of capacitor area. The potassium deficiency is ~ 25%. The dielectric loss of the capacitors grown at 300 and 400 mTorr was ~ 0.1 - 0.2. At 500 mTorr, 120 Hz and room temperature the dielectric permittivity was measured at ~ 230 - 320. The potassium deficiency

is ~ 35 %. For a 350 μm diameter device the dielectric permittivity measured at 50 Hz and 300 μV increased from 290 at 298 K to 406 at 83 K, Figure 53. The dielectric loss dropped with temperature; at RmT the loss was 0.17 and dropped to values between 0.01 - 0.02 by 200 K. The frequency dependence of the film was measured at room temperature and 84 K. At room temperature the dielectric permittivity dropped with increasing frequency, while at 84 K there was no frequency dependence of the dielectric permittivity up to 1 MHz. In both cases the resistance increased as D.C. values were approached.

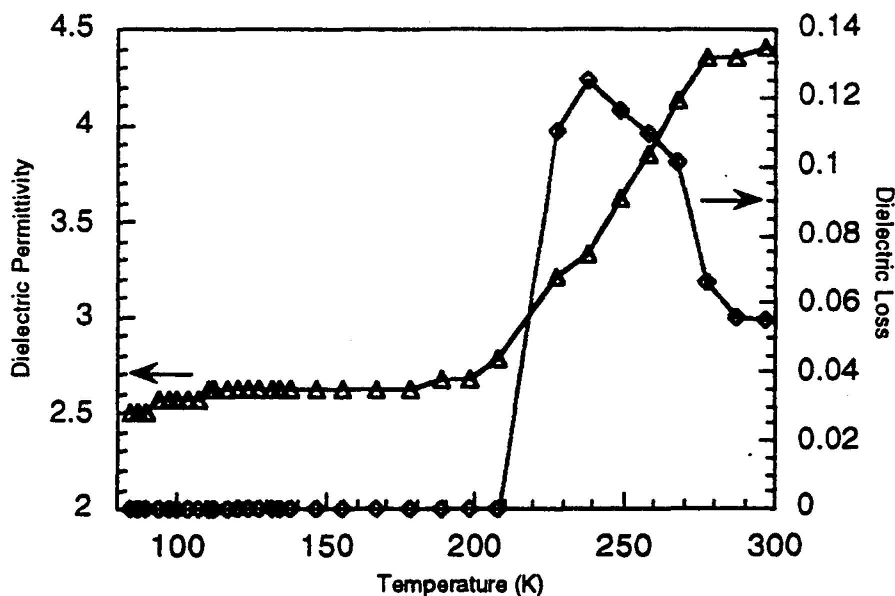


Figure 54. Dielectric permittivity and loss vs. temperature for a KTN/SRO device grown at 700 °C at 400/200 mTorr on SiN/Si.The data was measured at 100 Hz and 0.3 $mV_{ac}$.

Electrical properties for samples grown on Pt/Ti/SiN/Si and SiN/Si substrates grown without pyrochlore were measured. KTN/SRO films grown on SiN/Si substrates at 700 °C and 400/200 mTorr typically resulted in pyrochlore free films but of much lower perovskite

intensity than what is seen on other substrates and typically are composed of a higher fraction of (110) perovskite. It is possible that at the temperatures and oxygen pressures used for SRO growth that a $SiO_2$ layer consumes a portion of the SiN and affects the growth of the SRO layer; this was not investigated. The dielectric properties of the films at room temperature varied between 2 and 7 with losses ranging from about 0.1 to 0.3. Variable temperature dielectric permittivity measurements resulted in a slowly decreasing permittivity as the temperature was lowered, Figure 54. The dielectric loss reaches a maximum at 225 K as the permittivity drops, indicating that one of the dielectric mechanisms is freezing out. This space charge freeze-out is mimicked in the frequency dependence of the device taken at 84 K and room temperature. At room temperature the dielectric permittivity decreases with increasing frequency, with the dielectric loss maximum occurring at 800 Hz. The same behavior is seen at 84 K but the dielectric loss maximum shifts to 200 Hz indicating the temperature dependence of the mechanism. This film is ~ 25 % K deficient and has a graded composition of tantalum. Growth at higher pressures shows similar electrical behavior.

## 5.3 Integration

This section can be separated in two main issues that affect the development of KTN thin film devices. The first addresses the placement of KTN films on Si-based substrates, and the second relates to the photolithography steps used to define the top contacts.

The use of Pt as a bottom contact to the KTN poses several serious issues that need to be addressed more fully. The Pt is not altogether stable at the higher growth temperatures, > 600 °C used to grow KTN films via pulsed laser deposition. The Pt undergoes grain growth at these temperatures and tends to blister and hillock. But it retains its conducting nature. This has been found to increase the number of shorted devices. In addition, the Pt does not adhere

to the SiN as shown by a "scotch tape" test performed with removable tape. Additions of more oxidizing/nitride forming metals such as Ti and Cr, and $TiO_2$ between the SiN and the Pt does result in sufficient adhesion; however, problems with bubbling and buckling do not subside. We were unable to duplicate the results of Cooney et al. (see Section 4.2). Amorphous sputtered $TiO_2$ was deposited on silicon nitride/Si followed by Ti and Pt, but even without thermal assistance the films blistered.

Deposition of top electrodes underwent several steps in order to find the right combination for adherent top electrodes. It was found that top electrodes such as Au/Cr, Au/Pd, and Pt deposited by the electron beam process did not adhere well enough to stand up to wire bonding. Although E-beam deposition is a more desirable choice for metallic films when a lift-off is being performed, the more energetic sputtering process was better for making contacts on single-crystal KTN devices. Sputtering at 300 W power was tried using Au/Cr contacts. The lift-off took days in an ultrasonic acetone bath at 40 °C. Cr is difficult to deposit at lower powers because of the formation of Cr oxide. Deposition using Au/Pd electrodes at 100 watts resulted in lift-off within minutes in the ultrasound w/acetone at 40 °C. Adhesion of these contacts during wire bonding did improve to some degree but not by enough to make these contacts viable for use in the detectors.

## 5.4 Discussion

Growth of KTN films on conducting oxide electrodes was initiated in order to try and grow 100 % perovskite KTN since the pyrochlore containing films grown on Pt/SiN/Si substrates resulted in poor dielectric behavior. The use of LSC conducting electrodes in combination with Pt/SiN/Si and LAO substrates was employed in order to suppress the pyrochlore phase. At growth temperatures of 675 - 750 °C, KTN pyrochlore formation could

not be suppressed and the temperature was high enough to promote pyrochlore formation at the LSC/LAO interface. At growth temperatures ≥ 600 °C the behavior of the LSC film changed from metallic to semiconducting after subsequent KTN deposition. Dielectric permittivity behavior of these films is similar to those for KTN/Pt/SiN/Si regardless of whether there was pyrochlore present in the film. No films were produced that contained 100 % pyrochlore. Therefore, the lowered dielectric permittivities are assumed to originate in the perovskite phase. In addition, TEM results show that when the pyrochlore is present in small quantities it is not present at the grain boundaries nor is it present as a continuous layer within the KTN. It has such a minor presence that we would not expect it to affect the dielectric permittivity to the extent observed.

Clues to the origin of the electrical behavior can be gathered from the frequency and temperature dependencies of the permittivity. Dielectric permittivities measured at room temperature and ~100 Hz were fairly similar in magnitude when LSC was used as bottom contact to the KTN: 80 - 110. The dielectric permittivity at 1 kHz dropped to similar values, 43, that are observed upon cooling to 83 K, ~ 45. The decline in dielectric permittivity at frequencies < 1 kHz is usually due to a fall-off of space charge polarization. The freeze-out of dielectric permittivity reaches a constant value by 180 K and corresponds to a large drop in the film conductance from 300 - 180 K. The conductance of high quality KTN single crystals behaves in the opposite manner: the conductivity increases slightly as the temperature is lowered. The conductance behavior of the KTN film is consistent with the presence of charged mobile defects responsible for ionic conductivity in insulating materials. The apparent freeze - out and frequency fall-off of the dielectric permittivity also indicate the presence of atomic-scale defects. Because the voids seen between the KTN grains run the length of the film and represent a small volume, it can be assumed that they act as small parallel capacitors having a negligible contribution to the degraded dielectric permittivity.

The presence of a defective KTN layer is strongly supported by Auger measurements that indicate that two-thirds of the KTN film contains ~ 1/2 of the K and 3/4 of the O present in the remainder of the film. Because potassium ions have single valency and oxygen ions have double valency the K and O in the defective layer preserves the KTN's charge neutrality primarily via compensating K and O defects. It should be noted that both of the KTN layers may contain defects but both are perovskite as seen in the TEM images. Thickness measurements of the KTN based on TEM vs. RBS conflict, which is not surprising considering the inhomogeneity of the film and the method used to calculate the thickness in RBS. RBS measures an aerial density of atoms which is then used with the theoretical atoms/volume to calculate the thickness of the film. If the film is not homogenous or the density not as expected, this can result in erroneous values of thickness. It is more difficult to detect fluctuations in the K and O concentrations with RBS because of the low backscatter yield of the lighter K and O ions and apparent concentration variations due to film roughness. The dielectric permittivity more than doubles if values from cross-sectional TEM are used to calculate the dielectric permittivity of the films for KTN/LSC/LAO films, leading to permittivities ~110 at room temperature and 100 Hz. Expected values of dielectric permittivity at room temperature are 380.

It is also possible that the unstable KTN and Pt electrodes can influence dielectric properties of the KTN film through a diffuse interface and/or poor quality initial growth surface. Therefore, further investigation into the electric properties of the films required a more stable interface on which to grow the KTN. YBCO and SRO were identified as conducting oxide perovskite materials with similar lattice match and better temperature stability. The stability of the conducting films was tested by measuring the resistance across them before and after subsequent KTN deposition. They remained conducting after subsequent KTN deposition. Growth using YBCO electrodes on YSZ and LAO resulted in similar dielectric permittivity behavior as measured previously. The YBCO on these films was not as well

oriented and the KTN contained pyrochlore. The growth on STO substrates yielded oriented YBCO and perovskite KTN with dielectric permittivity values that peaked at 80 K, close to the intended Curie temperature of 90 K and had values ~60 % of the expected 380 at room temperature. The maximum of the dielectric permittivity was suppressed and broader than that of single crystal material. The resisitivity of the device mimics the behavior of good KTN; rising with temperature. The KTN results using YBCO were performed at growth temperatures of 300 mTorr with a potassium deficiency of ~ 10 - 20 %; improvements can be expected at higher KTN growth pressures where films close to stoichiometry can be produced. Very narrow ferroelectric hysteresis loops were observed up to 120 K which is consistent with the formation of polar regions of the material at temperatures above the 'averaged' dielectric permittivity maxima. The improvement in dielectric properties of the KTN films can be attributed to growth on a more ideal substrate KTN/YBCO/STO. However, it is not clear whether the improvement comes from easing of the stress issues or whether it is in fact due to the ability to grow a higher quality template electrode for subsequent growth of better KTN.

The use of the SRO electrode helps to illuminate some of these issues. First it was possible using KTN/SRO/LAO, a less ideal structure than KTN/YBCO/STO, to produce similar permittivity results but only at higher oxygen growth pressures, 500 mTorr. A weak dependence of dielectric permittivity with oxygen growth pressure was observed; higher growth pressures were correlated with higher dielectric permittivity. RBS results indicated the film with lowest K content had the lowest dielectric permittivity, the correlation did not hold up at higher oxygen pressures, however. The dependence of K content with oxygen partial pressure is not as strong for SRO growth surfaces indicating that the K stoichiometry is also a strong function of the substrate.

Further indication of a temperature-dependent frequency dispersion is evident in the electrical behavior of films grown on SRO/($SiO_2$)/SiN/Si based substrates. The resulting devices have extremely low dielectric constants that decrease with temperature and appear to

show a dielectric permittivity-frequency dispersion at room temperature that is similar to that observed on LAO substrates. Roll-off at frequencies < 1 kHz and shifts to lower frequencies as the temperature is lowered are observed.

## 6. Conclusions

Target Fabrication:

Increases in the density of the KTN targets could not be achieved by employing an additional ball-milling step with either $KO_2$ or $KCO_3$ potassium sources. The production of higher density, stoichiometric, single-phase perovskite targets may be achieved by using the HIP process in combination with the less volatile potassium source, $KCO_3$. This would aid in the reduction of boulders and also decrease shorting of films.

Si Integration:

The addition of Cr, Ti or $TiO_2$ layers was beneficial in providing adhesion between Pt and SiN. However, there was difficulty in stabilizing the Pt on Si-based substrates. This may be possible by alloying the Pt with iridium to slow down the grain growth. Depositing a well - reacted $TiO_2$ film at high temperatures between the Pt/Ti and SiN/Si also shows promise in stabilizing the Pt layer while providing adhesion to the SiN. Deposition of a well-reacted $TiO_2$ film requires high temperature depositions ~400 - 600 °C, however.

Improvement in the adhesion of the top contact to the KTN films may be realized by depositing a more oxidizing metal layer. Ti is a candidate, but similar to Cr, requires higher powers during sputter deposition. In order to be compatible with the lift-off technique deposition of Ti adhesion layers should be performed by e-beam evaporation.

Growth orientation:

The perovskite KTN endeavors to lower its surface tension by growing in the [100] and to a lesser extent the [110] orientations; the corresponding planes are the close-packed planes of the perovskite phase. In support of this, TEM micrographs of KTN grains indicate that they are highly faceted. Narrow phi-scan peaks of KTN films grown directly on LAO indicate excellent orientation between grains.

Perovskite/Pyrochlore phase formation:

Perovskite phase formation favors lattice matched and chemically similar substrates, and higher oxygen partial pressures. Since increasing the oxygen partial pressure increases both the potassium content of the films and decreases the pyrochlore, it is reasonable to suggest that potassium deficiency plays a role in the formation of the pyrochlore phase. Films composed entirely of perovskite KTN were grown on ($SiO_2$)/SiN/Si and Pt/(Ti)/SiN/Si substrates with the aid of a SRO template layer. These films exhibited similar electrical behavior to films containing small amounts of pyrochlore; therefore, the small amounts of pyrochlore seen in the X-ray scans do not appear to contribute to the very low dielectric permittivities measured.

Electrical Properties:

LSC is not a stable bottom electrode for KTN at growth temperatures $\geq$ 600 °C. YBCO and SRO provide more stable conducting electrodes for subsequent KTN growth. The temperature-dependent frequency dispersion of the dielectric constant below 1 kHz could arise from a large number of defects such as the K-O Schottky vacancies. It could also arise from small polar regions above the expected transition temperature that can occur in solid solution ferroelectric perovskites. However, it is clear that the K-O defected layer must give rise to

space charge behavior. There seems to be some argument for the involvement of stress in the behavior of the permittivity since only the more ideal systems KTN/YBCO/STO and KTN/SRO/LAO show a broad peak in permittivity. It may be due in part to direct coupling by the piezoelectric coefficient or the influence of stress in the formation of defected layers. As indicated by the Auger results, there is probably a good ferroelectric layer but it is masked by the series capacitance of the defective layer. It may be possible to reach this layer by etching the defective layer away.

It is necessary to separate the effects of stress and point defects on the electrical properties of KTN devices. Further progress in the development of higher and better behaved dielectric permittivity KTN films should be possible by investigating the behavior more in depth on ideal substrates such as KTN/YBCO/STO, KTN/SRO/LAO and KTN/SRO/STO. Growth on ideal substrates enables separation of stoichiometry and other growth parameter related issues. However, growth directly on the SiN/Si has shown some promise and it is worthwhile to pursue this option if the growth of KTN on these surfaces can be enhanced. One approach would be to use a YSZ template technology to optimize a YBCO electrode layer on SiN/Si prior to KTN deposition. This approach has been successful in producing high - quality YBCO on polycrystalline metal substrates.

# 7. Appendices

## A. Crystallographic Point Groups by Crystal System [103]

| Crystal System | Symbol | Pyroelectric | Piezoelectric |
|---|---|---|---|
| Triclinic | 1 | √ | √ |
| | $\bar{1}$ | | |
| Tetragonal | 4 | √ | √ |
| | $\bar{4}$ | | √ |
| | 4/m | | |
| | 422 | | √ |
| | 4mm | √ | √ |
| | $\bar{4}$2m | | √ |
| | 4/mmm | | |
| Hexagonal | 6 | √ | √ |
| | $\bar{6}$ | | √ |
| | 6/m | | |
| | 622 | | √ |
| | 6mm | √ | √ |
| | $\bar{6}$m2 | | √ |
| | 6/mmm | | |
| Monoclinic | 2 | √ | √ |
| | m | √ | √ |
| | 2/m | | |
| Orthorhombic | 222 | | √ |
| | mm2 | √ | √ |
| | mmm | | |
| Trigonal | 3 | √ | √ |
| | $\bar{3}$ | | |
| | 32 | | √ |
| | 3m | √ | √ |
| | $\bar{3}$m | | |
| Cubic | 23 | | √ |
| | m3 | | |
| | 432 | | |
| | $\bar{4}$3m | | √ |
| | m3m | | |

A tick (√) indicates that the point group is pyroelectric or piezoelectric.

B. Thin Film Deposition Techniques

Chemical Vapor Deposition (Berkeley Microlab, U.C. Berkeley))

Tylan 18 LPCVD Furnace

Gases $SiH_2Cl_2$ and $NH_3$

Low stress nitride using recipe BSLOW

Electron Beam Evaporator (Lawrence Berkeley National Laboratory)

Veeco Electron Beam Evaporator

Vacuum chamber base pressure $\leq 5 \times 10^{-6}$ Torr

Electron beam current < 0.2 Amps.

Pulsed Laser Deposition (Integrated Materials Laboratory, U.C. Berkeley)

Lambda Physik 100 KrF excimer (248 nm) laser

34 ns pulse width

Vacuum chamber base pressure ~ $2 \times 10^{-6}$ Torr

Laser spot size at the target $2 \times 4$ $mm^2$

Sputtering (Lawrence Berkeley National Laboratory)

Perkin Elmer Model 2400 RF Sputtering System

Vacuum chamber base pressure ~ $3 \times 10^{-6}$ Torr

Sputtering power 100 - 300 Watts

Argon gas ~ 10mTorr

C. Characterization Techniques

Auger Spectroscopy (Lawrence Berkeley National Laboratory)

Phi 660 with 3 kV beam voltage

FEI liquid metal $Ga^+$ ion gun was used for sputtering.

Capacitance Bridge (Lawrence Berkeley National Laboratory)

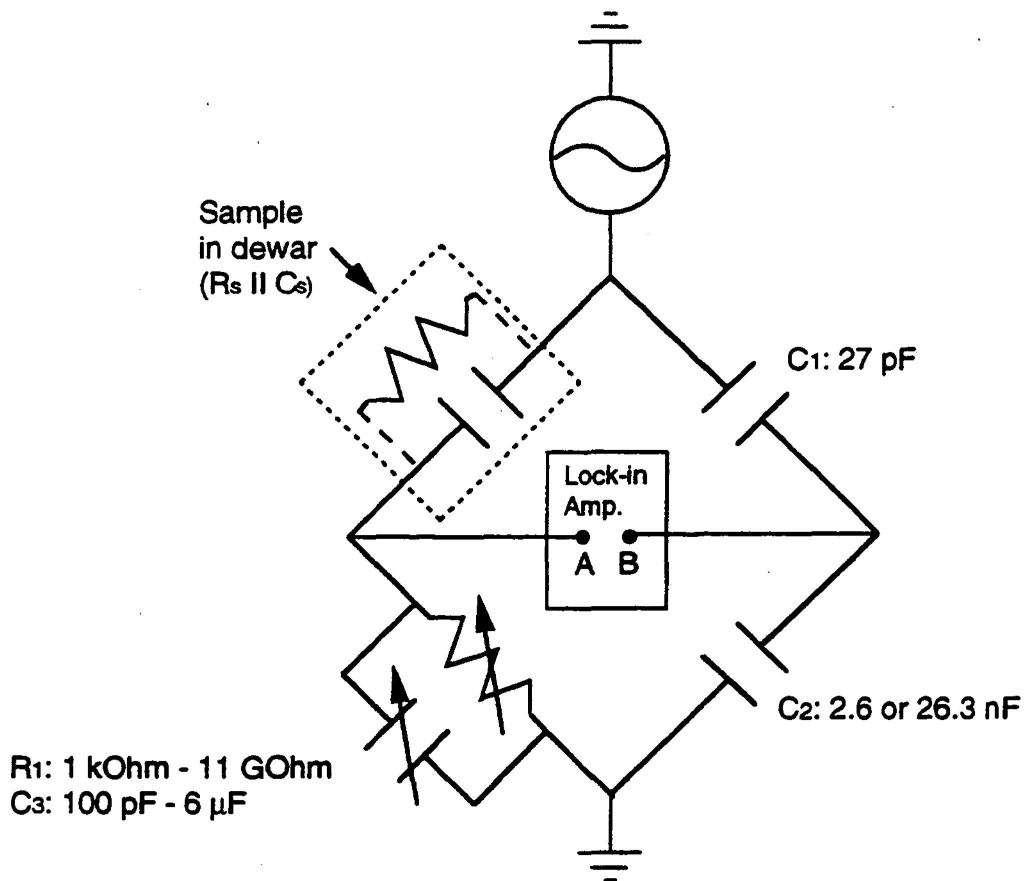


Figure 55. Schematic of the capacitance bridge used for dielectric and loss.

The schematic of the capacitance bridge built in-house is shown in Figure 55. A Princeton 5301 Lock-in Amplifier is used both to provide the A.C. drive voltage and to measure the difference in voltage amplitude and phase between A and B. When the phase and amplitude of the signal at A exactly matches that at B, the bridge is balanced. Balancing is performed by adjusting the variable resistor ($R_1$) and capacitor ($C_3$). In the balanced condition there is an impedance balance between the four arms of the bridge, which allows one to solve for the parallel or series resistance ($R_s$) and capacitance ($C_s$) of the sample under test. In the parallel case:

$$C_S = \frac{C_1 C_3}{C_2} \quad [56]$$

$$R_S = \frac{C_2 R_1}{C_1} \quad [57]$$

which is applicable for the KTN samples tested. This capacitance bridge is capable of variable frequency measurements (15 Hz < f < 1 kHz) of the capacitance and parallel resistance of the sample under test. In the parallel mode the bridge has a dynamic range of 3 pF < $C_s$ < 7 nF and $3 \times 10^{-7} < D < 3.1 \times 10^{4}$.

Hysteresis Measurements (Lawrence Berkeley National Laboratory)

Figure 56 shows a schematic of the Sawyer-Tower circuit used for ferroelectric hysteresis loop measurements. The input signal is a variable frequency 20 $V_{pp}$ sine wave that was typically operated at 100 Hz. The amplifier feedback was operated with a RC time constant of 10 ms. The capacitance range of the circuit was adjusted by varying the amplifier feedback resistor and capacitor keeping the RC time constant at 10 ms.

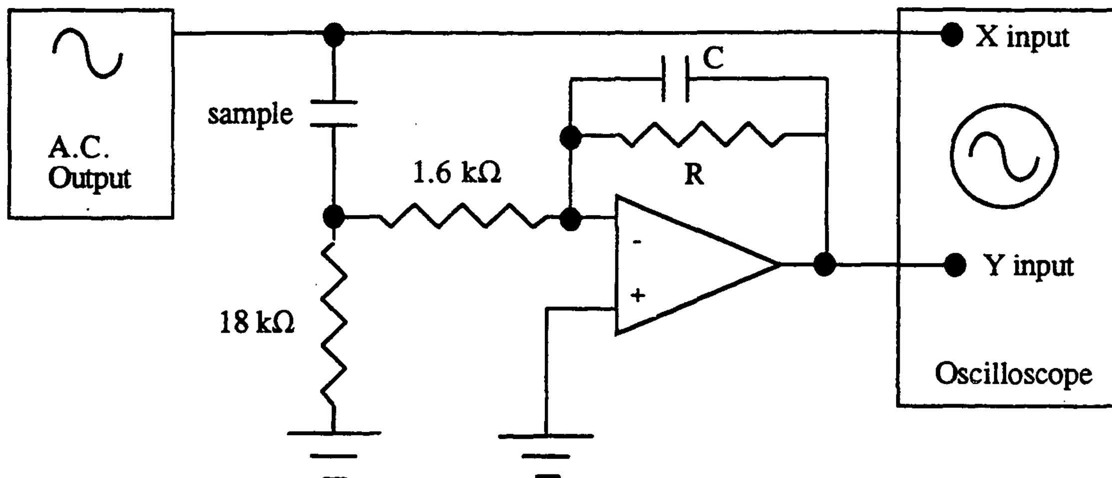


Figure 56. Sawyer Tower circuit used for hysteresis loop measurements.

Profilometer (Lawrence Berkeley National Laboratory)

Sloan Dektak IIA with a 12.5 μm diamond ball

Resistance Measurements

Keithly 617 Electrometer (D.C.)- Lawrence Berkeley National Laboratory

HP4262A LCR Meter (120 - 1 kHz) Berkeley Microlab

Capacitance bridge

Rutherford Backscattering Spectrometry (RBS) (Lawrence Berkeley National Laboratory)

2500 Van de Graaf accelerator operated at 1.95 MeV 4 $He^+$

Typical beam parameters (Figure 57): 10 nA ion beam current, backscatter angle $\Theta = 5°$, beam to detector angle $\phi = 9°$, detector solid angle $\Omega = 2°$, conversion = 3.5 keV/channel, intercept = 35 keV.
[(ion backscatter energy) = (channel #) * (conversion energy) + (intercept energy)]

Atomic concentration detection capability is 1 - 10% (Z<20) and 0.01 - 1% (Z=20-70)

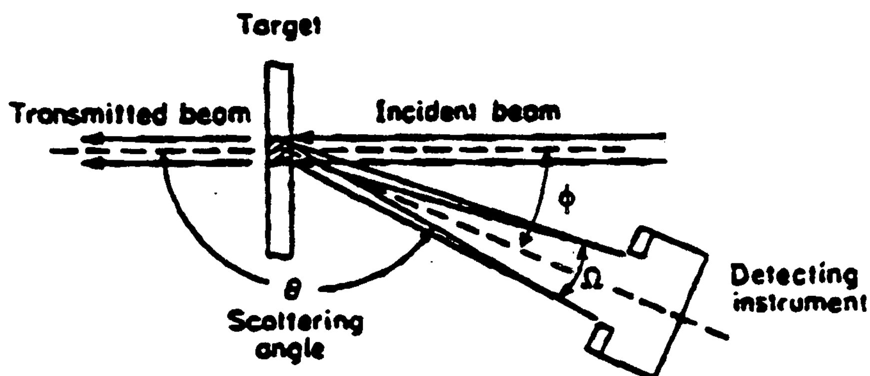


Figure 57. Schematic of the RBS geometry.[104]

X-Ray Diffraction

Normal Coupled Scan or Θ-2Θ (Lawrence Berkeley National Laboratory)

Siemens D5000 diffractometer

Cu $K_{\alpha}$ radiation and x-ray tube voltage and current set at 40 kV and 30 mA

Step size = 0.1° and time/step = 2 seconds

Rocking Curve (FWHM) and Phi-scan Measurements

Siemens D5000 four-circle diffractometer

Cu$K_{\alpha}$ radiation and x-ray tube voltage and current set at 40 kV and 30 mA

Beam divergence ~ 0.2° with Ni Filter in place

Beam divergence ~ 0.0033° with Ge (002) monochromator

X-ray Photoelectron Spectroscopy (XPS) (Lawrence Berkeley National Laboratory)

Phi 5300 ESCA System equiped with a Magnesium $K_{\alpha}$ anode (1253.6 eV)

Aperture area 1.1 - 3.6 $mm^2$

Samples from 2 -20 atomic layers

Atomic concentration ~ 0.5% detection capability for most elements

nondestructive, quantitative, less sample damage and charging effects for insulators

D. Photolithography Steps

1. Smooth backside of sample so vacuum suction on processing equipment will work
2. Prebake samples at 120°C for 5 minutes to dehydrate sample surface
3. Spin-on Shipley 1400-31 photoresist for 30 seconds at 5500 rpm
4. Cure photoresist at 90°C for 20 - 25 minutes
5. Expose photoresist at 5.6 light units (Canon Mask Aligner, Berkeley Microlab)
6. Soften photoresist in chlorobenzene for 2 minutes
7. Etch exposed photoresist in microposit:water (1:1) for 45 seconds
8. Descum for 1 minute in an oxygen plasma at 50 W (technics-c, Berkeley Microlab)
9. Metal deposition in e-beam evaporator or sputtering machine (see Appendix A)
10. Lift-off in acetone or acetone at 35-45°C in ultrasonic vibrator
11. Rinse sample in methanol then water

## 8. References


1. G. Asrar and D.J. Dokken, *Earth Observing System Handbook*, NASA, March (1993).

2. G.S. Hubbard et al, *Proceedings of the Fourth Symposium on Global Change Studies*, 194-7, January 17-22 (1993).

3. W.L. Wolfe and G.J. Zissis, *The Infrared Handbook*, revised edition, ERI Michigan, 11 - 86 (1985).

4. W.L. Wolfe and G.J. Zissis, *The Infrared Handbook*, revised edition, ERI Michigan, 11 - 86 (1985).

5. J.C. Brasunas and B. Lakew, Appl. Phys. Lett., **64** (6), 777-8 (1994).

6. G.S. Hubbard, R.E. McMurray, Jr., R.P. Hanel, D.E. Dominguez, H. Baumann (Cherry), H. Chang and E.E. Haller, *Proceedings of the Innovative Long-Wavelength Infrared Detector Workshop*, Jet Propulsion Laboratory, April 7-9 (1992).

7. J.C. Brasunas and B. Lakew, Appl. Phys. Lett., **64** (6), 777-8 (1994).

8. O. Auciello and R. Ramesh, MRS Bulletin, **21** (6), 31-43 (1996).

9. D.L. Polla and L.F. Francis, MRS Bulletin, **21** (7), 59-65 (1996).

10. O. Auciello and R. Ramesh, MRS Bulletin, **21** (6), 21 (1996).

11. J.C. Burfoot and G.W. Taylor, *Polar Dielectrics and their Applications*, University of California Press, Berkeley and Los Angeles, 35 (1979).

12. L.L. Hench and J.K. West, *Principles of Electronic Ceramics*, John Wiley and Sons, New York, 189 (1990).

13. J.M. Herbert, *Ceramic Dielectrics and Capacitors*, Gordon and Breach, New York, 15 (1985).

14. A.J. Moulson and J.M. Herbert, *Electroceramics*, Chapman and Hall, U.K., 62-8 (1990).

15. J.W. Morris, Jr., *Engineering 45 Class Notes*, Department of Materials Science and Mineral Engineering, 475-6 (1992).

16. L.L. Hench and J.K. West, *Principles of Electronic Ceramics*, John Wiley and Sons, New York, 139-44 (1990).

17. A.J. Moulson and J.M. Herbert, *Electroceramics*, Chapman and Hall, New York, 154 - 6 (1990).

18. L.L. Hench and J.K. West, *Principles of Electronic Ceramics*, John Wiley and Sons, New York, 208-12 (1990).

19. J.M. Herbert, *Ceramic Dielectrics and Capacitors*, Gordon and Breach, New York, 12 - 22 (1985).

20. L.L. Hench and J.K. West, *Principle of Electronic Ceramics*, John Wiley and Sons, New York, 222-33 (1990).

21. L. Solymar and D. Walsh, *Lectures on the Electrical Properties of Materials: Third Edition*, Oxford University Press, 271-3 (1984).

22. J.C. Burfoot and G.W. Taylor, *Polar Dielectrics and their Applications*, University of California Press, Berkeley and Los Angeles, 479 (1979).

23. A.F. Devonshire, Philosophical Magazine 3 (10), 86 (1954).

24. J.C. Burfoot and G.W. Taylor, *Polar Dielectrics and their Applications*, University of California Press, Berkeley and Los Angeles, 8-9 (1979).

25. R.W. Whatmore, Rep. Prog. Phys., **49**, 1339 (1986).

26. J.C. Burfoot and G.W. Taylor, *Polar Dielectrics and their Applications*, University of California Press, Berkeley and Los Angeles, 9 (1979).

27. J.W. Morris, Jr., *Engineering 45 Class Notes*, Department of Materials Science and Mineral Engineering, 478 (1992).

28. J.W. Morris, Jr., *Engineering 45 Class Notes*, Department of Materials Science and Mineral Engineering, 493 (1992).

29. J.S. Blakemore, *Solid State Physics*, W.B. Saunders Company, Philadelphia, 352 (1969).

30. F. Jona and G. Shirane, *Ferroelectric Crystals*, Dover Publications, Inc., New York, 46 (1993).

31. J.C. Burfoot and G.W. Taylor, *Polar Dielectrics and their Applications*, University of California Press, Berkeley and Los Angeles, 238 (1979).

32. G.A. Smolenski, *Ferroelectrics and Related Materials*, Gordon and Breach Science Publishers, Amsterdam, 366-7 (1984).

33. M.E. Lines and A.M. Glass, *Principles and Applications of Ferroelectrics and Related Materials*, Clarendon Press, Oxford, 103 (1977).

34. J.C. Burfoot and G.W. Taylor, *Polar Dielectrics and their Applications*, University of California Press, Berkeley and Los Angeles, 35 (1979).

35. J.C. Burfoot and G.W. Taylor, *Polar Dielectrics and their Applications*, University of California Press, Berkeley and Los Angeles, 35 (1979).

36. A.F. Devonshire, Advances in Physics, 3 (10), 94 (1954).

37. F. Jona and G. Shirane, *Ferroelectric Crystals*, Dover Publications, New York, 10 (1993).

38. A.F. Devonshire, Philosophical Magazine, 3 (10), 89-91 (1954).

39. A.F. Devonshire, Philosophical Magazine, 3 (10), 89-91 (1954).

40. F. Jona and G. Shirane, *Ferroelectric Crystals,* Dover Publications, Inc., New York, 109 (1993).

41. M.A. Subramanian, G. Aravamudan, and G.V. Subba Rao, Prog. Solid St. Chem., **15**, 55-143 (1983).

42. L.L. Hench and J.K. West, *Principles of Electronic Ceramics*, John Wiley and Sons, New York, 247 (1990).

43. J.M. Longo, P.M. Raccah, and J.B. Goodenough, Mat. Res. Bull., **4**, 191 (1969).

44. F. Jona and G. Shirane, *Ferroelectric Crystals*, Dover Publications, Inc., New York, 143-51 (1993).

45. A.F. Devonshire, Advances in Physics, 3 (10), 85-130 (1954).

46. M.E. Lines and A.M. Glass, *Principles and Applications of Ferroelectrics and Related Materials*, Clarendon Press, Oxford, 285-92 (1977).

47. M.E. Lines and A.M. Glass, *Principles and Applications of Ferroelectrics and Related Materials*, Clarendon Press, Oxford, 566 (1977).

48. O.M. Stafsudd and M.Y. Pines, Journal of the Optical Society of America, **61** (10), 1153-5 (1972).

49. R.W. Whatmore, Rep. Prog. Phys., **49**, 1341 (1986).

50. R.W. Whatmore, Rep. Prog. Phys., **49**, 1338-9 (1986).

51. J.C. Burfoot and G.W. Taylor, *Polar Dielectrics and their Applications*, University of California Press, Berkeley and Los Angeles, 35 (1979).

52. R.K. Willardson and A.C. Beer, *Infrared Detectors*, Academic Press, New York, 159 - 85 (1970).

53. F. Kreith and M.S. Bohn, *Principles of Heat Transfer*, Harper and Row, New York, 4 - 12 (1986).

54. R.W. Whatmore, Rep. Prog. Phys., **49**, 1341-3 (1986).

55. M.E. Lines and A.M. Glass, *Principles and Applications of Ferroelectrics and Related Materials*, Clarendon Press, Oxford, 565 (1977).

56. R.W. Whatmore, Rep. Prog. Phys. **49**, 1345 (1986).

57. M.E. Lines and A.M. Glass, *Principles and Applications of Ferroelectrics and Related Materials*, Clarendon Press, Oxford, 565 (1977).

58. M.E. Lines and A.M. Glass, *Principles and Applications of Ferroelectrics and Related Materials*, Clarendon Press, Oxford, 565 (1977).

59. R.K. Willardson and A.C. Beer, *Infrared Detectors*, Academic Press, New York, 268 (1970).

60. R.W. Whatmore, Rep. Prog. Phys. **49**, 1347 (1986).

61. R.W. Whatmore, Rep. Prog. Phys. **49**, 1348 (1986).

62. M.E. Lines and A.M. Glass, *Principles and Applications of Ferroelectrics and Related Materials*, Clarendon Press, Oxford, 565 (1977).

63. R.W. Whatmore, Rep. Prog. Phys. **49**, 1348 (1986).

64. F. Jona and G. Shirane, *Ferroelectric Crystals*, Dover, New York, 216-61 (1993).

65. O.M. Stafsudd and M.Y. Pines, Journal of the Optical Society of America, **62** (10), 1153-5 (1972).

66. L.E. Ravich, Laser Focus, 104-15, July (1986).

67. B.M. Kulwicki, A. Amin, H.R. Beratan, and C.M. Hanson, IEEE 8th ISAF Proc., 1 - 10, September (1992).

68. H.-M. Christen, L.A. Boatner, J.D. Budai, M.F. Chisolm, L.A. Gea, P.J. Marreo, and D.P. Norton, Appl. Phys. Lett., **68**(11), 1488-90 (1996).

69. H. Gui, X. Zhang, and B. Gu, Appl. Phys. Lett., **69** (16), 2353-5 (1996).

70. H.B. Baumann (Cherry), *Potassium Dihydrogen Phosphate and Potassium Tantalate Niobate Pyroelectric Materials and Far-Infrared Detectors*, Master's Thesis, University of California, Berkeley, 55 (1993).

71. J.M. Phillips, J. Appl. Phys., **79** (4), 1829-48 (1996).

72. J. Cheung and J. Horitz, MRS Bulletin, **XVII** (2), 31 (1992).

73. G.K. Hubler, MRS Bulletin, **XVII** (2), 26-7 (1992).

74. J. Cheung and J. Horitz, MRS Bulletin, **XVII** (2), 30-36 (1992).

75. D.B. Chrisey and G.K. Hubler, *Pulsed Laser Deposition of Thin Films*, John Wiley and Sons, New York, 24 (1994).

76. D.B. Chrisey and G.K. Hubler, *Pulsed Laser Deposition of Thin Films*, John Wiley and Sons, New York, 180-2 (1994).

77. J.C. Miller, *Laser Ablation Principle and Applications*, Springer-Verlag, 88-9 (1994).

78. D.B. Chrisey and G.K. Hubler, *Pulsed Laser Deposition of Thin Films*, John Wiley and Sons, New York, (1994).

79. G.K. Hubler, MRS Bulletin, **XVII** (2), 26-7 (1992).

80. K. Sreenivas, I. Reaney et al., J. Appl. Phys. **75** (1), 232-9 (1994).

81. T.G. Cooney, D.E. Glumac, W.P. Robbins and L.F. Francis, Mat. Res. Soc. Proc., **360**, 401-6 (1995).

82. A.W. Searcy, D.V. Ragone and U. Colombo, *Chemical and Mechanical Behavior of Inorganic Materials*, John Wiley and Sons, New York, 43 (1968).

83. S. Marais et al., Phys. Rev. Lett., **66**, 2480 (1991).

84. P. Avyub et al., Phys. Rev. **B**, **51**, 6135 (1995).

85. H.-M. Christen, L.A. Boatner, J.D. Budai, M.F. Chisolm, L.A. Gea, P.J. Marreo, and D.P. Norton, Appl. Phys. Lett., **68**(11), 1488-90 (1996).

86. N.W. Schubring et al., Phys. Rev. Lett., **68** (11), 1778-81 (1992).

87. R. Kelly, Surface Science, **100**, 85 (1980).

88. A. Nazeri, Appl. Phys. Lett., **65** (3), 295-7 (1994).

89. O.M. Stafsudd and M.Y. Pines, Journal of the Optical Society of America, **61** (10), 1153-5 (1972).

90. L.A. Boatner and U.T. Höchli, Ferroelectrics, **18**, 223-5 (1978).

91. S. Triebwasser, Physical Review, **114** (1), 63-70 (1959).

92. S.R. Sashital, S. Krishnakumar, and S. Esener, Appl. Phys. Lett., **62** (23), 2917-9 (1993).

93. S. Yilmaz, T. Venkatesan, and R. Gerhard-Multhaupt, Appl. Phys. Lett., **58** (22), 2479-81 (1991).

94. S. Yilmaz et al., J. Mater. Res., **9** (5), 1272-9 (1994).

95. A. Nazeri and M. Kahn, J. Am. Cer. Soc. **75**, 2125 (1992).

96. C.M. Cotell and R.E. Leuchtner, Mat. Res. Symp. Proc., **285**, 367-72 (1993).

97. C.M. Cotell and K.S. Grabowski, MRS Bulletin, **XVII** (2), 44-53 (1992).

98. C. Zaldo et al., Appl. Phys. Lett., **65** (4), 502-4 (1994).

99. S.S. Thöny et al., Appl. Phys. Lett., **61** (4), 373-5 (1992).

100. G.V. Samsonov, *The Oxide Handbook*, Plenum, New York (1969).

101. M.A. Subramanian, G. Aravamudan and G.V. Subba Rao, Prog. Solid. St. Chem., **15**, 55-143 (1983).

102. C.M. Cotell and R.E. Leuchtner, Mat. Res. Symp. Proc., **285**, 367-72 (1993).

103. J.C. Burfoot and G.W. Taylor, *Polar Dielectrics and their Applications*, University of California Press, Berkeley and Los Angeles, 608 (1979).

104. K.M. Yu, *Ion Beam Analysis Lecture Notes*, Lawrence Berkeley National Laboratory, Fall 1993.

Ernest Orlando Lawrence Berkeley National Laboratory
One Cyclotron Road | Berkeley, California 94720

Prepared for the U.S. Department of Energy under Contract No. DE-AC03-76SF00098